CRANFIELD UNIVERSITY

SCHOOL OF AEROSPACE, TRANSPORT AND
MANUFACTURING

MRes

Academic Year: 2016 - 2017

ASHLEY DENNIS

SELECTED AREA HOT MACHINING WITH A MULTI-TIPPED DIAMOND TOOLING SYSTEM

Supervisors: Dr Saurav Goel, Dr Xavier Tonnellier
September 2017

This thesis is submitted in partial fulfilment of the requirements for
the degree of MRes

© Cranfield University 2017. All rights reserved. No part of this
publication may be reproduced without the written permission of the
copyright owner.

ABSTRACT

An investigation of a novel ultra-precision tool is presented, the hot-milling multi-turret diamond tool. The tool implements micro-Laser Assisted Machining (µ-LAM) upon a multiple diamond fly cutter. Details of its design, both mechanical and optical, are presented- along with proposed modifications to Cranfield University's Tetraform C machine to allow for its implementation. Relevant experimentation is presented- the modal analysis of the Tetraform C machine and the testing of laser heating on a silicon substrate. FE analyses are carried out and calculations presented to justify design choices. Analytical investigations predicted increased depths of cut by using laser, and indicated that at lower wavelengths of laser light and with lower feed rates that the depth of cut may be significantly increased. A novel method of selecting laser wavelength based upon change in material absorptivity with temperature is investigated which may offer substantial increases in µ-LAM performance.

Keywords:

µ-LAM, hot milling, multi-tip, fly-cutter, UPRM, UPFC

ACKNOWLEDGEMENTS

I would especially like to thank Dr Saurav Goel for his guidance and support throughout the project. Thanks to Dr Xavier Tonnellier for his advice, to Professor Stephen James for advising on the optical aspects of the design, to Professor Stuart Williams and Dr Wojciech Suder for advising on the design and enabling experiments to be carried out on laser heating of silicon carbide. Thanks to John Hedge, Alan Heume and Kevin Howard for advice on the machinery in the ultra precision laboratory. Thanks to Julio Rafael Coroado for his efforts and time in the laser experimentation on the silicon substrate. Thanks to Amin and Ilias for their support.

TABLE OF CONTENTS

ABSTRACT 2
ACKNOWLEDGEMENTS........ 3
LIST OF FIGURES........ 6
LIST OF TABLES 10
LIST OF ABBREVIATIONS 12
NOMENCLATURE 13
1 INTRODUCTION........ 17
1.1 Scope and Motivation........ 17
1.2 Aims and Objectives 18
1.3 Layout of the Report........ 19
2 LITERATURE REVIEW........ 20
2.1 Challenges in Micro-Machining Hard and Brittle Materials........ 20
2.1.1 Introduction to Micro-Machining........ 20
2.1.2 DBT in Brittle Materials 24
2.1.3 Previous Work Done on Machining Hard and Brittle Materials.... 28
2.1.4 Introduction to Hybrid Micro-Machining Methods........ 30
2.1.5 Elliptical Vibration Cutting 33
2.1.6 Fly-Cutting........ 35
2.1.7 µ-LAM 37
2.1.8 Knowledge Gaps and Research Questions 40
3 RESEARCH METHODOLOGY 41
3.1 Design Specifications and Assumptions 41
3.2 Design Methodology 44
3.2.1 Specification of the Machine Tool 44
3.3 Design Process........ 49
3.3.1 Laser Photonics Optical Design........ 49
3.3.2 Mechanical Cutting Parameter Design........ 54
3.3.3 Assembly of Mechanical and Optical Design 61
3.3.4 Measures to Reduce Tool Wear and Thermal Shock 61
3.4 Preliminary Analysis of Tetraform C........ 64
3.4.1 Design Considerations for the Tool........ 64
3.4.2 Experimental Modal Analysis........ 67
3.4.3 Laser Heating Experiments on Silicon Wafer........ 69
3.5 Error and Uncertainty Budget........ 70
4 ANALYSIS AND DISCUSSION OF THE RESULTS 74
4.1 Design Process........ 74
4.1.1 Determination of Optical Parameters........ 74
4.1.2 Determination of Cutting Parameters........ 80
4.1.3 Analysis for Integration of Laser........ 85
4.1.4 Expected Optical Performance 88

4.2 Preliminary Analysis of Tetraform C 90
4.2.1 Design Assembly of the Tool 90
4.2.2 Modal Analysis 101
4.2.3 Validation of Laser Heating 104
4.3 Error and Uncertainty Predicted for Design 104
5 RECOMMENDATIONS AND FUTURE WORK 106
REFERENCES 109
APPENDIX 114

LIST OF FIGURES

Figure 1-1 SPDT (Goel et al, 2013) 17
Figure 1-2 MIRI IFU 1 (Shore et al, 2006) 17
Figure 1-3 Diamond Tool Wear (Zhang and Zhang, 2016) 17
Figure 1-4 Multi-Diamond Tool (Adapted Brinksmeier et al, 2002) 18
Figure 1-5 μ-LAM (Adapted Ravindra, 2011) 18
Figure 1-6 Combination of Two Concepts 19
Figure 2-1 Cutting Parameters (1) 21
Figure 2-2 Cutting Parameters (2) 21
Figure 2-3 Cutting Parameters (3) 21
Figure 2-4 Difficult-to-Machine Materials (Zhang and Zhang, 2017) 23
Figure 2-5 Ductile/Brittle Cut (Ravindra, 2011) 24
Figure 2-6 Brittle Cutting (Arif, 2013) 25
Figure 2-7 Sub-Surface Damage (Adapted Blake and Scattergood, 1990) 25
Figure 2-8 Plastic Transition (Adapted from Lawn and Wilshaw, 1975) 26
Figure 2-9 Feed Rate Fracture (Adapted from Bifano et al, 1991) 27
Figure 2-10 sp3-sp2 Hybridisation (Goel, 2011) 27
Figure 2-11 DBT in Shoulder (Goel, 2013) 30
Figure 2-12 1km Worn Tool (Goel, 2013) 300
Figure 2-13 LAM 311
Figure 2-14 Temp vs F_c (Jeon and Lee, 2012) 311
Figure 2-15 Laser Assisted Milling (Adapted from Lee et al, 2016) 31
Figure 2-16 Hybrid Machining (Adapted from Dandekar et al, 2010) 32
Figure 2-17 VAM (Adapted from Brehl and Dow, 2008) 33
Figure 2-18 Elliptical VAM (Adapted from Moriwaki and Shamoto, 1995) 34
Figure 2-19 VAM (Adapted from Moriwaki et al, 1991) 34
Figure 2-20 HUAT (Adapted from Muhammad et al, 2012) 35
Figure 2-21 UPFC Fly Cutter 36
Figure 2-22 UPRM Fly Cutter 36

Figure 2-23 Cutting of Aluminium Mirror with Multi-Diamond Tool 36
Figure 2-24 Diagram Illustrating µ-LAM (Adapted from Ravindra, 2011).......... 37
Figure 2-25 Laser Effect on depth of cut (Adapted from Ravindra, 2011) 38
Figure 3-1 Machining Processes Evaluated (Comley et al, 2011).................... 43
Figure 3-2 Layers Cut on Substrate 44
Figure 3-3 Edgetek SAM (Tonnellier, 2009) 45
Figure 3-4 BoX Machine (Tonnellier, 2009).. 45
Figure 3-5 Nanocentre (McKeown et al, 1990).. 46
Figure 3-6 µ6 (Morantz, 2017)... 46
Figure 3-7 Tetraform C (Arai, 2004) 46
Figure 3-8 Cable Through Spindle 48
Figure 3-9 Electrical Slip Ring 48
Figure 3-10 Exponentially Increasing Absorptivity... 51
Figure 3-11 Exponentially Increasing Temperature.. 51
Figure 3-12 Rate of Change of Refractive Index with ΔT (Green, 2008) 52
Figure 3-13 Rate of Change of Complex Refractive Index ΔT(Green, 2008) ... 52
Figure 3-14 Decreasing Absorptivity 53
Figure 3-15 Stabilising Temperature 53
Figure 3-16 Modification to Flank Area Formula.. 57
Figure 3-17 DBT Depth NR = 4mm, clearance = 35.. 62
Figure 3-18 Design Process.. 64
Figure 3-19 Optical Design Concepts Considered 64
Figure 3-20 Tool Fixture Concepts Considered... 65
Figure 3-21 Concepts for Modifying Tetraform C 66
Figure 3-22 Nodes Used in Modal Analysis (Orientation of Machine Shown) .. 68
Figure 3-23 Filtering of Modal Results.. 68
Figure 3-24 Experimental Setup for Laser Testing... 69
Figure 3-25 Machining Loop.. 70
Figure 3-26 Tetraform C Machining Loop.. 70

Figure 3-27 Z Axis Table 71
Figure 3-28 X Axis Support Free Body 72
Figure 3-29 Meshed X Axis Support........ 72
Figure 3-30 Tetraform C Frame........ 72
Figure 3-31 Spindle Support Free Body 73
Figure 3-32 Meshed Spindle Support........ 73
Figure 3-33 Spindle Errors 74
Figure 3-34 Tool Fixture Free Body Diagram 74
Figure 3-35 Tool Fixture Meshed 74
Figure 4-1 Absorptivity of α-Si (Palik, 1998a) 74
Figure 4-2 Depth of Absorption for α-Si (Palik, 1998a)........ 75
Figure 4-3 Loss of Intensity α-Si........ 75
Figure 4-4 Surface Temperatures of Heated Silicon 76
Figure 4-5 n values of pristine silicon 77
Figure 4-6 k values of pristine silicon 77
Figure 4-7 dn/dT values of pristine silicon........ 78
Figure 4-8 dk/dT values of pristine silicon 78
Figure 4-9 Temperature Increase in Pristine Silicon........ 80
Figure 4-10 Maximum Feed Rate for Different Depths of Cut in 3C-SiC 82
Figure 4-11 Maximum Feed Rate for Different Depths of Cut in 4H-SiC 82
Figure 4-12 Maximum Feed Rate for Different Depths of Cut in 6H-SiC 83
Figure 4-13 Maximum Feed Rate for Different Depths of Cut in Silicon 83
Figure 4-14 Feed Rate correlated to Surface Roughness 84
Figure 4-15 Feed Rate correlated to DBT Depth........ 85
Figure 4-16 Maximum Feed Rate (NR = 3mm, clearance = 10)........ 86
Figure 4-17 DBT Related to Feed Rate........ 87
Figure 4-18 Predicted Increase in Diffusion Rate 88
Figure 4-19 Final Optical Setup........ 90
Figure 4-20 Beam Splitter for 294nm Wavelength Light........ 90

Figure 4-21 Final Optical Assembly 91
Figure 4-22 Multiple Fibre Rotary Joint 93
Figure 4-23 Combined Laser Diodes (CAD Parts from Thorlabs.com) 93
Figure 4-24 Size Mismatched Optical Components 94
Figure 4-25 Tool Fixtures for Diamond Tools on Spindle 94
Figure 4-26 Hollow Tool Fixture Concept 95
Figure 4-27 Multiple Angle Tool Fixture 95
Figure 4-28 Differing Swing Radii 95
Figure 4-29 ALM Tool Fixture 96
Figure 4-30 Focused Laser Beam 96
Figure 4-31 Misalignment Laser Beam 96
Figure 4-32 Adopted Optical Setup 97
Figure 4-33 Diamond Tool Configuration 97
Figure 4-34 Aligning of Laser Beam 98
Figure 4-35 Machining Loop 99
Figure 4-36 Components on Tetraform C 99
Figure 4-37 MRR Correlated to Cutting Speed (s=30µm/rev) 99
Figure 4-38 Axial Motion of Configuration 10000
Figure 4-39 Spindle Support Brackets 10000
Figure 4-40 Modes Identified in Experimentation 10101
Figure 4-41 Components of Tetraform C Tested 10502
Figure 4-42 View from Underneath Tetraform C 10505
Figure 5-1 Novel Aspects of Study 107
Figure A-1 Tool Fixture Manufacturing Drawing 116
Figure A-2 Diamond Tool Manufacturing Drawing 11717
Figure A-3 Spindle Bracket Manufacturing Drawing 11818

LIST OF TABLES

Table 2-1 Development of SPDT, (Adapted Brinksmeier and Preuss, 2012) . 200
Table 2-2 Forms of Tool Wear, (Zhang and Zhang, 2016) 22
Table 2-3 Cutting Lengths, (Adapted from Zhang and Zhang, 2017) 23
Table 2-4 DBT Depths for Different Materials, (Source: Ravindra, 2011)......... 24
Table 2-5 History of DBT Concept (Source: Goel, 2013) 26
Table 2-6 History of Machining Hard and Brittle Materials 28
Table 2-7 Challenges in Machining Silicon Carbide (Source: Goel, 2014) 29
Table 2-8 Improvements in R_a by VAM (Source: Brehl and Dow, 2007) 33
Table 2-9 History of VAM 34
Table 2-10 Optimised Laser Powers at λ ~1µm, (Ravindra, 2011)................... 38
Table 2-11 DBT Depths of Cut With Laser (Based on Ravindra, 2011) 39
Table 2-12 Comparison of PD with Different Machining Parameters 39
Table 3-1 Specification for Installed Tool 42
Table 3-2 Weighting for Machine Selection... 45
Table 3-3 Edgetek SAM (Tonnellier, 2009) 46
Table 3-4 BoX (Tonnellier, 2009) 46
Table 3-5 Nanocentre (McKeown et al, 1990).. 47
Table 3-6 µ6 (Morantz, 2017).. 47
Table 3-7 Tetraform C (Arai, 2004) 47
Table 3-8 Pugh matrix for different machines considered 48
Table 3-9 Material Properties of 4H-SiC.. 60
Table 3-10 Parameters Used in Diffusive Wear Calculation............................ 63
Table 3-11 Cutting Conditions Considered in Error Budget............................. 71
Table 4-1 Parameters Used to Verify Depth of Heating 79
Table 4-2 Critical Depths of Cut 81
Table 4-3 Critical Crack Lengths (Goel, 2014) 81
Table 4-4 Critical Loads (Goel, 2014)... 84
Table 4-5 Critical Depths of Cut 86

Table 4-6 Critical Crack Lengths 86
Table 4-7 Temperature Increases for Diamond Graphitisation......................... 89
Table 4-8 Predicted Increases in Graphitisation... 89
Table 4-9 Parameters used for predicting maximum temperature change....... 89
Table 4-10 Power Ratings of Components in Optical Setup 91
Table 4-11 Performance of Components used for Adaptation of Tetraform C 100
Table 4-12 Modes Detected in Tetraform C 10303
Table 4-13 Modes Identified by Analysis... 10303
Table 4-14 Sources of Vibration 103
Table 4-15 Accuracies of Z Axis Table.. 10404
Table 4-16 Deflections in Tetraform C Frame 105
Table 4-17 Combined Accuracies in the Z Direction 10505
Table A-1 Fiber Coupler Specification... 114
Table A-2 Rotary Joint Specification 114
Table A-3 1000nm Beam Splitter 11414
Table A-4 295nm Beam Splitter 11515

LIST OF ABBREVIATIONS

ALM	Additive Layer Manufacturing
AFM	Atomic Force Microscopy
CVD	Chemical Vapour Deposition
CAD	Computer Aided Design
CW	Continuous Wave
DBT	Ductile-to-Brittle Transition
ELID	Electrolytic In-Process Dressing
FEA	Finite Element Analysis
HPPT	High Pressure Phase Transformation
HUAT	Hot Ultrasonic Assisted Turning
LAM	Laser Assisted Machining
LAM	Laser-Assisted Machining
MRR	Material Removal Rate
µ-LAM	Micro-Laser Assisted Machining
PLAM	Pulsed Laser Assisted Micro-Milling
SiC	Silicon Carbide
SPDT	Single Point Diamond Turning
TAM	Thermally Assisted Machining
UPFC	Ultra Precision Fly-Cutting
UPRM	Ultra Precision Raster Milling
VAM	Vibration Assisted Machining

NOMENCLATURE

A	Area of Focused Laser Beam
A_0	Pre-Exponential Factor of Diffusion
A_e	Factor Depending upon Entropy
a	Acceleration
A_c	Uncut Chip Area
A_f	Area at Flank of Tool
A_l	Laser Spot Area
b	Wavelength Dependent Constant
BM	Bending Moment
c	Concentration of Carbon Atoms
c_P	Rate of Change of Refractive Index
c_0	Saturation Concentration
C_D	Carbon atoms per unit surface area
C_p	Specific Heat Capacity
C_m	Length of Median Crack
C_l	Surface Damage
d	Depth of Focus
D	Beam Diameter
d	Distance
dc	Depth of Cut
d_f	Fibre Optic Cable Core Diameter
d_s	Laser Spot Diameter
E	Young's Modulus
E_D	Diffusive Activation Energy
E_{DGcat}	Catalytic Activation Energy
E_a	Activation Energy
E_d	Specific Cutting Energy
f	Feed Rate
f_l	Focal Length
F	Force

F_c Cutting Force
F_t Thrust Force
I Laser intensity
H Material Vicker's Hardness
h_{min} Minimum Undeformed Chip Thickness
I_n Mode Number
I_s Moment of Inertia
k Imaginary Refractive Index
k_c Rate of Complex Formation
k_r Arrhenius Rate Constant
k_D Diffusive Wear Constant
K_c Fracture Toughness
l Laser Absorption Depth
m Mass
M* Number of Active Metal Sites
MRR Material Removal Rate
n Refractive Index
n_h Strain Hardening Exponent
P Laser Power
P_L Load
p Represents either n or k
p_n Number of Radial Zero Fields
P_c Cutting Pressure
$PD_{/L}$ Power Density per Unit Length
q Power Density
r Tool Edge Radius
r_d Diffusive Wear Rate
r_c Cutting Ratio
r_{cat} Catalytic Reaction Rate
R Nose Radius
R_a Surface Roughness
R_c Gas Constant

R_l Reflectance

R_s Swing Radius

R_t Total Roughness

S_{max} Maximum Feed Rate

s Spring Back

T Temperature

ΔT_{max} Maximum Temperature Change

t Laser Dwell Time

t_0 Undeformed Chip Thickness

T_0 Initial Temperature

t_a Time for Spindle to Reach Speed

v Poisson's Ratio

V_s Spindle Speed

V_c Cutting Speed

w Length of Flank Wear

W Width of Cut

x Ratio of carbon atoms that escape

z Depth Below Substrate Surface

α Absorption Coefficient

α_e Instantaneous rake angle

α_r Angular Acceleration

α_t Coefficient of Thermal Expansion

ε Strain

ε_P Plastic Strain

ε_y Yield Strain

λ Wavelength of Laser Light

λ_d Distance Between Sites

ρ Density

ω Angular Velocity

τ Torque

λ Wavelength

γ_c Maximum Crack Length

Y_S Specific Surface Energy

φ_e Effective Shear Angle

μ Friction Between Tool and Chip

μ_f Friction at Flank of Tool

σ_C Compressive Yield Stress

σ_f Stress at Flank of Tool

σ_y Yield Stress

θ_r Clearance Angle

1 INTRODUCTION

1.1 Scope and Motivation

Single point diamond turning (SPDT) is a machining process which is used ‘to generate ultra smooth machined surfaces’ (Goel et al, 2013) as shown in figure 1-1, such as the MIRI IFU 1 reflector shown in figure 1-2. It is also possible to create ‘freeform shape optics in a single pass’ with SPDT, making it preferred to other finishing processes like grinding and polishing (Goel et al, 2013). SPDT works by running a small diamond over the workpiece, because the diamond is very hard it removes material in a predetermined way. SPDT is used to produce many complex items, for example the MIRI IFU 1 image slicer for the James Webb telescope (Shore et al, 2006).

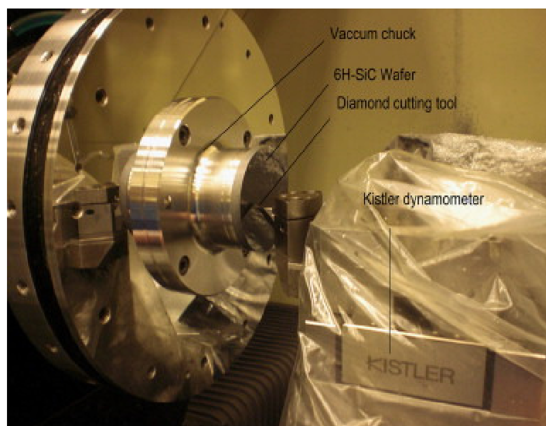

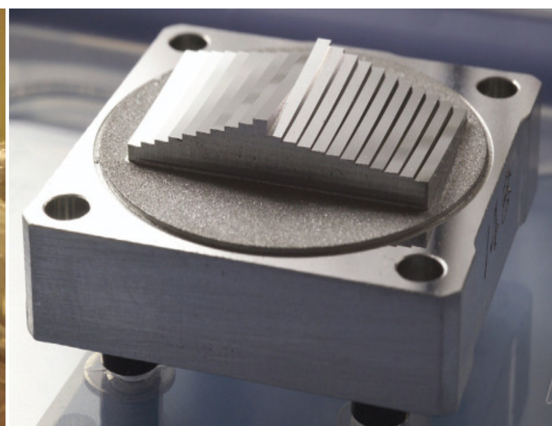

Figure 1-1 SPDT (Goel et al, 2013) **Figure 1-2 MIRI IFU 1 (Shore et al, 2006)**

Zhang et al (2016) describe how wear of the diamond tool (as shown in figure 1-3) can be a serious limitation to SPDT in turning of hard and brittle materials. They describe three categories of wear of diamond tools: mechanical, chemical and physical. They describe diamond tools which would normally wear after 100’s of kilometres wearing after only 10’s of metres when cutting difficult to cut materials like silicon carbide.

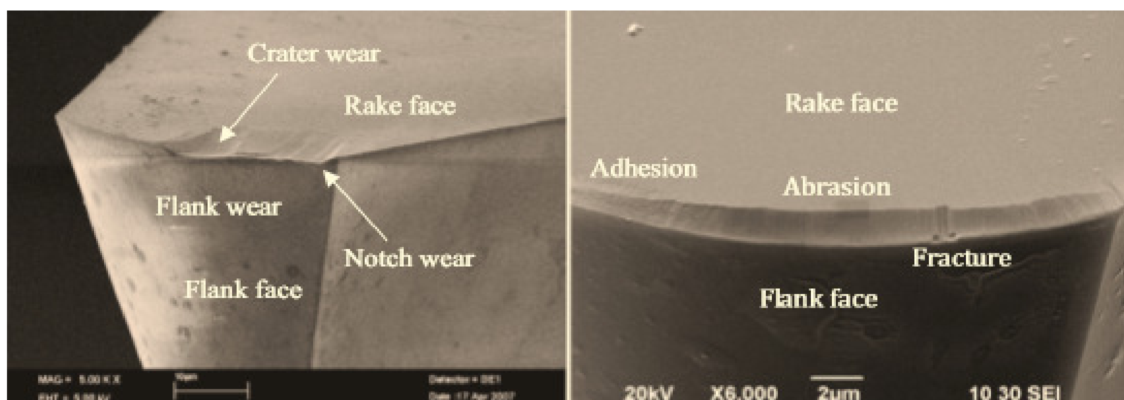

Figure 1-3 Diamond Tool Wear (Zhang and Zhang, 2016)

The purpose of the tool proposed is to facilitate the machining of difficult-to-machine materials, particularly those for which wear is caused by hardness and toughness, for example silicon carbide and silicon (used in optical mirrors, amongst other applications) and tungsten carbide (used in the nuclear industry). Silicon carbide has been identified by NASA's Glenn Research centre (Nemeth et al, 2007) as a material which can have great benefit across several different sectors like electronics in spacecraft, aircraft, power, automotive, communications and energy production, but is not yet machinable by diamond turning. Silicon carbide has been identified as a wide-bandgap semiconductor for high temperature applications (Casady et al, 1996), as a new MEMS technology (Sarro, 2000), and in mirrors for use in space (Shore et al, 2010).

Because the materials of interest are difficult to machine, when being turned with diamonds they cause tool wear, so large components cannot be machined because the tool wears out prematurely. Because of this, large items like telescope mirrors are currently ground and polished, but this is less deterministic than diamond cutting. Grinding and polishing are force and time dependent processes, so involve increased complexity when compared to SPDT, as SPDT involves removal of a known geometry of material. In addition to countering wear, it is hoped that the proposed tool will offer advantages in cutting performance, like increased rates of material removal, allowing machining of the highly desirable materials such a silicon carbide.

1.2 Aims and Objectives

The aim of the current study is to investigate a novel tool which synthesises two concepts involving diamond cutting, shown in figures 1-4 and 1-5. The two concepts (which are discussed later in the report), multi-diamond fly cutting and micro-Laser Assisted Machining (µ-LAM), both offer advantages in terms of cutting results such as material removal and surface roughness. It is hypothesised that by combining the two techniques (as shown in figure 1-6), an increased improvement in cutting efficiency and quality can be achieved as well as a reduction in tool wear, possibly enabling the machining of the difficult-to-machine materials of interest like silicon carbide.

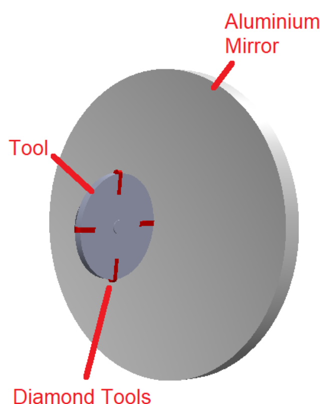

Figure 1-4 Multi-Diamond Tool (Adapted Brinksmeier et al, 2002)

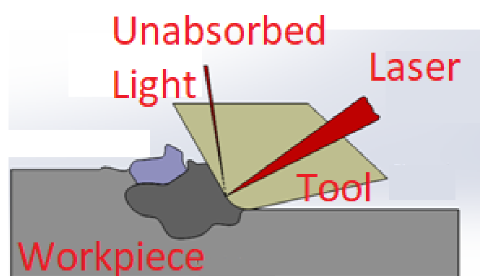

Figure 1-5 µ-LAM (Adapted Ravindra, 2011)

The aim of the study is to carry out an extensive assessment of the concept, including its feasibility and outcomes that are likely to be achievable via its use. Objectives specified for achieving this are carrying out the design for the tool (optical, mechanical, and for the integration of the optical and mechanical aspects), specifying components that can be used for the implementation of the design, determining limiting factors likely to influence the optical performance of the tool, carrying out design work to enable the tool to be implemented upon a machine tool at Cranfield University, carrying out experimentation that is relevant to the tool and its implementation upon the machine, and to predict the machining capabilities that are achievable via the implementation of the tool upon the machine. It is hoped that by achieving these objectives, it will be possible to determine the likely performance enhancements that the tool can offer, both in terms of increased cutting capability and in countering the problem of tool wear which is important for machining of difficult-to-machine materials of interest such as silicon carbide.

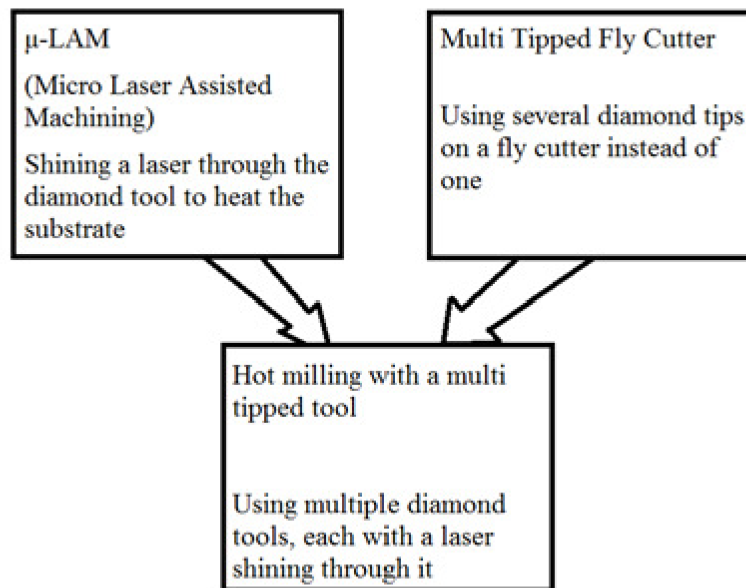

Figure 1-6 Combination of Two Concepts

1.3 Layout of the Report

The report consists of five main sections: the introduction, literature review, research methodology, analysis and discussion of the results, and the recommendations and future work. The introduction serves to describe the broad topic to the reader, and to provide some background information which explains the motivation of the project and its objectives. The literature review aims to give the reader a summary of the research which has been carried out which is relevant to the project. In the research methodology section, the work that was carried out as part of the project is introduced. In the analysis and discussion of the results section, the results that were obtained are presented and analysed, and conclusions are drawn which are

relevant to the project. Finally, in the recommendation and future work section, the findings of the project are drawn together and suggestions relevant to the technology are made.

2 LITERATURE REVIEW

2.1 Challenges in Micro-Machining Hard and Brittle Materials

2.1.1 Introduction to Micro-Machining

Brinksmeier and Preuss (2012) review the concept of micro-machining, which is described here to introduce the broad area in which the project lies. They describe the term 'Micro-machining' as a machining process by which small ('microscopic') bits of material are removed in order to achieve a high geometrical accuracy that is otherwise 'unattainable'. They describe how this can be achieved using physical, chemical or mechanical processes- with cutting (the process involved in this project) being a mechanical process. Brinksmeier and Preuss (2012) highlight the evolution of diamond machining, which is shown in table 2-1.

Table 2-1 Development of SPDT, (Adapted Brinksmeier and Preuss, 2012)

1960's	• Investigation into error sources of machine motions carried out systematically • High precision air bearing spindles developed
1970's	• Encoders capable of location information better than 100nm • Creation of high quality diamond tools
1980's	• Diamond machining became commercialised • Laser interferometers used for position control (better than 10nm) • CNC implemented • Quality of diamond tools improved
1990's	• Glass scales used for position control (better than 1nm) • Oil hydrostatic bearings for linear slides introduced • Multi axis machines introduced for freeform machining • PC controls • Air conditioning of machines for thermal control
2000's	• Fast tool servo and slow slide servo introduced • Linear motors introduced for causing linear motion • Software improved for freeform machining • Ion beam polishing introduced for non circular cutting edges on tool

There are several parameters which are important to understand if working with SPDT, these are introduced here. The geometry of a diamond tool can be defined in terms of several parameters, the main of which are: nose radius, rake angle, clearance angle and edge radius.

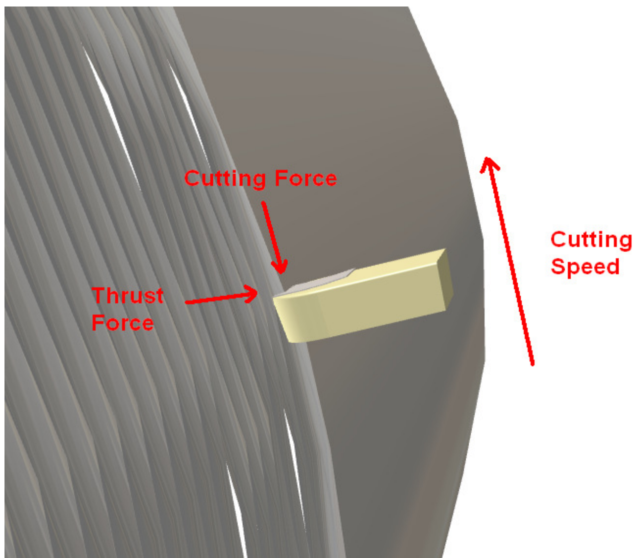

Figure 2-1 Cutting Parameters (1)

Figure 2-1 is an illustration showing a diamond tool cutting through a material- the tool moves in the direction of the arrow, and material is removed in front of the tool in the form of a chip. The cutting speed is the speed at which the tool moves in this direction, and the cutting force is the force exerted on the tool opposing this motion. The thrust force is the reaction force acting vertically, which acts to oppose the pressure exerted downwards on the diamond tool to induce the cut.

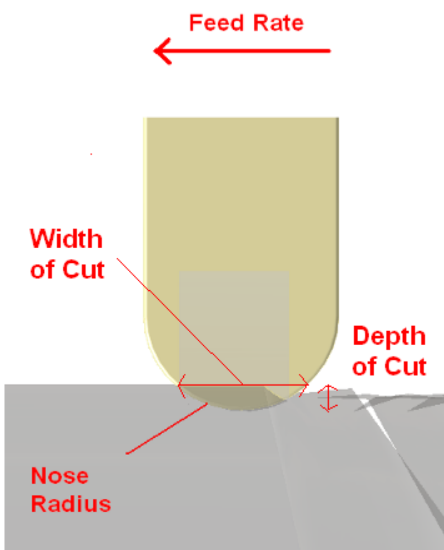

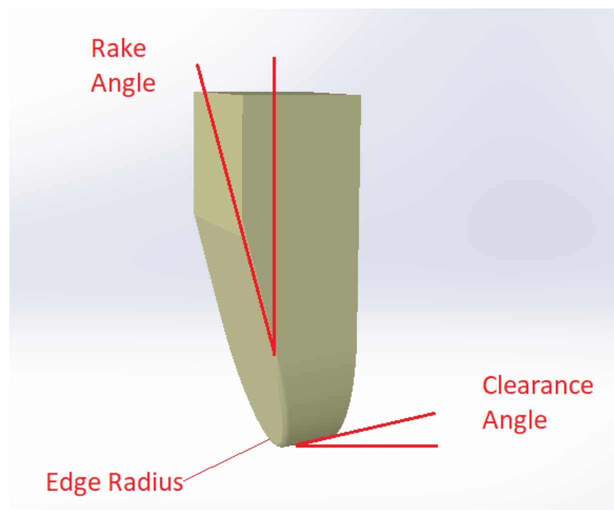

Figure 2-2 Cutting Parameters (2)

Figure 2-3 Cutting Parameters (3)

Figure 2-2 shows the view perpendicular to the cutting direction. From this view, the nose radius of the tool can be seen, which is another critical parameter. Also, the distance that the tool

travels laterally in this view in one revolution of the workpiece is known as the feed rate. The depth of cut is how deeply the diamond penetrates the material's surface.

In Figure 2-3, there are two angles which can be seen which are important, the first is the rake angle- the angle that the leading edge of the tool makes with the vertical, being positive if orientated clockwise of the vertical, and negative if orientated anti-clockwise to the vertical (in this diagram), in this case the rake angle is negative. The other important angle is the clearance angle- this is defined as the angle that the trailing edge of the diamond tool makes with the horizontal. A further key parameter is the edge radius, which is the radius shown on the tool from this view.

An issue faced in SPDT is that the diamond tool can become worn through various different mechanisms. When the tool becomes worn, the cutting performance worsens, and the surface quality and form accuracy can become poor. Table 2-2 shows the different mechanisms which act to cause tool wear.

Table 2-2 Forms of Tool Wear, (Zhang and Zhang, 2016)

Nature	Mechanism	Feature
Mechanical Wear	Friction	Abrasive Wear
		Tribo-chemical Wear
	Fatigue	Chipping, Cracking, Fracture
	Adhesion	Adhesive Wear
Chemical Wear	Chemical Reactivity	sp^3, sp^2, sp
	Amorphisation	Diamond-like particles
	Diffusion	
Physical Wear	Thermal Properties	Thermo-chemical Wear
	Electricity	Tribo-electric Wear
	Crystal Orientation	Anisotropy
	Defect	Impurity

Different forms of wear are dominant for different materials- in cutting of iron and steel, for example, chemical wear is dominant as iron reacts chemically with diamond; in cutting silicon carbide, wear is predominantly abrasive because of the hardness of the material. As different materials induce different forms and rates of wear because of their material properties, some materials have been classified as 'difficult-to-machine' (Zhang and Zhang, 2017). The table below shows the elements of the periodic table classified as either difficult or easy to machine:

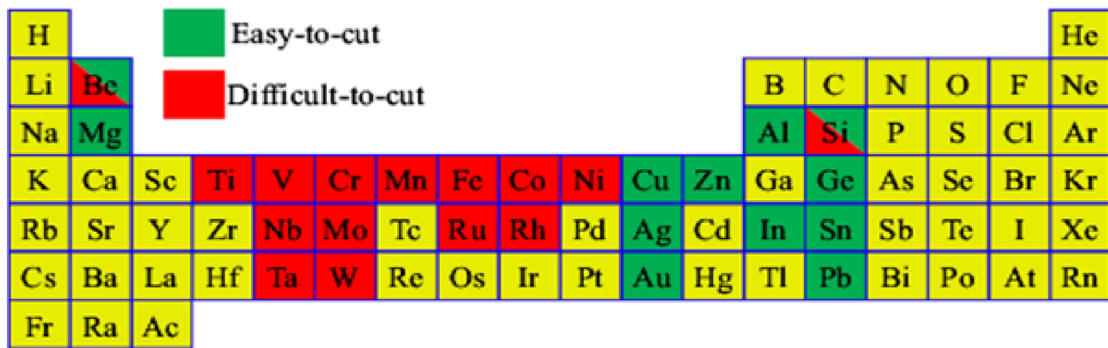

Figure 2-4 Difficult-to-Machine Materials (Zhang and Zhang, 2017)

It can be seen from figure 2-4 that the elements which form carbides are difficult-to-cut, this is because of unpaired electrons in the outer valence of the elements which react chemically with diamond (Zhang and Zhang, 2017). Silicon is shown to be partially machinable, but as is known, silicon carbide is not machinable because of its high hardness among other reasons (Goel, 2014).

Zhang and Zhang (2017) describe the way in which cutting of different materials is limited by diamond tool wear, as shown in table 2-3.

Table 2-3 Cutting Lengths, (Adapted from Zhang and Zhang, 2017)

Material	Diamond Tool Wear Limited Cutting Distance (m)
Glass	4000
Silicon	1000
Silicon Carbide	10's
Iron	6
Titanium	6280
Copper	30000+

It can be seen how track lengths of silicon that can be machined are only about 3% as large as those of copper, and that silicon carbide cannot be machined to significantly large areas. As an indication, at a surface roughness of 100 nm RMS: over 6.7 m^2 is machinable in copper; 0.2 m^2 is machinable in silicon; and 0.001 m^2 is machinable in silicon carbide- approximately the size of a small coin. As described previously, silicon carbide is desired as a mirror for space applications, so sizes in excess of 1 m^2 are desirable, implying a considerable required increase in track length.

2.1.2 DBT in Brittle Materials

The Ductile-to-Brittle Transition (DBT) is discussed here as the tool proposed aims to cut brittle materials in the ductile regime. DBT is characterised by material which is normally brittle responding in a ductile way when being machined as shown in figure 2-5, which is advantageous as it allows for better surface finishes to be achieved. The materials which undergo this process include silicon, tungsten, tungsten carbide and silicon carbide.

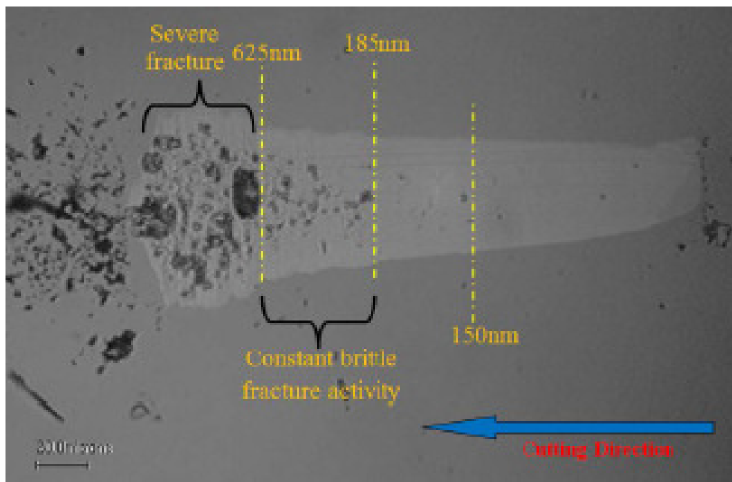

Figure 2-5 Ductile/Brittle Cut (Ravindra, 2011)

A key parameter which determines whether a material will be cut in a ductile way is the depth of cut which is used. Materials like silicon and silicon carbide can be said to have a specific depth of cut beyond which they are expected to be cut in a brittle way, and before which they are expected to be cut in a ductile way. The critical depths of cut for some materials are shown in table 2-4 from Ravindra's (2011) investigation. It is important to note that the materials of concern for this project is silicon and silicon carbide wafers, not Chemical Vapour Deposited (CVD) silicon or silicon carbide, as described by Shore (1995).

Table 2-4 DBT Depths for Different Materials, (Source: Ravindra, 2011)

Material	Average DBT Depth
4H-SiC	20.0 nm
6H-SiC	17.5 nm
3C-SiC	42.5 nm
Silicon	185.0 nm
Sapphire	122.5 nm

Quartz	87.5 nm
Spinel	205.0 nm
AlTiC	425.0 nm

There are two main mechanisms which can be said to govern whether material is cut in a ductile or brittle way, these are: whether the material being removed is deforming plastically or fracturing (Arif et al, 2013); and whether sub-surface damage is caused in the material (Blakeand Scattergood, 1990). In the first of these criteria, shown in figure 2-6, there is a specific energy for each set of cutting conditions which is required to propagate a crack in the material. If cutting takes place below this energy, then the material is removed in a plastic (ductile) way. If this energy is exceeded in cutting, then the material fractures and brittle cutting occurs.

In the second criteria, as shown in figure 2-7, for each cutting condition there is a maximum crack length which is induced during the cutting process. Depending upon the feed rate employed, this crack may or may not propagate beneath the cut surface. In the case that the crack does extend beneath the surface, sub-surface damage is induced and the cutting can be said to be brittle.

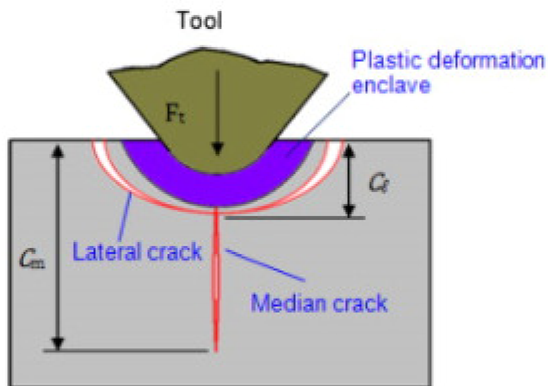

Figure 2-6 Brittle Cutting (Arif, 2013)

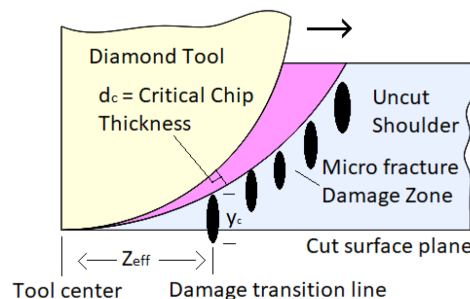

Figure 2-7 Sub-Surface Damage (Adapted from Blake and Scattergood, 1990)

Goel et al (2013) chart the evolution of the concept of ductile to brittle (DBT) transition in the machining of brittle materials, which is reproduced in table 2-5.

Table 2-5 History of DBT Concept (Source: Goel, 2013)

Authors (Year)	Development
King and Tabor (1954)	Identified that because of high hydrostatic pressures, brittle materials like rock-salts deform plastically when they would otherwise be expected to fracture in a brittle way
Bridgman and Šimon(1953)	Describe 'plastic flow' of glasses under high hydrostatic pressure (glass being a normally brittle material)
Lawn and Wilshaw (1975)	Observed this plastic behaviour of glasses in nano-indentation, and suggested the existence of the elastic/plastic transition- as shown in figure 2-8
Niihara (1979)	Further explained that any material experiencing high hydrostatic stresses could be expected to deform plastically
Bifano et al(1991)	Suggested that all materials would respond in a ductile way if they were cut at a small enough depth, because at the small depth more energy is required to propagate a crack than for the material to undergo plastic deformation. They also found that grinding feed rate is important for ductile machining; as shown in figure 2-9
Blake and Scattergood (1990)	Identified the link between machining of brittle materials in a ductile way and indentation tests, and recognised that the same mechanism of high hydrostatic pressure resulting in ductile deformation was at play. They highlighted that there exists a critical depth of cut below which material deforms plastically, and beyond which it deforms in a brittle way.

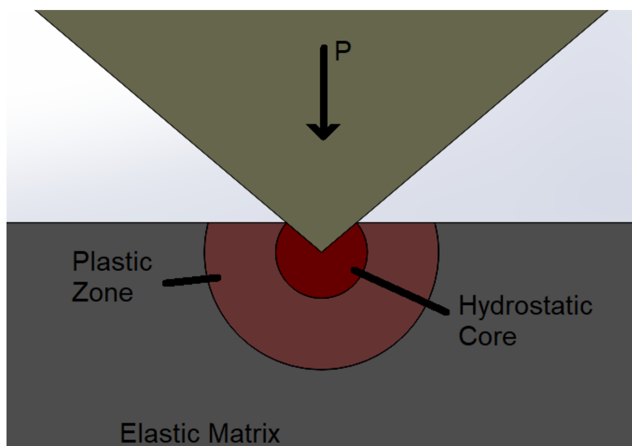

Figure 2-8 Plastic Transition (Adapted from Lawn and Wilshaw, 1975)

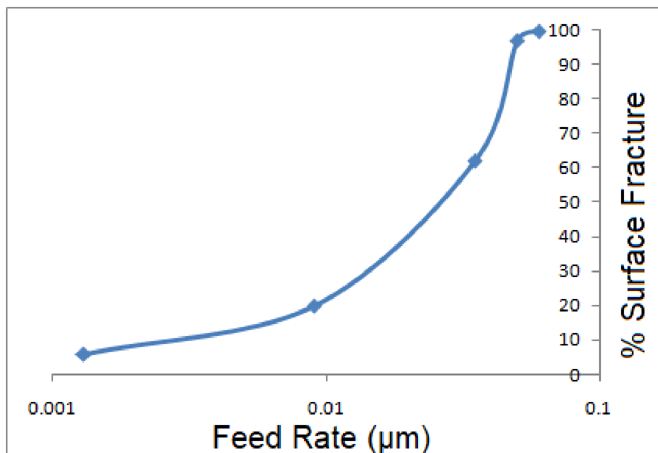

Figure 2-9 Feed Rate Fracture (Adapted from Bifano et al, 1991)

Ngoi and Sreejith (2000) explain how cutting being brittle or ductile depends upon the resolved tensile stress on the cleavage plane and shear stress on the slip plane, and that these are governed by the 'size of the stress field' caused by the machining process. They describe how in silicon, plastic (ductile) mode machining is based upon a phase change in the material to its amorphous state.

Jacob et al (2005) investigated the DBT of silicon carbide in fly-cutting. In so doing, they found that the same principle applied to this cutting technique as to SPDT. Jacob found a DBT depth of 70nm in 6H-SiC, observing brittle mode cutting beyond this depth (which is substantially larger than that suggested by Ravindra, 2011).

Goel et al (2011) carried out a molecular dynamics simulation to investigate the root causes of the plastic deformation of SiC. They found that cubic silicon carbide undergoes a process called 'sp^3-sp^2 order-disorder (shown in figure 2-10). This occurs when the tetrahedral bonding structure of 3C-SiC becomes distorted, such that the angle between the bonds changes from 109.5° to 120°. This occurrence causes a graphene like substance to form, which in turn leads to the ductile response from 3C-SiC.

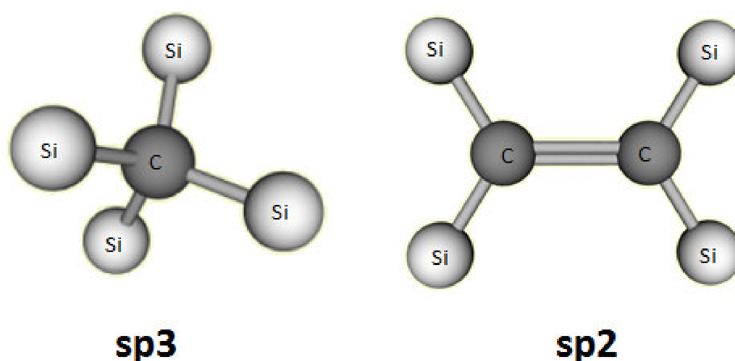

Figure 2-10 sp3-sp2 Hybridisation (Goel, 2011)

The DBT depth achievable in different materials has a significant impact upon cutting performance and upon the machinability of materials such as silicon carbide which are in such high demand for technologically advanced applications. When materials can be machined at higher DBT depths, it is possible to take greater depths of cut, and therefore the material removal rate (MRR) can be increased. Additionally, to a certain extent, increasing the DBT depth can be shown to mitigate the effect that tool wear has. The usual effect that increased tool wear has is to cause cutting to become brittle, but (as demonstrated with the formulae of Arif, 2013) when cutting a material with a larger DBT depth at a shallower depth of cut, the effect of tool wear has can be mitigated, allowing for ductile cutting with a more worn tool.

2.1.3 Previous Work Done on Machining Hard and Brittle Materials

A great amount of research has been carried out to counter the problems posed by 'difficult-to-machine' materials, thereby enabling the machining of important materials such as silicon carbide. Some of this is presented here for information on the challenge that the investigation is attempting to address. Ngoi and Sreejith (2000) present a review of ductile regime machining of materials, which is shown in table 2-6 as it presents an overview of the methods being used and understanding in this field.

Table 2-6 History of Machining Hard and Brittle Materials

Authors (Year)	Development
Syn and Taylor (1989); Blake and Scattergood (1990)	Altering different cutting parameters such as cutting speed, tool geometry and rake angles affected the DBT transition; it was found particularly that having a large negative rake angle is beneficial for inducing ductile mode machining.
Nakasuji et al (1990)	Experimentation in cutting germanium, silicon and LiNbO3 in order to achieve a mirror finish using diamond turning. They put forward a model to describe the critical chip thickness that would result in ductile machining. They were able to achieve finishes better than 20nm PV.
Shibata et al (1996)	Carried out SPDT of silicon with a view to investigating the effect of crystallographic orientation upon the surface quality. They found 'pitting' in the surface of the material which corresponded to changing crystallographic orientation of the silicon. They present formulae describing the mechanism at work, stating that slip along a crystallographic plane takes place when the shear stress (caused by the shear plane in cutting) exceeds a threshold value.

Goel (2014) highlights five different challenges which must be overcome in machining silicon carbide (SiC) which are shown in table 2-7.

Table 2-7 Challenges in Machining Silicon Carbide (Source: Goel, 2014)

Challenge	Description
1	SiC has a high thermal conductivity and low thermal expansion
2	SiC is highly brittle, having a very high ratio of hardness to Young's modulus, making it more likely to fracture than to deform in a ductile way
3	The ratio of tensile strength to shear strength is low, leading to a high probability of brittle fracture
4	SiC has low fracture toughness, so poor machinability
5	Five independent slip systems are required in the machining of SiC

Patten et al (2005) were first to report successful ductile regime machining of single crystal 6H-SiC. They report a DBT phenomenon in the material, suggesting a High Pressure Phase Transformation (HPPT) in the cutting zone, allowing for ductile material removal instead of brittle. They used 2mm nose radius tools, with edge radius of 20-250nm. They were able to achieve ductile machining at depths of cut as large as 100nm, dependent upon rake angle, and observed a DBT depth of cut of about 500nm at a -45° rake angle.

Ravindra and Patten (2008) describe machining Chemically Vapour Deposited (CVD) polycrystalline SiC in order to investigate improvements in surface roughness, material removal rate (MRR) and tool wear. They found a recommended cutting strategy which involved taking 6 cutting passes over the same area, starting with deeper depths of cut and gradually taking shallower depths of cut. R_a was reduced from 1158nm to 88nm, and it was found that tool wear could be reduced both by using a cutting fluid, and by decreasing the feed rate once the surface had become smooth.

Goel et al (2012) carried out molecular dynamics simulations of SPDT of 3C-SiC to evaluate the wear mechanisms of the diamond tool in this process. They observed graphitisation of the diamond tool, caused by abrasion in cutting which causes high temperatures in the tool, leading to sp^3-sp^2 transition in the diamond tool. Luo et al (2012) performed further molecular dynamics simulations to evaluate the effect of polymorphism in SPDT of single crystal SiC. They determined that 3C-SiC was most difficult to cut, followed by 4H-SiC and then 6H-SiC (which is approximately twice as difficult to machine as silicon). They found that all polytypes considered were machinable in the ductile regime, and that they would all induce graphitisation of the diamond tool due to abrasion caused temperature rise.

Goel et al (2013) carried out SPDT of single crystal 6H-SiC at cutting speeds of 1m/s, achieving a surface finish of 9.2nm R_a, which was the best surface roughness reported on the material. Significant wear was observed on the diamond tool using a scanning electron microscope, after only 1km of cutting as shown in figure 2-12- the wear observed was flank wear, with some

rounding and recession of the edge radius. The DBT transition was identified in the cutting process using a DXR Raman microscope to view the uncut shoulder of the material, as shown in figure 2-11, which displayed cracking according to the formula of Blake and Scattergood (1990).

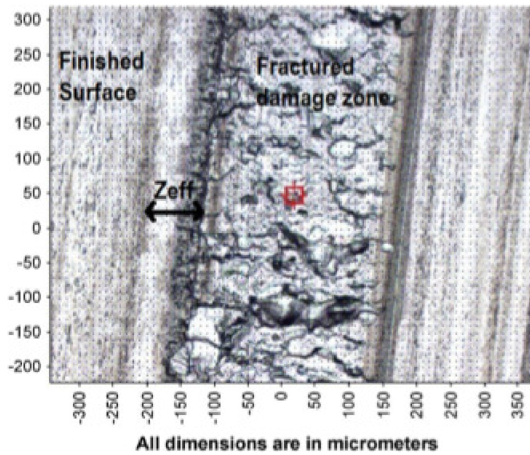

Figure 2-11 DBT in Shoulder (Goel, 2013)

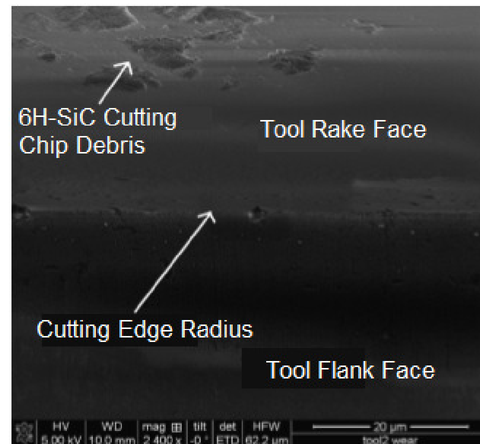

Figure 2-11 DBT in Shoulder (Goel, 2013) **Figure 2-12 1km Worn Tool (Goel, 2013)**

Goel (2014) describes how one factor influencing the successful ductile cutting of silicon carbide is the rake angle of the tool used, larger negative rake angles being more favourable. If a positive rake angle is used, this can lead to chipping of the diamond tool- and the negative rake angle is known to induce a high hydrostatic stress in the workpiece, thereby facilitating the brittle to ductile transition which is induced by hydrostatic pressure. It is noteworthy that when the depth of cut is less than the cutting edge radius, that an effective negative rake angle is induced.

2.1.4 Introduction to Hybrid Micro-Machining Methods

Several novel technologies which aim to improve ductile cutting performance of brittle materials of interest such as silicon carbide have been reported in the literature. They are summarised here to give an idea of the context in which the technology of interest is being developed.

Jeon and Lee (2012) define Thermally Assisted Machining (TAM) as using an external heat source to 'increase the temperature of the cutting area to facilitate the processing of the material'. They describe how by increasing the temperature of the substrate, the shear strength is reduced in metals, and ceramics are caused to deform more plastically (as evidenced by figure 2-14). The heat sources that were used are: 'oxyacetelyne torches, induction coils, plasma and lasers'.

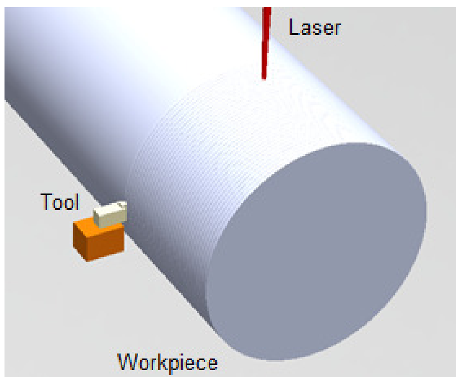

Figure 2-13 LAM

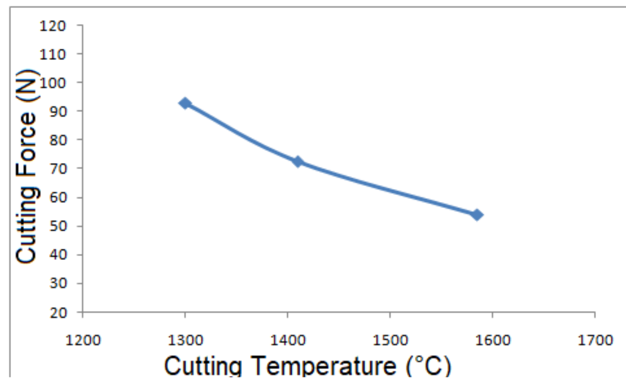

Figure 2-14 Temp vs F_c (Jeon and Lee, 2012)

Jeon and Lee (2012) also discuss Laser Assisted Machining (LAM), shown in figure 2-13, in which a laser is used to heat the material. They describe the use of CO_2, Nd:YAG, diode and excimer lasers for heating the workpiece. Jeon and Lee mention the importance of considering the absorptivity of the material being machined at the laser's wavelength, and also of using a laser of sufficient power. They also mention that it is important to consider the speed at which the laser is moving across the workpiece, as this will affect the temperature that the material reaches. Jeon and Lee discuss how reductions in flank wear of 50µm with a temperature increase of 310 °C were observed (Lei and Shin, 2001).

Lee et al (2016) present a review of 'laser-assisted milling' (shown in figure 2-15). Laser-assisted milling (LAM) is defined as a type of laser assisted machining, applied to the milling process. Similar to laser assisted machining described above, a laser is pointed onto the substrate to heat it up, thereby making it more pliable and easier to machine. In the case of LAM, the laser is pointed onto the material in front of the mill. As the mill may take a complex tool path, an additional axis must be used to control the location of the laser so that it remains focused ahead of it. The technology can be applied to a conventional drill, to an end mill or to a face mill.

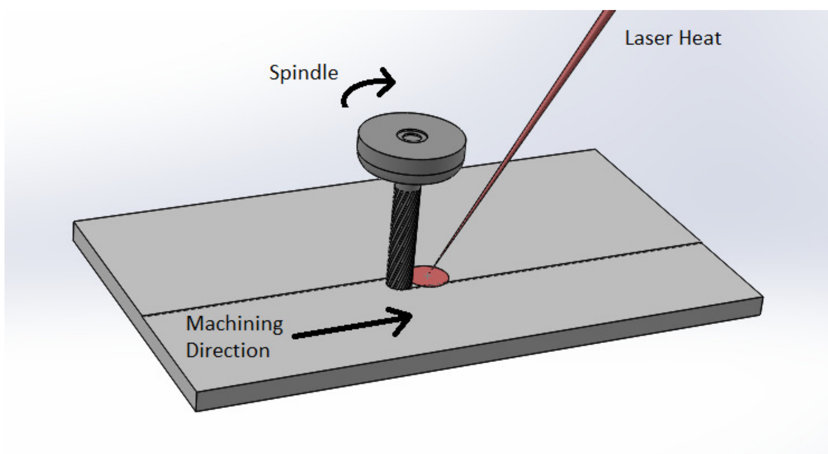

Figure 2-15 Laser Assisted Milling (Adapted from Lee et al, 2016)

Dandekar et al (2010) report the use of Laser Assisted Machining (LAM) in 'hybrid machining' (shown in figure 2-16) to machine Titanium. In their experiment, not only is the substrate heated using lasers, but the tool is also cooled using liquid nitrogen. The cooling of the tool is said to help it to keep its hardness and strength, and to reduce the tool wear (which is known to increase with temperature because of chemical reaction; Zhang et al, 2017).They report a two to threefold improvement in tool life compared to conventional machining using a carbide cutting tool.

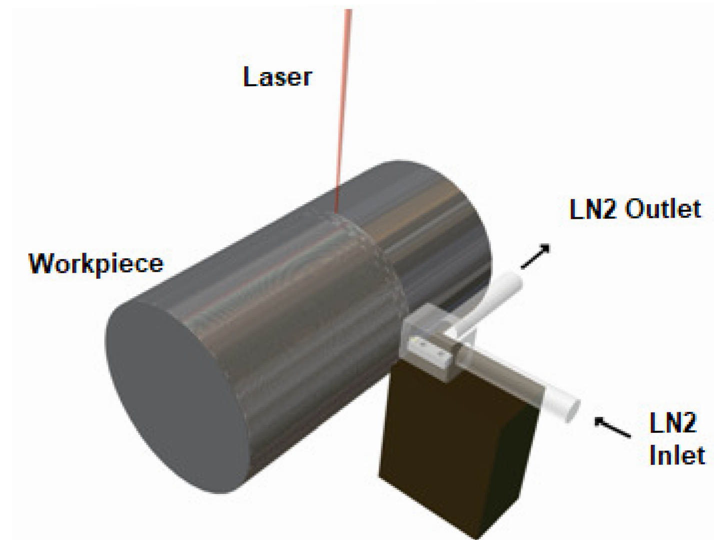

Figure 2-16 Hybrid Machining (Adapted from Dandekar et al, 2010)

Özel and Pfefferkorn (2007) present an account of Pulsed Laser Assisted Micro-milling (PLAM), in which instead of using a continuous wave (CW) laser as is normally the case, they use a pulsed laser to generate heat in the machined material to aid with cutting, particularly with reference to miniature dies/moulds. They found that while the use of laser had significant effects upon cutting forces, it also impacted negatively upon the surface finishes achievable. They found a reduction in resultant cutting forces of approximately 10N at feed rates of 5µm/rev.

Kumar et al (2011) present experimentation into laser assisted micro-grinding, in which grinding is combined with the use of lasers in order to achieve ‘three-dimensional micro-scale’ features in hard ceramics. Particularly, silicon nitride was experimented upon, and it was found that the use of lasers consistently reduced grinding forces, by as much as 43.2%; that tool wear was reduced with the use of laser; and that higher depths of cut were achievable with the use of laser as tool wear and grinding forces are reduced at these depths of cut.

The literature reveals a wide variety of techniques which are used to cut difficult-to-machine materials with improved efficacy. It is clear that while performance advantages have been gained, that the machining of sought after materials like silicon carbide remains to be achieved.

2.1.5 Elliptical Vibration Cutting

This sub-section focuses on Elliptical Vibration Cutting as this technology has had success in the cutting of difficult-to-machine materials, and because there are many variants of the technique which are introduced here. Vibration Assisted Machining (VAM) is a process by which ultra-precision machining is combined with vibration of the tool (as shown in figure 2-17), which is used to aid the machining process. The technique is said to reduce cutting forces, improve surface finish, and importantly to reduce tool wear in some cases (Brehl and Dow, 2008). It has been used to help the machining of brittle or ferrous materials, and also for creating microstructures on items such as moulds.

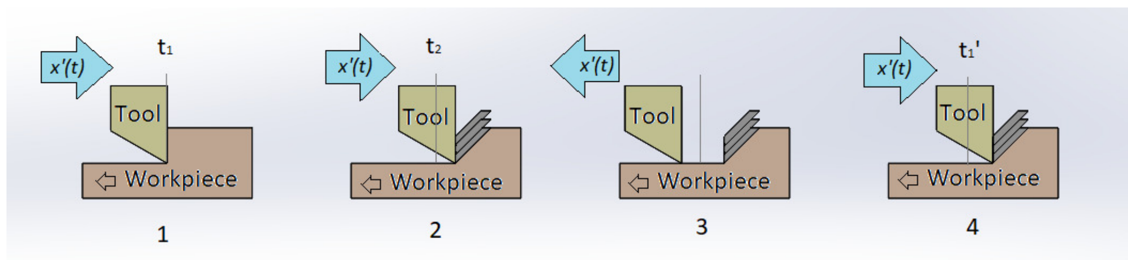

Figure 2-17 VAM (Adapted fromBrehl and Dow, 2008)

VAM works by inducing either a linear or elliptical vibrational motion in the tool, in such a way that the tool comes away from the workpiece periodically. In this way, VAM has been shown to increase the ductile-to-brittle (DBT) depth of cut limit for brittle materials. For example, improvements in surface finish brought about by VAM are shown in table 2-8 from Brehl and Dow (2007).

Table 2-8 Improvements in R_a by VAM (Source: Brehl and Dow, 2007)

Workpiece Material	Tool Material	VAM Process	Tool Nose Radius (mm)	Depth of Cut (µm)	VAM Surface Roughness	Conventional Surface Roughness
SS	Carbide	1D	0.20	50	4.3 PV	20.0 PV
Inconel	Carbide	1D	0.20	50	4.5 PV	60.0 PV
Al-SiC	SCD	1D	0.80	1	0.578 PV	0.859 PV
Fused silica	SCD	1D	0.80	2	0.100 Ra	0.260 Ra
CFRP	SCD	1D	0.50	200	2.80 Ra	4.00 Ra
LY12 (aluminium)	PCD	1D	0.50	150	0.63 Ra	0.94 Ra
304 SS	PCD	1D	0.20	20	0.152 Ra	0.239 Ra
PMMA(CR-39)	SCD	1D	NR	2	0.1 Ra	0.2 Ra

Steel	SCD	2D	1.00	3.5	0.04 Ra	0.52 Ra
Brass	SCD	2D	NR	1	0.04 Ra	1.00 Ra
Inconel	Carbide	1D	NR	800	0.284 Ra	0.510 Ra

The development of VAM is described in table 2-9.

Table 2-9 History of VAM

Authors (Date)	Development
Skelton (1968)	They used a hydraulic vibrator to oscillate a lathe tool, and found significant reductions in machining forces
Moriwaki and Shamoto (1991)	Carried out VAM diamond machining of stainless steel, which is not normally machinable using diamond because of chemical reaction. They also applied ultrasonic vibration to the cutting tool, and were able to cut a length of 1600m of stainless steel, at a surface roughness of 30nm R_{max}.
Moriwaki et al (1992)	Experimented on diamond cutting of glass using VAM (shown in figure 2-19), and found that the critical ductile-to-brittle transition (DBT) depth of cut was made deeper by using the technique
Moriwaki and Shamoto (1995)	Applied elliptical vibration at an ultrasonic frequency to the cutting tool (shown in figure 2-18). They found that the cutting force and the chip thickness were improved, and that the technique was practical to apply to ultra precision machining
Shamoto and Moriwaki (1999)	Found similar results in their application of VAM to hardened steel.

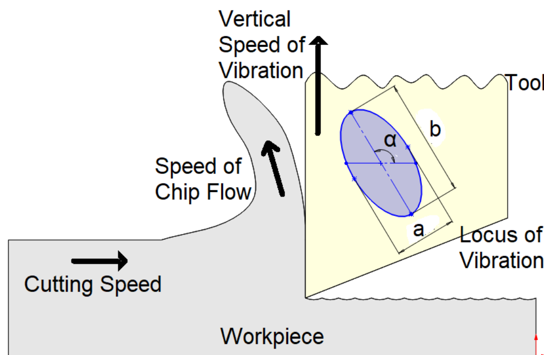

Figure 2-18 Elliptical VAM

(Adapted from Moriwaki and Shamoto, 1995)

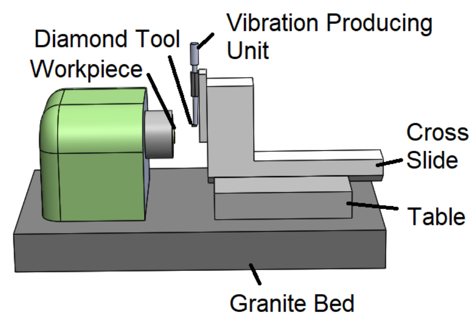

Figure 2-19 VAM

(Adapted from Moriwaki et al, 1992)

Muhammad et al (2012) present an account of Hot Ultrasonic Assisted Turning (HUAT), shown in figure 2-20, which combines heating of the substrate, with vibration of the tool at high speeds (>20kHz) in order to achieve reduction in cutting forces and improvement in surface finish. When turning a Ti15V3Cr3Al3S alloy at 300°C, they found an improvement in surface roughness (Ra) of 74% compared to conventional turning, and a reduction in cutting force of up to 88%. Their results suggested that the application of heat had more of an effect when the workpiece was being vibrated at an ultrasonic speed.

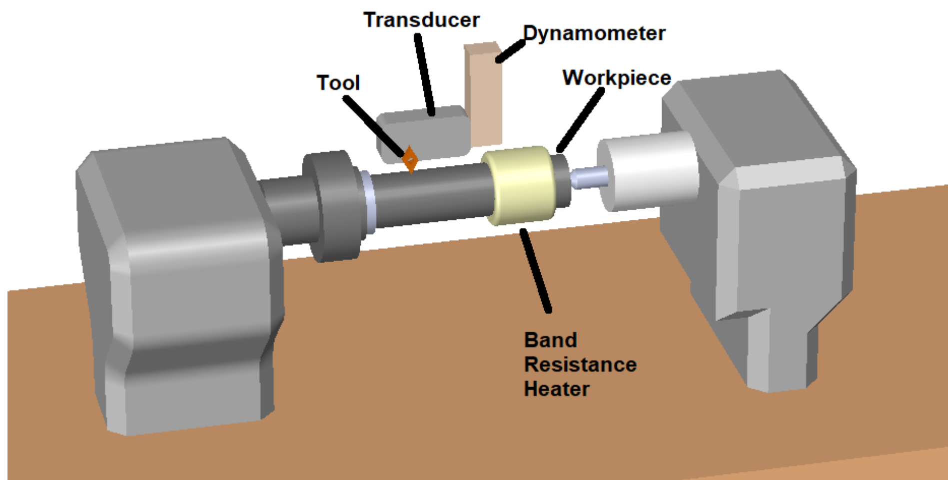

Figure 2-20 HUAT (Adapted from Muhammad et al, 2012)

Negishi (2003) describes EVAM using single crystal diamond tools being used to produce optical surface finishes upon silicon carbide. They simulated cutting by creating grooves in SiC at different depths of cut, which were then viewed with a scanning electron microscope (SEM) and measured with a profilometer. As shown in the figure below, the DBT depth of cut indicated was 3.5 μm, significantly greater than values achieved in conventional SPDT (eg 500nm by Patten, 2005). They observed a wear land on the tool of approximately 400nm after only 196mm cutting distance.

2.1.6 Fly-Cutting

Zhang et al (2016) provide a comprehensive review of diamond fly cutting, or Ultra Precision Fly Cutting (UPFC) as it is termed in the literature, which forms the basis for this section. They highlight that UPFC is a process which is capable of producing large flat surfaces (in end-UPFC) or freeform surfaces (in Ultra Precision Raster Milling, UPRM); and is capable of producing 'sub-micrometric' form error, and nanometric surface roughness (the differences between these two processes are shown in Figures 2-21 and 2-22).

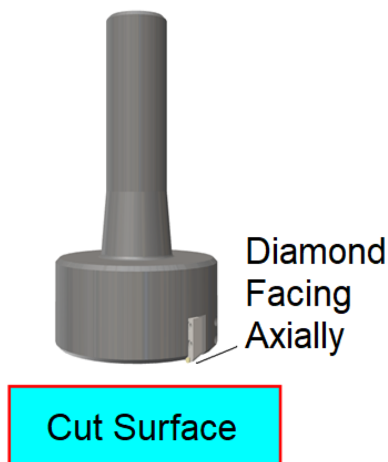

Figure 2-21 UPFC Fly Cutter

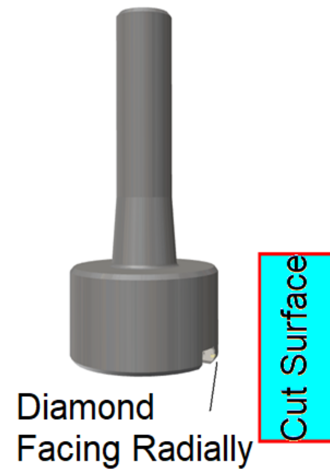

Figure 2-22 UPRM Fly Cutter

Brinksmeier et al (2002) present an account of fly-cutting which is partly the motivation for this research. They use a fly-cutter which is novel because it does not have a single tool, but four tools rotating on the same fly-cutter as shown in figure 2-23. They use this tool to cut the '3m reflector of the KOSMA submillimeter telescope', and describe cutting at 3600rpm, with four 12mm nose radius diamond tools, completing each large telescope mirror in 3:45hr, and at a form accuracy better than 5µm.

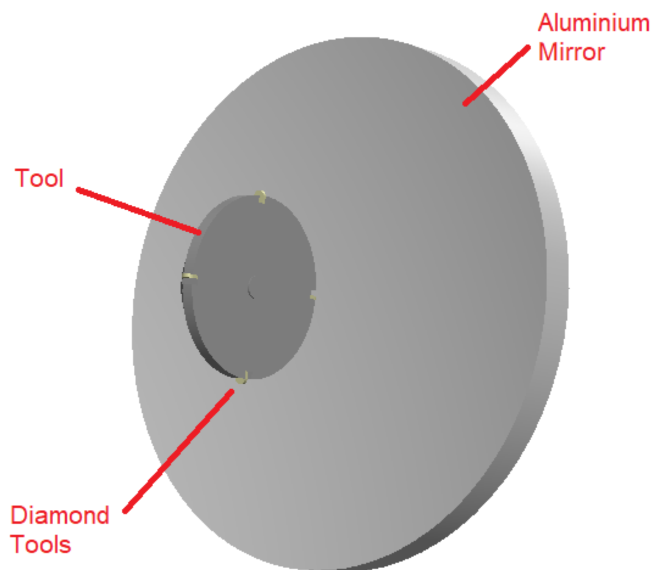

Figure 2-23 Cutting of Aluminium Mirror with Multi-Diamond Tool (Adapted Brinksmeier et al, 2002)

2.1.7 μ-LAM

Ravindra (2011) carried out extensive investigations into μ-LAM, which are central to the current investigation. μ-LAM is differentiated from Laser Assisted Machining (LAM) in that as diamond is transparent to laser light, the laser is passed directly through the diamond onto the cutting zone as shown in figure 2-24 below. In this case, laser light is absorbed by the high pressure phase transformation (HPPT) zone (induced by the brittle to ductile transition), in which in the case of silicon and silicon carbide there is a phase change in the material, and in which more light is absorbed than in the surrounding material. An advantage of μ-LAM is that it allows for heating of only a very small area on the substrate, thereby minimising the effects of thermal distortion of the workpiece.

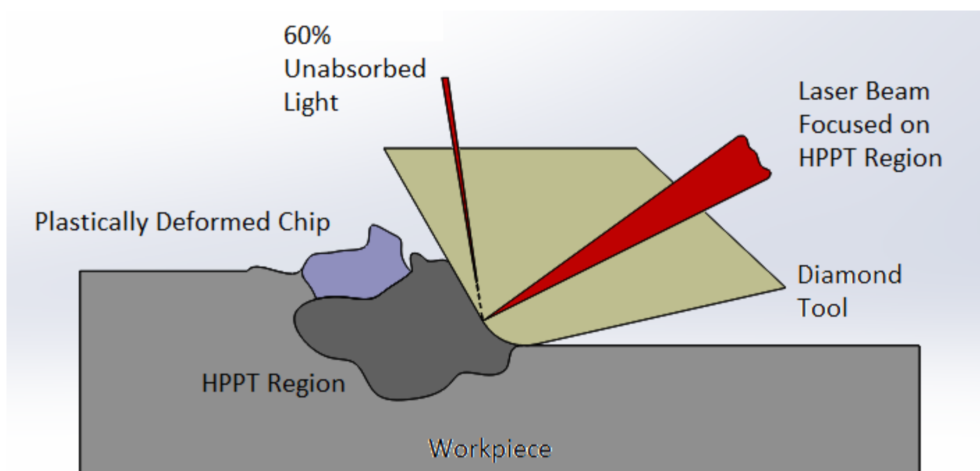

Figure 2-24 Diagram Illustrating μ-LAM (Adapted from Ravindra, 2011)

Ravindra's (2011) investigation looked at many different aspects of μ-LAM using scratch tests, where SPDT was simulated using actual diamond cutting tools, and simulating cutting conditions by varying cutting and thrust forces. A drawback of the investigation is that the cutting speeds employed were considerably slower than actual machining parameters, so the question remained whether realistic cutting speeds would negate any effect of the laser- although this was later disproved by the subsequent study of Mohammadi et al (2015).

Noteworthy in the principle of μ-LAM is that the spot size of the laser must be proportional to the size of the HPPT zone so that it is preferentially absorbed, as the HPPT zone is known to have higher absorptivity. Another reason why the laser must be focused to such a small spot is that it ensures that only the part of the substrate which is covered with the diamond tool, therefore not in the presence of oxygen, will be heated- thereby avoiding combustion. The size of the HPPT zone is estimated to be equivalent to the size of the width of cut or feed rate, therefore the spot size must be as small as these.

The results of Ravindra's (2011) study (some of which are shown in figure 2-25), which concerned µ-LAM mainly of silicon and silicon carbide, included a consistent increase in the depth at which the ductile to brittle transitions occurred by using laser (of up to 176%); a consistent increase in depth of cut for a fixed thrust force through using laser, although this rarely resulted in an increase in cutting forces. Ravindra identified the mechanism by which µ-LAM seemed to be operating, that of preferentially heating the high pressure phase of the material in the cutting region (this having a higher absorption rate). Ravindra identified that the temperature required for µ-LAM to be effective seemed to be >1038°C for both silicon and silicon carbide.

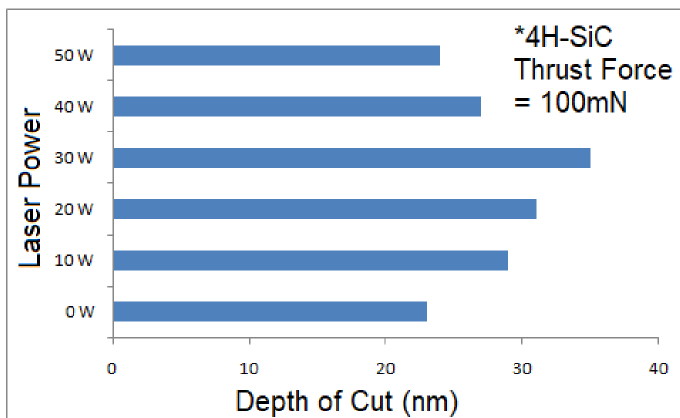

Figure 2-25 Laser Effect on depth of cut (Adapted from Ravindra, 2011)

Ravindra found the optimised laser powers shown in table 2-10 (in terms of depth of cut) when cutting with a 1.3-1.5mm nose radius tool for silicon and a 1mm nose radius tool for SiC, in both cases at 1µm/sec with a -45° rake angle and 5° clearance angle. It is noteworthy that the optimised values were determined as those which used the highest laser power possible without melting the material.

Table 2-10 Optimised Laser Powers at λ ~1µm, (Ravindra, 2011)

Material	**Optimised Laser Power (W)**
Single crystal silicon	45
Single crystal 4H-SiC	30
Single crystal 6H-SiC	20
Polycrystalline CVD coated 3C-SiC	10

The DBT depths of materials of interest with optimal µ-LAM powers presented by Ravindra (2011) are shown in table 2-11.

Table 2-11 DBT Depths of Cut With Laser (Based on Ravindra, 2011)

Material	DBT Depth without Laser (nm)	DBT Depth with Optimal Laser Power (nm)
4H-SiC	20.0 nm	40.0
6H-SiC	17.5 nm	26.0
3C-SiC	42.5 nm	117.5
Silicon	185.0 nm	260.0

Ravindra also presented a formula to calculate the Power Density incorporating the cutting speed, this formula is:

$$q = \frac{P}{A \times V_c} \qquad \textbf{(2-1)}$$

Where q is power density (W/m^2), P is laser power (W), A is Area of focused laser spot (m^2), V_c is cutting speed (m/s)

The question that Ravindra's (2011) study left open was whether the technology would be effective in actual machining rather than just in scratch tests. This question was answered to a certain extent in his later research paper, Mohammadi et al (2015), in which µ-LAM was implemented on a SPDT machine for turning silicon. The results showed an improvement of 80% in the surface roughness of the machined material, although they did not report on improvements in the ductile to brittle transition depth of the material or other outcomes.

Table 2-12 compares the power values that formula 2-1 gives at lower cutting speeds as in Ravindra's study, with those obtained in higher speed cutting (eg 2.9m/s). The table below shows the disparity in results obtained, which is one of the factors that has prompted further investigation into this.

Table 2-12 Comparison of PD with Different Machining Parameters

	Ravindra, (2011)	Ravindra, (2011)	Ravindra, (2011)	Mohammadi et al. (2015)
Spot Diameter (µm)	10	10	10	10
Power (W)	45	50	55	20
Cutting Speed (µm/s)	1	2	5	3 (m/s)
Power Density	572958	318310	140056	0.087

Shayan et al (2009) carried out similar scratch tests using µ-LAM, and they obtained results which corroborate those of Ravindra (2011). Shayan et al used a White Light Interferometer and Atomic Force Microscopy (AFM) to measure the depth and width of scratches which had been made on 4H-SiC. They used a low power (400mW), 1480nm wavelength laser, and they also measured the cutting and thrust forces. Their findings included significantly reduced cutting forces.

An interesting phenomenon observed in Ravindra's (2011) study was that while many of the cut regions, when their Raman spectra were analysed, revealed that amorphous silicon was left (as would be expected), some revealed that pristine silicon remained- suggesting an annealing effect of the laser. A research paper which corroborates this is Thompson et al's (1987), in which they suggest that if lasers are shone on amorphous silicon at power densities below those required to fully melt the material, that this can lead to 'explosive crystallization', in which a liquid layer travels through the material, creating 'fine grained polycrystalline Si'.

2.1.8 Knowledge Gaps and Research Questions

There are several knowledge gaps and research questions which arise from an inspection of the literature relevant to single point diamond turning, the machining of hard/brittle materials, fly cutting and µ-LAM, which include:

- How to effectively machine materials such as silicon carbide which currently cause excessive diamond tool wear
- What the relationship is between laser power, heating of the substrate and performance of µ-LAM, and how to determine this
- What effects wavelength of laser has upon µ-LAM

The primary knowledge gap concerns the method of machining the important difficult-to-machine materials such as silicon carbide, which is not currently machinable in large areas, and for which there is a significant demand. While a wide variety of novel technologies have been presented which aim to achieve this goal, effective machining of the material is not yet achievable- so there is a demand for a methodology which can be used to achieve this.

The extent to which µ-LAM meets this objective is not yet determined, as there are few accounts of experimental investigation involving realistic cutting conditions, and the technology is still developing. As such there are knowledge gaps concerning the optimisation of this technique- such as the way in which laser power relates to the effectiveness of µ-LAM, the methodology that should be used to specify the wavelength of laser light, how best to determine the optimum parameters to be used with this technique and the extent to which limitations are imposed upon µ-LAM performance by phenomenon such as thermal shock or increased chemical wear at higher temperatures.

With regard to µ-LAM, a significant question remains about how best to analytically describe the intensity of laser with respect to the effect that this will have upon cutting performance. As discussed previously, Ravindra's (2011) formula does not seem to accurately predict the effect of laser power upon heating and cutting. It can easily be seen how, with the development of the technology, there is a need to be able to set the laser power so as to gain optimal µ-LAM performance, but the analytical basis to do this has not yet been presented in the literature. It is necessary to determine a methodology to predict the heating caused in the substrate by lasers of different characteristics when travelling at known speeds, and from the temperature induced to be able to predict the effectiveness of µ-LAM using different cutting parameters in different materials (ie cutting forces and DBT depths for different conditions of tool wear). In answering these research questions it is possible to predict the performance of µ-LAM under different cutting conditions, which is necessary for enabling better cutting performance of sought after difficult-to-machine materials (such as silicon carbide).

An analogous situation exists with respect to the effect of laser wavelength upon the performance of µ-LAM. While lasers with wavelengths of 1000nm have most commonly been used for µ-LAM in the literature, there is scope for investigation of the effect of using different wavelengths. Jeon and Lee (2012) describe how Nd:YAG lasers (~1000nm) offer the advantage of being fibre coupled and can be applied to ceramics and metals, but an in-depth justification for the choice of laser wavelength has not yet been presented. Moreover, there is a demand for a conceptual framework which describes the effect that lasers of different wavelengths can have upon the effectiveness of µ-LAM for different materials.

3 RESEARCH METHODOLOGY

3.1 Design Specifications and Assumptions

In order to create the tool in a feasible way, it was first necessary to create a design specification. Key characteristics that were considered in this regard were material removal rate (MRR), surface roughness, heating caused in substrates of different materials, the size of components machinable, and the type of machining operation (whether creating a 2D or 3D geometry), this was done with consideration of the materials of primary interest- silicon and silicon carbide.

MRR was determined to be significant because it represents the speed at which the manufacturing technique can be carried out, thereby limiting the usefulness of the process if a minimum value is not adhered to. It was important to ensure that surface finishes of high enough quality are attainable to determine the usefulness of the process in terms of producing parts which are of superior finish.

The accuracy in the Z direction was specified because this accuracy determines how shallow the minimum depths of cut are that can be taken, so this characteristic will determine whether the brittle materials of interest can be machined in the ductile regime. The heating required in the substrate was specified because without sufficient heating the effectiveness of µ-LAM would be limited, and as sufficient depth of penetration of laser is also required for effective heating to take place, this parameter was specified also. The final four parameters specified are all design choices which do not involve analytical calculations, so they are determined in this section.

The specifications selected for the tool is shown in table 3-1, followed by the rationale behind the requirements determined:

Table 3-1 Specification for Installed Tool

Characteristic	**Requirement**	**Units**
MRR	1-100	mm^3/min
Surface Roughness	<10 (80)	nm RMS (Rt)
Accuracy in Z direction	<40	nm
Heating in substrate	Silicon = 1414	°C
	Silicon Carbide = 2730	°C
Depth of penetration of laser	Silicon = 260.0	nm
	Silicon Carbide = 117.5	nm
Spot size of laser	Equal to or smaller thanfeed rate in all cases	-
Size of substrates	120 * 120	mm
Geometry created	2D	-
Number of diamonds	3+	-
Time for spindle to reach speed	20	s

The specifications for MRR and surface roughness were selected so that the process put forward would compare favourably with diamond turning (as shown in figure 3-1), which is a competing process.

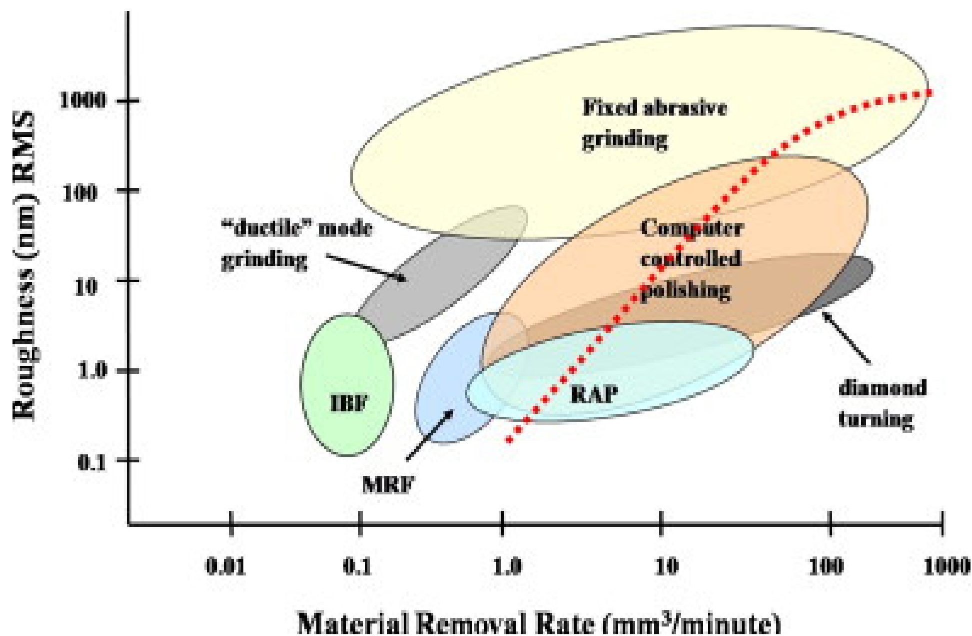

Figure 3-1 Machining Processes Evaluated (Comley et al, 2011)

With regards to the accuracy in the Z direction for the tool and the machine tool that it was to be implemented on, it was determined that this should be better than 40nm. This decision was made with reference to the DBT depths of cut for silicon and polytypes of silicon carbide. The smallest of these with optimal laser heating is 26nm (Ravindra, 2011). It was predicted that by ensuring accuracies of 40nm that it would be possible to cut a large number of ceramics in the ductile regime using µ-LAM.

It was determined that the laser components selected should be capable of heating the surface of the substrates to their melting temperatures (1414°C for silicon, 2730°C for silicon carbide). It was decided that it should be possible to cause this temperature at the surface of the material being cut, because Ravindra (2011) had identified that the optimal temperature for µ-LAM was that which was reached immediately preceding the materials melting.

With regards to the depth of absorption of the laser into the substrate, it was determined that it should be ensured that this exceeded the DBT depths of cut for both silicon and silicon carbide. This is because the laser must act to a depth at least equal to the depth of cut, but that heating beyond this depth is unlikely to be relevant.

With regards to the spot size, it was determined that this should be kept to the same size as the feed rate proposed. This decision was made because Ravindra's (2011) study had indicated that it was necessary to heat the HPPT region under the diamond tool only, and this is approximately the size of the feed rate. Ravindra (2011) considered the spot size as being limited by the size of the width of cut taken, but in the present study the spot size is set to be limited by the feed rate applied. This is because the feed rate represents the distance of

material which is being removed at the tip of the diamond, whereas the width of cut is larger, including some area in which material has already been removed. As laser can cause combustion in the presence of oxygen (where material is not present) the feed rate is taken as the dimension limiting the spot size, to ensure the laser spot comes into contact with the substrate material only.

It was determined that the substrate should have a size of 120 x 120mm. It was decided that it should be possible to cut a surface area analogous to larger components which cannot currently be processed using SPDT. As such, 2m^2 was selected as the surface area that should be possible to machine. Because this area is extremely large given the constraints of most machine tools, an alternative approach is suggested in which a smaller substrate could be machined in successive layers, as shown in figure 3-2, so that the machining of a larger substrate could be simulated.

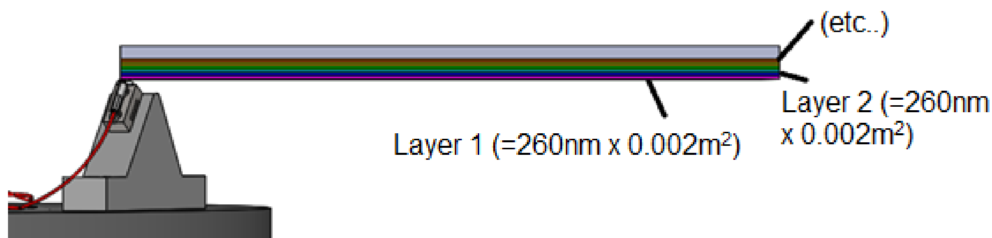

Figure 3-2 Layers Cut on Substrate

With regards to the geometry of the substrates cut, it was decided that a 2D facing cut would be most appropriate because this reduces the complexity of the operation. While the option of implementing 3D cuts could be used, it was determined that designing for 2D cuts would suffice to prove that implementation of the tool is feasible without involving non-relevant design. It was decided to use 3 diamond tools as a minimum because odd numbers of diamond tools avoid reflective symmetry in the tool (although rotational symmetry is maintained), which can avoid some modes of vibration of the tool; and more than one diamond tool is necessary to incorporate the two aspects of the concept of the tool.

3.2 Design Methodology

3.2.1 Specification of the Machine Tool

Several different machines were considered for implementation of the multi-turret µ-LAM machine, including Cranfield University's BoX, µ4, Edgetek SAM, and CUPE Nanocentre. A Pugh matrix (Burge, 2009) was created in order to select the machine.

Various different criteria were important for selecting the machine that could be used for the tool- including accuracy of axes, possibility of passing fibre optic cable through the spindle, ease of access, the torque and spindle speed of the machine, the motion of the axes and the size of

component machinable. These different characteristics were weighed up according to their importance for the project on a scale of 1-5. Characteristics that were vital to the successful implementation of the tool were awarded a score of 5, with those which were less vital being awarded lower scores, as justified in table 3-2. The machines were subsequently rated in terms of each characteristic, and a weighted score was determined for each machine.

Table 3-2 Weighting for Machine Selection

Characteristic	Score	Justification
Accuracy of Axes	5	High accuracy required for shallow depth of cut (ductile machining of brittle materials)
Motion of Axes	5	Without adequate motion of axes machining not possible
Passing Fibre Optic Through Spindle	5	This is essential for to implement the tool, as laser feed cannot be provided by any other means
Ease of Access	1	Only important in implementation of the tool
Spindle Torque	1	Only minimal cutting forces involved and no large moving masses on the spindle
Spindle Speed	3	High speed desirable to enable high MRR
Size of Workpiece	4	Necessary to enable significant areas to be cut, but multiple layers can be taken to simulate larger areas

The different machines which were considered are displayed in figures 3-3 to 3-7, and a summary of each machine's specifications is reproduced in tables 3-3 to 3-7 from various sources, which inform the decision made in the Pugh matrix.

Figure 3-3 Edgetek SAM (Tonnellier, 2009)

Figure 3-4 BoX Machine (Tonnellier, 2009)

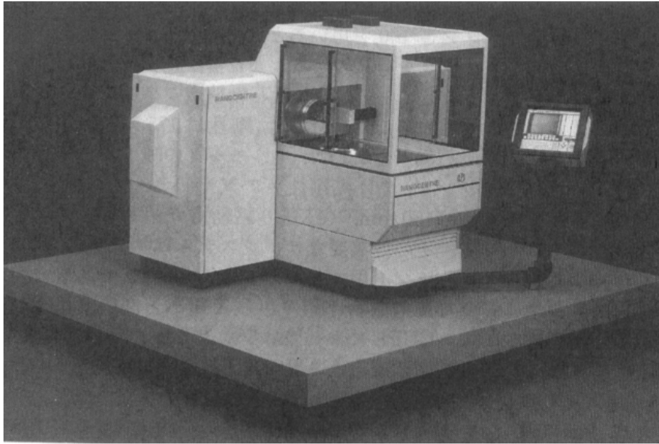

Figure 3-5 Nanocentre (McKeown et al, 1990)

Figure 3-6 µ6 (Morantz, 2017)

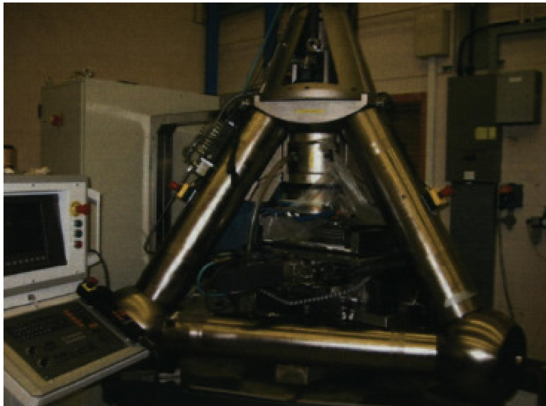

Figure 3-7 Tetraform C (Arai, 2004)

Table 3-3 Edgetek SAM (Tonnellier, 2009)

X axis travel (mm)	Y axis travel (mm)	Z axis travel (mm)	Spindle Power (kW)	Feed Rate (mm/s)	Positoning Accuracy (mm/300mm)	Positoning Accuracy (mm/300mm)	Positoning Accuracy (mm)
472	350	305	27	0 to 66	+/- 0.005	0.005	0.001

Table 3-4 BoX (Tonnellier, 2009)

X Axis Travel (mm)	X Axis Speed (mm/s)	Z Axis Travel (mm)	Z Axis Speed (mm/s)	Rotary Table Torque (Nm)	Rotary Table Speed (rpm)	Spindle Power (kW)	Spindle Speed (rpm)	Repeat-ability Accuracy (µm)
1350	0 to 50	120	0 to 20	878	0 to 25	10	100-2600	0.1

Table 3-5 Nanocentre (McKeown et al, 1990)

X Axis Travel (mm)	X Axis Resolution (nm)	Z Axis Travel (mm)	Interferom-eter Resolution (nm)	B Axis Rotary Travel (°)	B Axis Rotary Resoultion (Arc Sec)	Com-ponent capacity (mm)
350	1.25	260	1.25	360	0.1	250 x 250

Table 3-6 µ6 (Morantz, 2017)

Workpiece Surface Finish (nm S_a)	Form Accuracy (nm RMS)	Diamond Turning Spindle Speed (rpm)	Milling Speed Capability (rpm)	Turning Workpiece Size Capacity (mm)	Milling Workpiece Size Capacity (mm)
1	100	3000	>300000	150 x 150	150 x 150

Table 3-7 Tetraform C (Arai, 2004)

X Axis Positioning Accuracy (µm)	X Axis Encoder Resolution (nm)	Y Axis Positioning Accuracy (µm)	Y Axis Encoder Resolution (nm)	Workpiece Size Capacity (mm)	Z Axis Accuracy (µm)
1	10	1	10	150 x 150	1

Several different machine tools were initially considered for the implementation of the multi-turret µ-LAM tool. Before the design of the tool had advanced beyond the conceptual stage, a design was considered whereby an electrical slip ring was used (shown in figure 3-9), which would have avoided the need to pass the fibre optic cable through the centre of the spindle of the machine (as in the design shown in figure 3-8)- thereby allowing more machines to be considered.

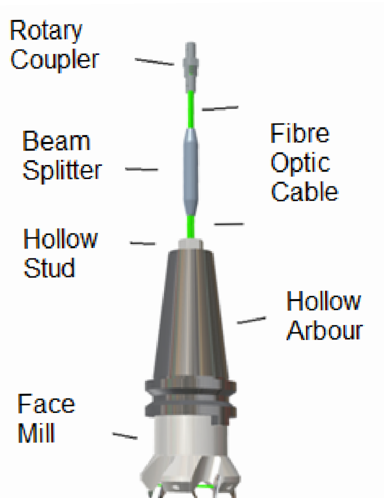

Figure 3-8 Cable Through Spindle

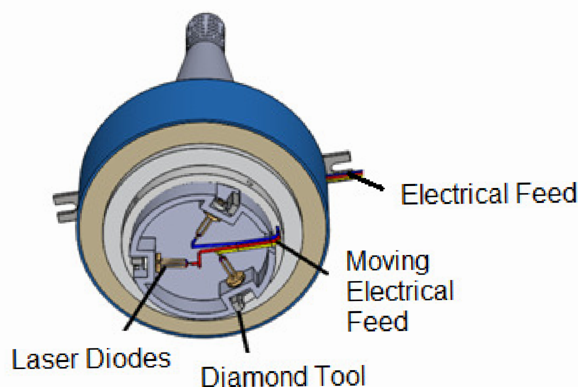

Figure 3-9 Electrical Slip Ring

It was realised that this option was impractical as the laser diodes that would need to be used are not capable of focusing the laser beam to a small enough spot size. Therefore, one of the ultimate requirements for the machine tool was that it be possible to pass a fibre optic cable through the centre of its spindle. The different machines considered are shown in the Pugh matrix (Burge, 2009) in table 3-8, where the favourability in terms of the different characteristics are rated from 0 (low) to 5 (high):

Table 3-8 Pugh matrix for different machines considered

Machine	Fibre through spindle (x5)	Torque (x1)	Spindle Speed (x3)	Ease of Acces s (x1)	Motion of axes (x5)	Accuracy of axes (x5)	Size of workpiece (x4)	Total
µ4	0	5	5	1	5	4	1	70
BoX	0	5	1	3	5	2	5	66
Edgetek SAM	0	5	5	3	3	3	3	65
Nano-centre	5	5	5	3	3	5	3	100
Tetra-form C	5	5	5	5	5	3	3	102

The CUPE Nanocentre was considered as an option for the implementation of the tool, as the Nanocentre allows for extremely shallow depths of cut to be achieved, which is ideal for machining hard and brittle materials in the ductile regime. The decision was made to opt for the Tetraform C machine. An alternative spindle was selected which would allow for the fibre optic cable to pass through its centre. The Tetraform C offers superior stiffness, and has been known

for ductile regime grinding of ceramics as a result of this (Arai, 2004). The Tetraform C, unfortunately, offered only 1µm accuracy in the Z direction, which exceeds the requirement for ductile machining. The accuracy of the Tetraform C in the X direction is 1µm.

3.3 Design Process

3.3.1 Laser Photonics Optical Design

It was necessary to perform calculations which would determine the specification of the optical components selected. Two separate optical designs are presented, the first concerning laser light used at the conventional wavelength of 1000nm, and the second involving the optimisations of the wavelength of light. Optical components are later selected in section 4.2.1 based upon each of these designs, such that two interchangeable options are presented for the optical design of the tool. The calculations for the second, more complex optical design, use optical data for pristine silicon because of its availability, although the use of data for amorphous silicon would be more appropriate. It is anticipated that the same design could be implemented for other materials of interest, namely the polytypes of silicon carbide and their different phases by following the methodology of Green (2008) in which he predicts absorptivity data based upon previous experimental findings. This is beyond the scope of the current investigation, where pristine silicon is used as a material to illustrate the optical design concept proposed.

For the basic optical design, it was necessary to specify the wavelength of light used and the power of laser required. In order to do this, the absorptivity of the materials of interest was first calculated, shown graphically in figure 4-1 as the absorptivity of α-Si at different wavelengths. The heating was then predicted, shown in the table in figure 4-9 and 4-4, which show the time predicted for the material to reach melting temperature. The depth of absorption was also calculated as shown in figure 4-2, which shows the depth of absorption in α-Si according to the wavelength of laser used; and the loss of intensity of laser light below the surface of α-Si was shown graphically in figure 4-3, demonstrating whether effective heating would occur beneath the surface of the material. The relevant formulae are:

$$\alpha = \frac{4\pi nk}{\lambda} \tag{3-1}$$

(Li and Li, 2011)

Where α is the absorption coefficient (/m), n is the material's refractive index, k is the imaginary component of the complex refractive index, and λ is the wavelength of the light (m).

$$l = \frac{1}{\alpha}$$

(3-2)

(Li and Li, 2011)

Where l is the absorption depth (m)

The temperature increase in a material can be calculated with the following formula:

$$T = T_0 + \frac{\alpha q t (1 - R_l) e^{-\alpha z}}{\rho C_P}$$ **(3-3)**

(Li and Li, 2011)

Where T_0 is the initial temperature (°C), α is the absorptivity (/m), t is dwell time (s), q is the power density (W/m^2), R_l is the reflectance, z is the distance beneath the surface (m), ρ is the density (kg/m^3), and C_P the specific heat capacity (J/kg.°K).

Because of the availability of lasers and laser components at a wavelength of 1000nm, it was decided to assess whether this wavelength would be suitable for use. The absorptivity at this wavelength was first assessed for amorphous silicon, this being the constituent material of the HPPT zone in μ-LAM of silicon. The depth of absorption was compared with cutting depths which are known to be used for these materials (from Ravindra, 2011) to ensure that light would be absorbed to a sufficient depth. The dwell time for the laser upon a given patch of material was approximated with the formula below (the cutting speed was calculated in later sections of the report).

$$t = \frac{d_s}{V_C}$$ **(3-4)**

Where V_C is cutting speed (m/s), and d_s is spot diameter (m)

Minimum spot diameter was predicted (based upon optical components selected later) using the formula:

$$D_{\min} = \frac{2 \times \lambda}{\pi \times \frac{D}{2 \times f_l}}$$ **(3-5)**

Where f_l is lens focal length (m), D is beam diameter (m), λ is wavelength (m)

Having determined the minimum dwell time, the laser power was determined at which the temperature would reach the melting temperature of the material (it being indicated by Ravindra in 2011 that the optimal temperature for μ-LAM occurred immediately preceding melting of the

material). These calculations formed the basis of the selection of components in the assembly of the mechanical and optical design in section 4.3.1.

The second optical design presented concerns the manipulation of the heating rate by changes in absorptivity which occur with heating of the material. Figures 3-10 and 3-11 illustrate how the heating of silicon, for example, increases exponentially because the absorptivity of the material raises as it is heated (at 1000nm wavelength).

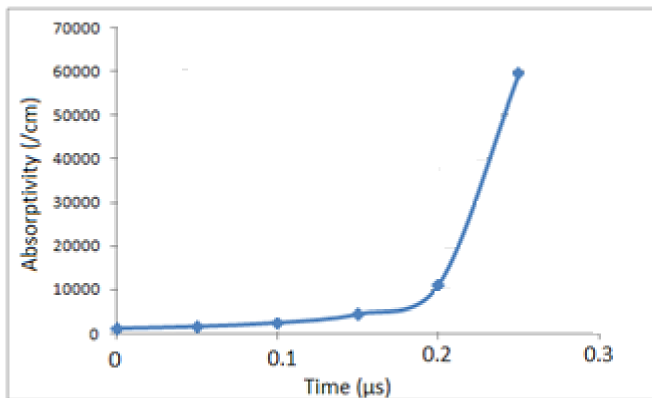

Figure 3-10 Exponentially Increasing Absorptivity for Silicon

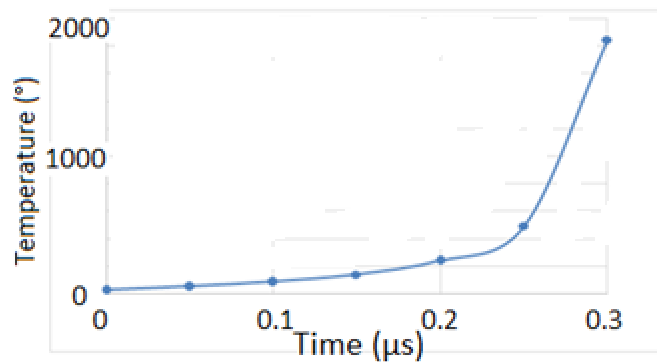

Figure 3-11 Exponentially Increasing Temperature

The rate of the increase in absorptivity differs depending upon the wavelength of the laser light (Green, 2008), and there are some wavelengths at which silicon actually absorbs less with increasing temperature, and some at which the absorptivity remains constant with changing temperature, as shown in figures 3-12 and 3-13.

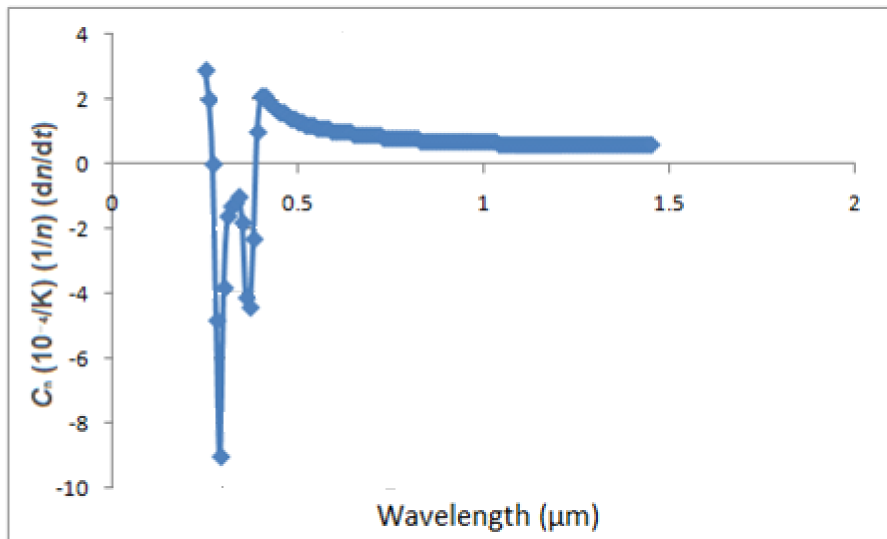

Figure 3-12 Rate of Change of Refractive Index with ΔT (Green, 2008)

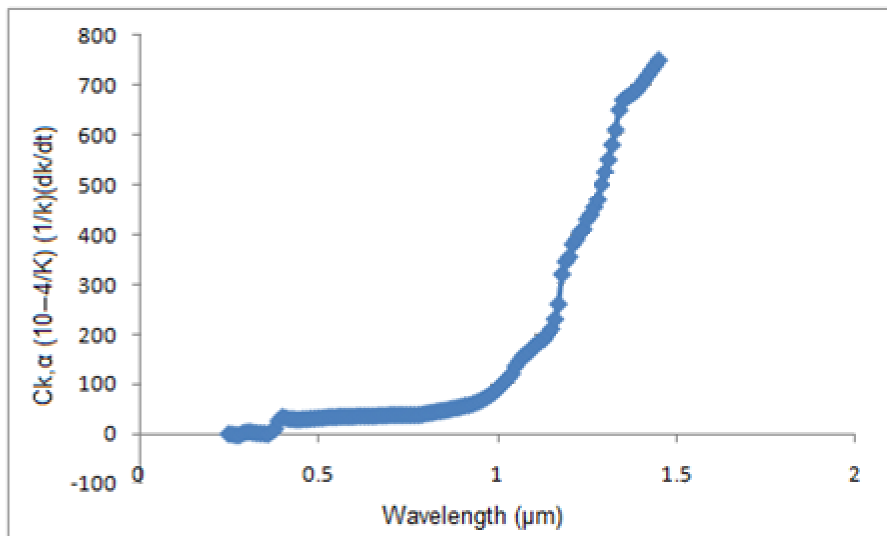

Figure 3-13 Rate of Change of Complex Refractive Index ΔT (Green, 2008)

In the second design, the phenomenon of decreasing absorptivity with increasing temperature is exploited to enable a constant temperature, marginally below the melting temperature, to be maintained in the substrate during machining. This is done by selecting the wavelength such that in silicon the absorptivity reduces to zero just before the material reaches its melting temperature, as illustrated in figures 3-14 and 3-15.

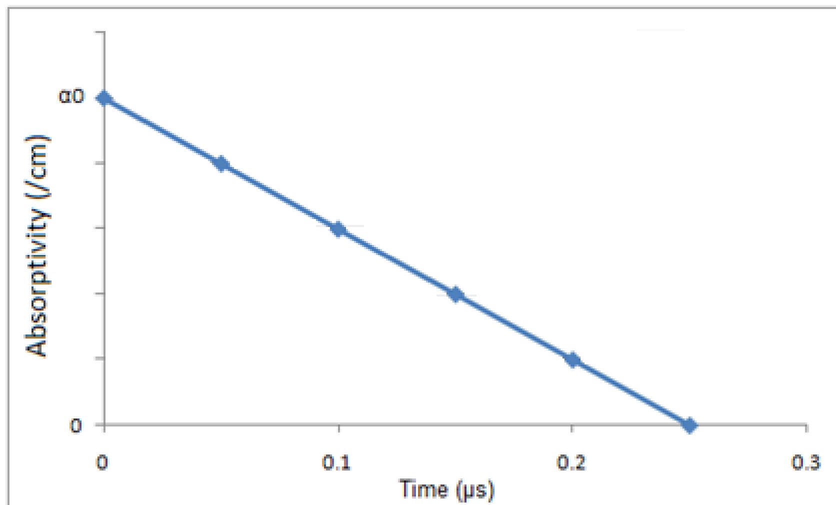

Figure 3-14 Decreasing Absorptivity

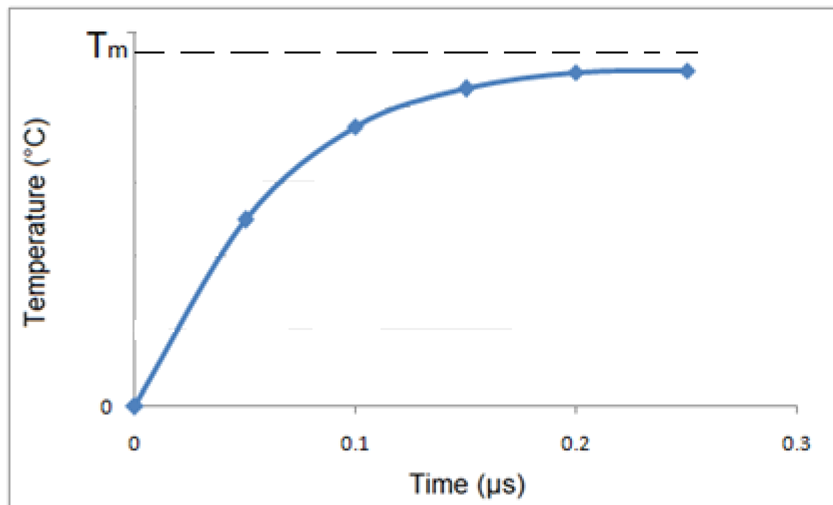

Figure 3-15 Stabilising Temperature

Using this concept, it is possible to use an overpowered laser so that the temperature is maintained at a maximum value regardless of the dwell time of the laser upon the substrate, because the material reaches its maximum temperature relatively quickly. This is particularly useful as in SPDT the cutting speed normally varies as the radial distance of the tool on the workpiece alters during machining, so by using this design it is possible to maintain a constant temperature (and therefore μ-LAM performance) regardless of cutting speed.

The formula given by Green (2008) is used to determine the change in refractive index for a given change in temperature:

$$p(T_0 + \Delta T) = p(T_0)(1 + c_P \Delta T) \qquad \textbf{(3-6)}$$

Where p is the parameter of interest (n or k), T_0 is the initial temperature (°C), ΔT is the change in temperature (°C), c_p is the is the rate of change of the given parameter as detailed in Green (2008)

Green (2008) provides data for values of n and k for pristine silicon at 300°K across a wide range of wavelengths. Lines of best fit were applied to this data, and also to the data in graphs 3-10 and 3-11 for rates of change of refractive indices with temperature increase. As such, by rearranging the formula above, it was possible to create graphs (figures 4-9 to 4-11) to determine wavelengths at which one of the refractive indices (and therefore the absorptivity) reduced to zero at a given temperature. This was done for a temperature approaching the melting temperature of silicon, to determine a wavelength of laser light that could be used.

Having specified the wavelength of laser light that could be used, it was necessary to ensure that sufficient heating occurred during the time that the substrate was exposed to the laser. An incremental heating analysis was carried out using formula 3-6 such that incremental dwell times were adjusted so that a small proportion of the heating required was carried out in each step, producing a graph showing the time estimated to be taken for heating to the maximum temperature. Formula 3-3 is used with a reflectance of 60% (as indicated by Ravindra, 2011). Graphs were produced for lasers of different powers, thereby determining the power at which the design would provide adequate heating to enable effective µ-LAM.

To summarise, the optical parameters were selected based upon the analysis in this section, including the wavelength and powers of laser light used in two separate designs, one of which involves a novel concept.

3.3.2 Mechanical Cutting Parameter Design

In this section, the mechanical design for the tool without laser heating is presented, thereby enabling selection of the mechanical components and predictions of the cutting performance.

Bifano (1989) introduced a formula for estimating the critical depth of cut for materials beyond which they would respond in a brittle way:

$$dc = 0.15 \frac{E}{H} (\frac{K_C}{H})^2 \tag{3-7}$$

Where dc is the depth of cut (m), E is the Young's modulus (Pa), H is the material hardness (J/m^2), and K_c is the fracture toughness

A limitation to the above formula is that it does not consider feed rate in the prediction of the DBT, which is also an important factor. Using the formula, a table was created indicating the critical depths of cut for the materials of interest. Ravindra's (2011) experimentally determined depths of cut for the DBT transition were also shown for comparison.

An important consideration is that feed rate is limited in SPDT by crack propagation, because at excessively large feed rates cracks propagate beneath the machined surface, resulting in sub-surface damage. Graphs shown in figures 4-14 to 4-17 were created showing the maximum feed rate for different depths of cut in 3C, 4H, 6H SiC and Si, using tools of different nose radius. The maximum feed rate is calculated according to the following formula:

$$s_{\max} = dc\sqrt{\frac{R}{2(dc + y_c)}} \tag{3-8}$$

(Blake and Scattergood, 1990)

Where S_{max} is the maximum feed rate (m/rev), R is tool nose radius (m), dc is depth of cut (m) and y_c is the maximum crack length (m)

The maximum crack length (y_c) can be calculated according to the formula:

$$y_c \approx 120\frac{{K_C}^2}{H^2} \tag{3-9}$$

(Blake and Scattergood, 1990)

Where y_c is the critical crack length (m), K_c is the fracture toughness (J/m^2), and H is the material hardness

As such, table 4-3 was created showing the critical crack lengths for the different materials of interest, and graphs were also created showing the maximum feed rates associated with different depths of cut in polytypes of silicon carbide and in silicon. These limiting factors were used in the subsequent analysis.

It is noteworthy that there is a threshold load that is required for the cracks to be instigated, given by the formula:

$$P_L \approx 1.6\times10^4\frac{{K_C}^4}{H^3} \tag{3-10}$$

(Lawn and Marshall, 1979)

Where P_L is the load (N), K_c is the fracture toughness (J/m^2), H is the material hardness.

Accordingly, a table was created showing the loads required for sub-surface damage to be initiated in the materials, these limiting factors were used in the subsequent analysis- when the cutting force was calculated to reach these limiting forces, the DBT depth was taken as the depth of cut at which the cutting force was reached.

In order to more completely analyse the mechanical cutting process under different conditions, the procedure used by Arif et al's (2013) is applied to 4H-SiC to determine the critical depths of cut at which the ductile to brittle transition is predicted to take place under different cutting conditions. Arif et al (2013) used an energy based model in which they compared the predicted specific cutting energy required to remove material in a brittle way with that needed to remove material in a ductile way, the method requiring less energy being predicted to occur. This procedure is coupled with Blake and Scattergood's (1990) and Lawn and Marshall's (1979) formula for sub-surface damage, to predict whether the cutting will be brittle or ductile.

The cutting force can be predicted using the formulae below. This was done to compare the cutting forces with the calculated threshold cutting forces which would result in cracking.

$$F_c = \frac{H}{3\sqrt{3}} \frac{A_c}{\sin\varphi} \cos\varphi + \frac{H}{3} A_c + \mu_f \sigma_f A_f \tag{3-11}$$

(Arif et al, 2013)

Where F_c is cutting force (N), H is material hardness, Ac is the uncut chip area (m2), φ is the effective shear angle (°), μ_f is the friction coefficient at the flank, σ_f is the stress at the flank of the tool (Pa)

The following formulae were important in the above calculation

$$A_c \approx f \times dc \tag{3-12}$$

Where A_c is uncut chip area (m^2), f is feed rate (m/rev), dc is depth of cut (m)

$$A_f = W\left(r + w + \frac{2s}{3\tan\theta_f}\right) \qquad dc \geq r \tag{3-13}$$

$$A_f = W\left(\sqrt{r^2 - (r-dc)^2} + w + \frac{2s}{3\tan\theta_f}\right) \qquad dc < r$$

(Arif et al, 2013)

Where A_f is the area at the flank of the tool (m^2), W is the width of cut (m), s is the spring back (m), θ_f is the clearance angle (°), r is the tool edge radius (m), w is the length of flank wear (m)

The above formula from Arif et al (2013) has been modified in the case where the depth of cut is lesser than the tool edge radius. The reason for this is illustrated in figure 3-16. In the case where the depth of cut is less than the tool nose radius, the area at the flank of the tool does not encompass the entire edge radius, but only the fraction of it given by the formula above (ie the

distance D shown in the figure should not be included in the calculation). It is noteworthy however that area covered by the negative rake face is still not considered.

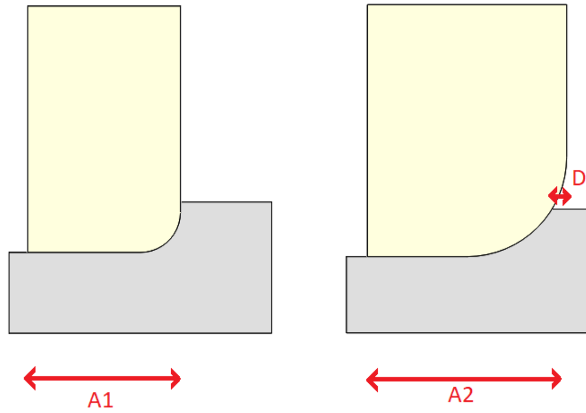

Figure 3-16 Modification to Flank Area Formula

$$\sigma_f = 3.5H\sqrt{\frac{H}{E}} \quad \textbf{(3-14)}$$

(Chunlei et al, 2016)

Where σ_f is the stress at the flank of the tool (Pa), H is the materials Vickers hardness, E is the Young's modulus (Pa)

The following formulae were used for calculation of the ductile-to-brittle transition depth according to Arif et al's (2013) framework. Chunlei et al's (2016) formulae were used to predict the spring back of the material which would normally be calculated experimentally, this being an adaptation to Arif et al's method:

$$\sigma_f = E\varepsilon \qquad \varepsilon \le \varepsilon_y$$

$$\sigma_f = \sigma_y \left(\frac{E\varepsilon}{\sigma_y}\right)^{nh} \varepsilon > \varepsilon_y \quad \textbf{(3-15)}$$

(Chunlei et al, 2016)

Where σ_f is the stress at the flank of the tool (Pa), E is the material Young's modulus (Pa), ε is the strain at the flank of the tool, σ_y is the yield stress (Pa), n_h is the strain hardening exponent

$$\varepsilon_y = \frac{\sigma_y}{E} \quad \textbf{(3-16)}$$

$$\varepsilon = \varepsilon_y + \varepsilon_p \quad \textbf{(3-17)}$$

(Chunlei et al, 2016)

Where ε_y is the yield strain, σ_y is the yield stress (Pa), E is the Young's modulus (Pa), ε_p is the plastic strain

$$s = (1 - \varepsilon_P) h_{\min} \tag{3-18}$$

$$h_{\min} = 0.35r \tag{3-19}$$

(Chunlei et al, 2016)

Where s is spring back (m), ε_p is plastic strain, h_{min} is the minimum undeformed chip thickness (m), r is the tool cutting edge radius (m)

$$\mu = \frac{\cos\varphi - \frac{\sin\varphi}{\sqrt{3}}}{\frac{\cos\varphi}{\sqrt{3}} + \sin\varphi} \tag{3-20}$$

$$\mu_f \approx 0.9\mu \tag{3-21}$$

(Arcona and Dow, 1998)

Where μ is the friction at the tool chip interface, μ_f is the friction at the flank of the tool, φ is the instantaneous shear angle

Additional formulae used are:

$$E_d = \frac{F_C}{A_C} \tag{3-22}$$

(Arif et al, 2013)

Where E_d is the specific ductile cutting energy (N/m^2), F_c is the cutting force (N), A_c is the cutting area (m^2)

$$\alpha_e = \sin^{-1}\left(\frac{t_0}{r} - 1\right) \qquad t_0 < r(1 - \sin\alpha) \tag{3-23}$$

$$\varphi_e = \tan^{-1}\left(\frac{r_c \cos\alpha_e}{1 - r_c \sin\alpha_e}\right) \tag{3-24}$$

(Arif et al, 2013)

Where α_e is the instantaneous rake angle (°), t_0 is the undeformed chip thickness (m), r is the tool edge radius (m), r_c is the cutting ratio, φ_e is the instantaneous shear angle

$$F_t = \mu[\frac{HA_c}{3}(\frac{\cot\varphi}{\sqrt{3}}+1)] + A_f(4.1H\sqrt{\frac{H}{E}}) \quad \textbf{(3-25)}$$

(Arcona and Dow, 1998)

Where F_t is thrust force (N), μ is the friction between the chip and the tool, H is the material hardness, A_c is the area between the tool and the chip (m^2), φ is the shear angle, A_f is the area at the flank, E is the material's Young's modulus (Pa)

$$C_m = (\frac{0.256P_L}{K_C})^{\frac{2}{3}} \quad \textbf{(3-26)}$$

$$C_l \cong \frac{C_m}{7} \quad \textbf{(3-27)}$$

(Arif et al, 2013)

Where C_m is the length of the median crack (m), C_l is the surface damage, $P_L$is the thrust force (N), K_c is the material's fracture toughness (N/m^2)

$$E_b = \frac{2((2\pi C_l + 2C_m)\gamma_s + \frac{HA_C}{3}(\frac{\cot\varphi_e}{\sqrt{3}}+1) + \mu_f 2\sqrt{t_0(2R-t_0)}(\frac{2s}{3\tan\theta_f})(3.5H\sqrt{\frac{H}{E}}))}{\pi C_l^{\ 2}} \quad \textbf{(3-28)}$$

Where E_b is the specific cutting energy required for brittle material removal, C_l is the surface damage, C_m is the length of the median crack (m), γ_s is the specific surface energy (J/m^2), H is the material hardness, A_c is the uncut chip area (m^2), φ_e is the instantaneous shear angle, μ_f is the friction at the flank, t_0 is the instantaneous chip thickness (m), R is the tool nose radius (m), s is the material spring back (m), E is the material's Young's modulus (Pa)

The values that were used for hardness, Young's modulus and depths of cut are as in table 3-9. The analysis was carried out for 4H-SiC only as this is the only material for which the strain hardening exponent is widely known. It is predicted that, 4H-SiC being one of the most difficult to machine materials, the results can form a worst-case prediction for results that would be obtained for the other materials of interest.

Table 3-9 Material Properties of 4H-SiC

Parameter	Value (4H-SiC)
Young's Modulus	330 GPa*
Hardness	26 GPa*
Fracture Toughness	1.9 MPa**
Strain Hardening Exponent	50***

*Shim et al (2008), **Chen et al (2000), ***Virkar and Patten (2013)

The methodology described above was used to determine the DBT depths of cut for several different cutting conditions evaluated, as shown in figure 4-19 which shows the critical DBT depth of cut for different feed rates; using this method it was possible to select the mechanical design. Parameters selected include rake angle, clearance angle and nose radius, while edge radius, feed rate and wear land were varied. It is noteworthy that where the cutting was predicted to become brittle according to Blake and Scattergood's (1990) model predicting sub-surface damage, then the depth of cut at which this occurred was taken as the DBT depth of cut.

The width of cut (W) is a distance across the nose radius, which is implied by the depth of cut with the formula below. It is important to note that the feed rate must not exceed the width of cut, this limitation was used in the analyses.

$$W = 2\times\sqrt{R^2-(R-dc)^2} \tag{3-2}$$

Where W is width of cut (m), R = nose radius (m), dc = depth of cut (m)

It is possible to calculate the best possible surface roughness achievable with a given feed rate and nose radius of tool with the equation below (Whitehouse, 1994). This was done to set a limit to the maximum feed rate which could be used for given tool nose radii, according to the surface roughness specified in section 3.1. The formula was rearranged to create the graph in figure 4-18 relating feed rate to surface roughness for several different nose radius tools (up to 13mm).

$$R_t \cong 0.032\frac{f^2}{R} \tag{3-3}$$

Where R_t is roughness total, f is feed rate (m/rev) and R is nose radius (m)

The analysis carried out in this section simulates several different cutting conditions and thereby works to determine the optimum cutting parameters and the effect that varying cutting

conditions has upon the DBT depth of cut. By carrying out this analysis, the background information is provided which allows for selection of the optimal machining parameters, and comparison with the analysis in the following section which investigates the effects of µ-LAM. The optimal machining parameters for the proposed tool are only presented in the next section, however, where the effect of µ-LAM is considered.

3.3.3 Assembly of Mechanical and Optical Design

In this section the effect that introducing laser heating by µ-LAM is considered, with an aim to predict the performance of the tool, and to evaluate the benefits which are gained through the use of laser.

In order to analytically investigate the use of laser, the same procedure is used as in the previous section, except that two parameters (material hardness and fracture toughness) are altered according to what is known to result from heating the material; as such figure 4-21 is produced showing the predicted DBT depth of cut for different feed rates. Shayan et al (2009) predicted that the effective hardness of the 4H-SiC in µ-LAM reduced from 26GPa to 13GPa, and Chen et al (2000) found that fracture toughness of silicon carbide dropped by approximately 30%when heated by 1275°C. Calculations on the predicted surface roughness are not repeated because they are not altered by the use of laser. 4H-SiC is again used as the material under consideration because of the availability of knowledge of its strain hardening exponent. As the optical design allows for heating closer to the melting temperature, the hardness may in fact be reduced further than indicated by Shayan et al (2009). The value of 13 GPa is used to indicate the minimum effect that µ-LAM is likely to have.

Figure 4-20 was created in this section using formula 3-8 in order to predict the depth of cut which is achievable for different nose radius of tool and feed rates, to avoid the propogation of sub-surface damage.

The effect of cutting parameters are presented with regards to machining of 4H-SiC. The results are compared with those without laser. The effect of µ-LAM having been considered, and the optimum parameters of the tool having been specified, it is necessary in the next section to identify limiting factors to the optical performance within which the configuration must be shown to operate to enable effective machining to take place.

3.3.4 Measures to Reduce Tool Wear and Thermal Shock

While proposing the use of laser to heat substrates in µ-LAM, it is important to evaluate the limitations in performance in this method, particularly when putting forward novel techniques such as the proposal involving the use of laser at different wavelengths.

Two different sets of limitations have been identified which are evaluated in this section: those concerning the increase in chemical wear of the tool due to heating by laser; and those concerning thermal shock of the substrate when subjected to sudden thermal heating.

With regards to increased chemical wear of the tool due to laser heating, Paul et al (1996) describe several formulae which are used to characterise the chemical wear rate of the diamond tool during SPDT, these are used to evaluate the increase in tool wear. The rate of chemical wear is then predicted for typical machining conditions, and these are evaluated to determine whether the laser heating is likely to cause excessive additional chemical wear. The formulae used are shown below:

$$k = A\exp(\frac{-E_a}{R_C T}) \quad \textbf{(3-4)}$$

(Paul et al, 1996)

This is the Arrhenius function, where k_r is the rate constant, A_e is the factor depending upon the entropy of the complex, E_a is the activation energy, R_c is the universal gas constant

It has been identified (Luo et al, 2012; Goel et al, 2012) that the primary mechanism of tool wear in SPDT of silicon carbide is graphitisation of the diamond tool because of high temperature induced by abrasion between the tool and workpiece. As such, the effect that the temperature increase caused by the use of laser is likely to have upon graphitisation is considered in this section. Luo et al (2012), using molecular dynamics simulation, detected temperatures in the surface of the diamond tool according to figure 3-17.

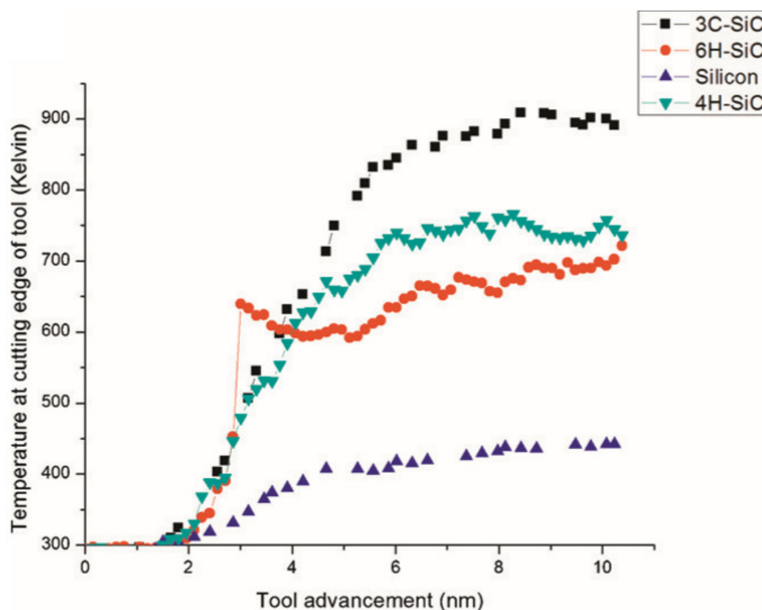

Figure 3-17 Temperature at Surface of Diamond Tool (Luo et al, 2012)

For this reason, the formula above was used to evaluate the effect of increasing the temperature at the tool from those shown in the figure above to the melting temperature of the material. Paul (1996) states how activation energies for graphitisation are either 730 kJ/mol or 1060 kJ/mol.

The diffusive wear rate in silicon was also considered:

$$r_D = k_D \frac{(c_0 - c)}{\lambda_D} \qquad \textbf{(3-5)}$$

$$k_D = A_D \exp(\frac{-E_D}{R_C T}) \qquad \textbf{(3-6)}$$

(Paul et al, 1996)

Where r_D is the rate of diffusive wear, k_D is the diffusive rate constant, c_0 is the saturation concentration, c is the concentration of carbon atoms in the metal, λ_D is the distance between sites, A_D is the pre-exponential factor for diffusion, E_D is the activation energy for diffusion, R_C is the universal gas constant and T is the temperature

The above formula is used with the parameters in table 3-10 to carry out calculations of the increase in diffusion for silicon (shown in figure 4-19 which predicts the increase in diffusion at higher temperatures):

Table 3-10 Parameters Used in Diffusive Wear Calculation

Parameter	Value
Activation Energy for Diffusive Wear	280 kJ/mol (Silicon) [Paul (1996)]
Gas Connstant	8.314 J/K mol

With respect to the control of thermal shock, Hasselman (1986) presents an overview of the resistance of ceramics to thermal stress, the formulae which he discusses is used in the analysis:

$$\Delta T_{\max} = \frac{\sigma_c (1 - v)}{\alpha E} \qquad \Delta T > 0 \qquad \textbf{(3-7)}$$

Where ΔT_{max} is the maximum temperature change, σ_c is the compressive yield stress, v is the Poisson's ratio, α_t is the coefficient of thermal expansion, E is the Young's modulus

3.4 Preliminary Analysis of Tetraform C

3.4.1 Design Considerations for the Tool

An outcome of the project was the design for the implementation of the µ-LAM system for a machine in Cranfield's ultra precision laboratories. This design task was undertaken, and can be divided into different sections as in figure 3-18 according to the type of design that was being implemented. The first stage was to determine the optical components for the tool, including components like the laser, fibre optics and lens configuration. The next stage was to design the cutting tool which was going to be used in conjunction with the optical setup. The final stage involved determining the effective implementation of the tool upon an ultra-precision machine in Cranfield's UP Laboratory.

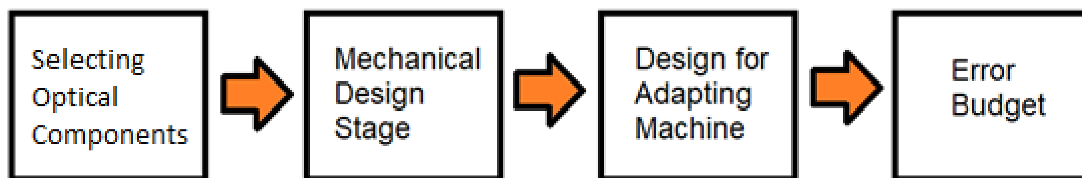

Figure 3-18 Design Process

A description is given of several different concepts which were considered in the optical design, which are shown in figure 3-19. These different concepts are presented and evaluated, and the rationale behind their adoption or otherwise is given.

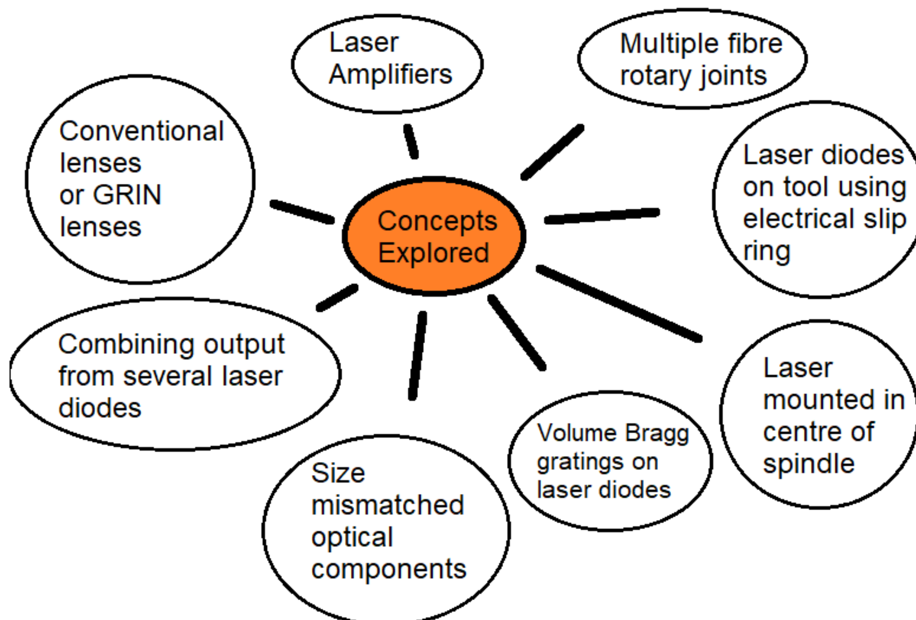

Figure 3-19 Optical Design Concepts Considered

In terms of the design for the fixture which secures the cutting tool to the spindle, several different options were again considered- the rationale behind their adoption or otherwise being given in the results section. The final design which was created is also presented, along with the design for the brackets which fix the spindle to the frame of the Tetraform C. The different options which were considered are shown in figure 3-20.

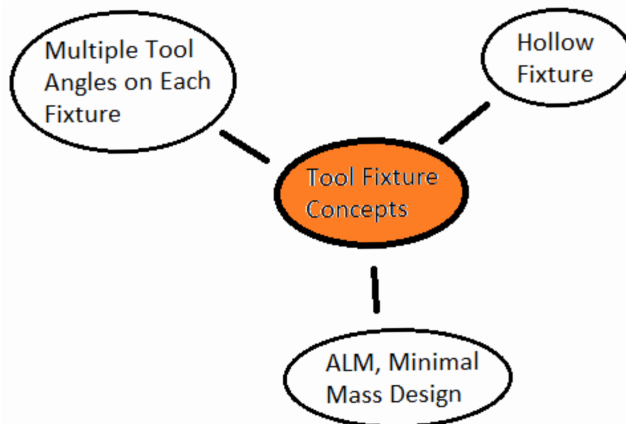

Figure 3-20 Tool Fixture Concepts Considered

A problem was encountered in the design for the assembly of the optical components with the diamond cutting tool. Unlike in conventional µ-LAM, in the tool proposed the optical components are not stationary, and are rotating at high speeds and will undergo forces associated with acceleration of the tool. Because of this, it was determined to be unlikely to be practical to use the more traditional configuration of lenses for delivering the laser beam to the diamonds, because these lens configurations are normally designed to remain stationary, and their motion is likely to induce deflection which can cause the beam to change its position. As it is necessary for the beam to remain focused exactly at the cutting location where the substrate undergoes high pressure phase transformation, it was necessary to find an alternative configuration of optical equipment which would perform the optical functions required while remaining mechanically robust at high speeds. As it is quite unusual to employ high power optics that are moving at such high speeds, there was no commercially available optical setup that was designed specifically for this problem. Therefore, a custom solution is proposed which could be used.

In order to implement the tool on the Tetraform C machine, it was necessary to design several modifications to the machine. There were several different concepts for the modified machine which could have been used, and it was first necessary to select the concept which would be carried forward in the design. The rationale used was to minimise the changes to be made. This was done because it not only implied that the cost for the conversion would be kept to a minimum, but also that its complexity would be reduced- both minimising the difficulty of the conversion, and the likelihood that it would not function as expected. The rationale behind the

adoption or otherwise of the different concepts shown in figure 3-21 which were considered is discussed.

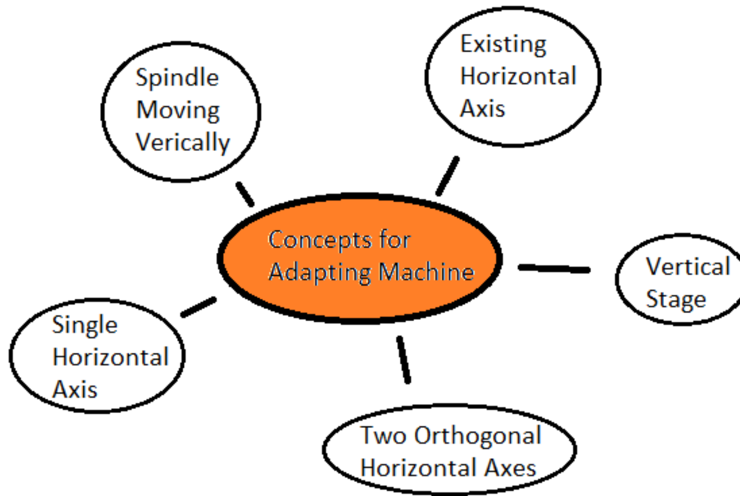

Figure 3-21 Concepts for Modifying Tetraform C

A priority was placed upon maximising the accuracy in the Z direction, because this ultimately determines how shallow the depths of cut are that can be taken, and therefore which materials can be machined in the ductile regime, as shown in table 2-4. The error budget carried out in section 4.3 contains FEA results evaluating the machine's performance in this respect.

Once the concept had been selected, calculations were carried out to determine parameters in selecting components, relating to the specification in section 3.1.

Material removal rate (MRR) is a characteristic of SPDT which as expected defines how quickly material is cut away from the workpiece. Naturally, high MRR is desirable as it implies that processing speeds are faster. The formula for this is:

$$MRR = s \times dc \times V_c \quad \textbf{(3-8)}$$

MRR is Material Removal Rate (m^3/s), V_c is cutting speed (m/s), dc is depth of cut (m), f is feed rate (m/rev)

With regards to cutting speeds, with reference to the MRR specified (table 3-1), the formula for MRR was rearranged to give cutting speed in terms of the other parameters as below:

$$Vc = \frac{MRR}{dc \times s} \quad \textbf{(3-9)}$$

Where MRR is material removal rate (m^3/s), d_c is the depth of cut (m), f is the feed rate (m/rev), V_c is the cutting speed (m/s)

As the feed rates had already been calculated, these were substituted into the above formula to determine the relationship that would exist between cutting speed, MRR and depth of cut, which is shown in figure 4-38. As it is known that there are several depths of cut (see table 2-4) which are of interest, cases were taken at these depths of cut. A plot was created using each of these depths of cut, relating cutting speed to MRR. The plots were then analysed in conjunction in terms of the material removal which is expected for each depth of cut to determine a cutting speed which satisfies the MRR requirements generally. The speed of the spindle is limited by the maximum turning capability of the fibre optic rotary joint, as beyond a specified speed this component would not necessarily function as expected.

With regard to torque requirements, the cutting force which is caused by the tool removing material from the substrate, as calculated in section 4.1.2, was used to determine this, according to the formula:

$$\tau = R_s \times F_c$$

(3-10)

Where τ is the torque (Nm), R_s is the swing radius (m), and F_c is the cutting force (N)

The toque of the configuration was calculated and compared with the cutting forces indicated previously in section 4.1.3. Using these calculations it was possible to select the spindle of the machine.

3.4.2 Experimental Modal Analysis

Fu and He (2001) have defined modal analysis as 'the process of determining the inherent dynamic characteristics of a system in forms of natural frequencies, damping factors and mode shapes'. Modes are vibrational excitations of objects which are associated with frequencies, shapes, damping, and scales. Modes can be determined using FEA, or experimentally as in this investigation. Determining what modes are associated with a machine is useful as this can indicate frequencies that should not be excited in the machine. This was done in the current study because it indicates spindle speeds which should not be used in the installation of the system upon Cranfield University's Tetraform C machine, thereby allowing for a more complete design for implementation of the tool.

Accelerometers were attached to the Tetraform C using a wax layer. A hammer with built in force transducer was used to provide the impact that would cause the machine to vibrate. These were connected to a signal acquisition and processing unit. The signal acquisition and processing unit was attached to a computer running LMS Test Lab software, which was used to produce images of the motion of the machine under various modes, and to show their frequency and damping.

The experimentation was carried out with weveral trials, such that each member of the Tetraform C's frame, and each connecting ball was tested with 4 accelerometers, with 3 strikes in each direction, using each of 3 hammers (low, medium and high frequency) leading to a total of 81 tests. Figure 3-22 shows all of the accelerometer locations used.

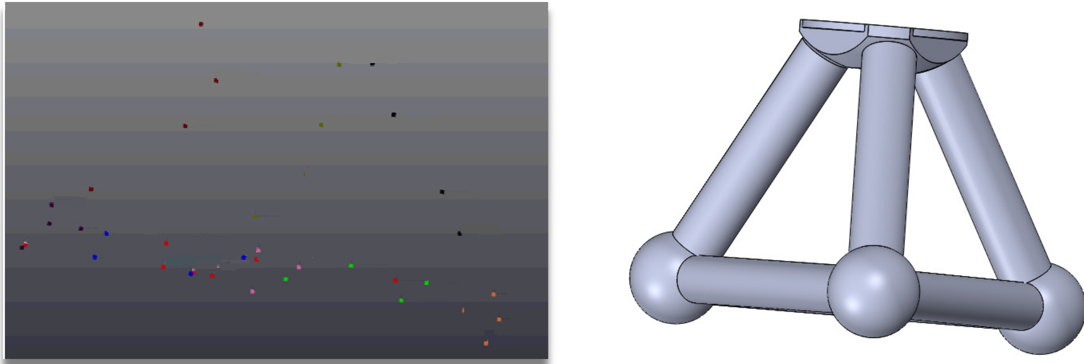

Figure 3-22 Nodes Used in Modal Analysis (Orientation of Machine Shown)

As a surplus of modes were identified in the experimentation, to ensure that the modes being identified were representative of modes of the machine, the modes considered were narrowed down using a method which is illustrated in figure 3-23. The same three contact points were used throughout the analysis.

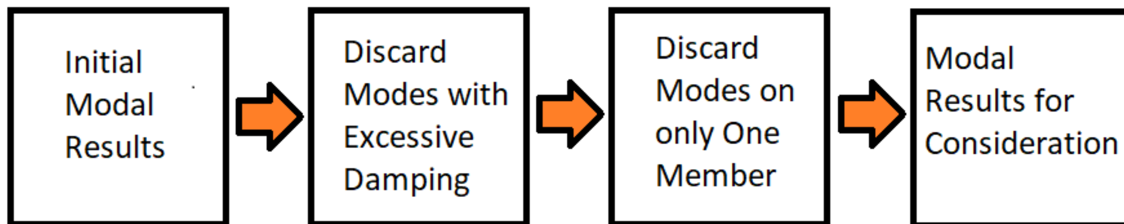

Figure 3-23 Filtering of Modal Results

First, as modes with excessively high damping are known to be caused by factors other than the vibration of the frame (for example by the vibration of the machine's axes), these modes were discarded in the current investigation.

In order to be certain that the modes detected were accurate, it was decided that if the same mode was detected when different members of the machine were being tested, it would be included. One mode which was identified by this method was ignored because it was only detected twice, which may have been a coincidence.

Arai (2004) carried out a similar modal analysis on the Tetraform C machine, although he conducted this when the machine was loaded with more components. Arai did not discuss all of the modes that he identified, but his results are compared with those found in the current study. The mode frequencies identified are also compared with likely sources of vibration in the

Tetraform C with the proposed modifications. The modes identified are displayed graphically in figure 4-41 which shows the mode frequency against the damping percentage.

3.4.3 Laser Heating Experiments on Silicon Wafer

Ravindra put forward a formula to attempt to describe the relationship between cutting speed and the amount of power that is transferred to the material, but this formula indicated that at speeds around 1m/s, no significant effective heating could be expected using laser powers commonly available.

Because of this it was decided to test this experimentally to determine whether the heating caused by a laser operating at similar speeds would have a thermal effect upon a silicon substrate. Ravindra (2011) had carried out experiments in which he recorded the temperature which silicon substrates reached for effective μ-LAM to take place, finding that >1038°C was the effective temperature needed for μ-LAM to take place, so this temperature was aimed at in the experimentation. The experimental setup was as in figure 3-24.

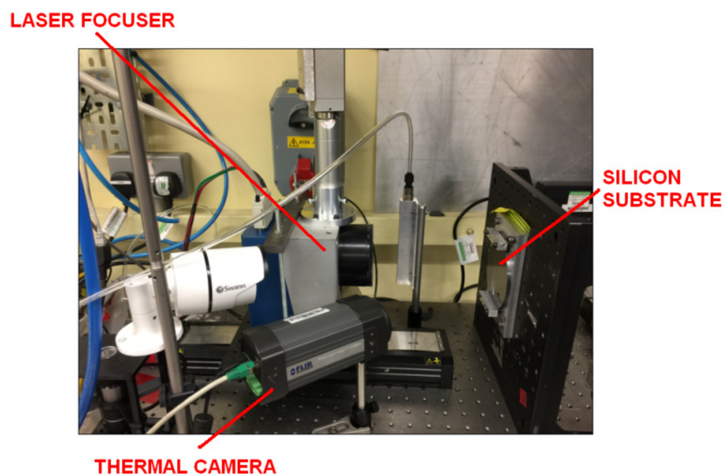

Figure 3-24 Experimental Setup for Laser Testing

The substrate, a 10mm thick silicon disk, was mounted on a stand, facing a laser. The laser was used in CW mode, having a maximum possible power of 100W at 1μm wavelength. A thermal camera was positioned such that it pointed at the silicon substrate to view its entire surface. The thermal camera was used which captured temperature at a frequency of 660Hz. The laser operates with software which allows its distance from the substrate, speed of travel and power to be adjusted.

The equipment was programmed to run the laser across the silicon substrate in a raster pattern, filling a small square. The speed of the laser and its power were altered until significant heating was viewed in the thermal camera. The experimentation was carried out with a view to

determining whether effective heating was likely to take place with the laser powers and speeds concerned.

3.5 Error and Uncertainty Budget

An error budget (Uriarte et al., 2007a) is a tool used by designers of ultra-precision machines in order to predict the errors that are likely to occur in their machine. Error budgets normally identify components of errors acting in the X, Y and Z directions, and categorise them as occurring because of different sources, eg: thermal expansion, tilt errors, vibration etc..

An error budget is presented to predict the accuracy of the adapted Tetraform C machine in the Z direction, this being the direction which is most important in determining how shallow the depths of cut are that can be taken for enabling ductile mode machining of brittle materials. While accuracies in the X and Y directions are important, it is not foreseen that these will limit the implementation of the tool upon the machine, so these are omitted from the investigation.

An important aspect considered in carrying out the design analysis was the machining loop of the Tetraform C (Shore, 1995). While deflections, stresses and vibrations are important in any part of the machine, the machining loop is particularly important as it consists of the parts which act to connect the tool to the workpiece, as shown in figure 3-25. Because of this, it was decided to analyse each of the components in the machine loop for the proposed modification to the Tetraform C machine in terms of their stiffness in the Z direction. FEA was carried out on the configuration designed, shown in figure 3-26 (along with numerical analysis) to ensure that its accuracy was likely to lie within the required range.

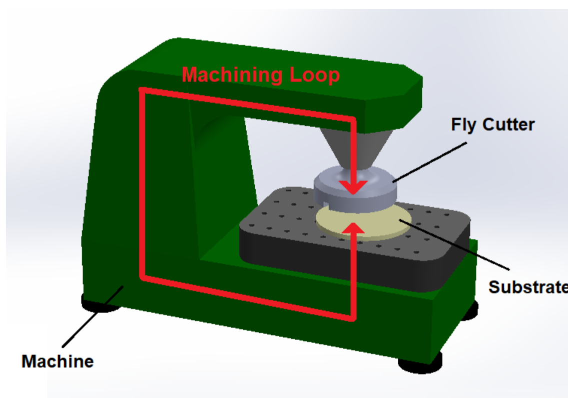

Figure 3-25 Machining Loop

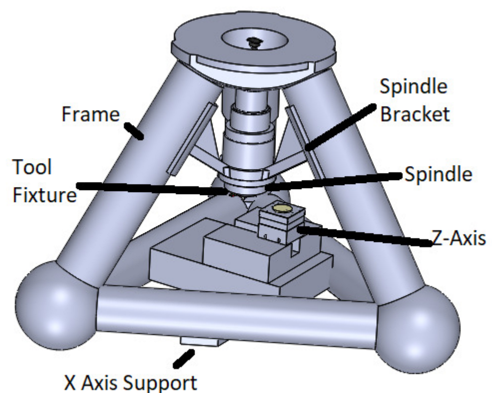

Figure 3-26 Tetraform C Machining Loop

An important consideration is that depending upon the cutting parameters employed and the material being cut, different thrust forces are predicted to be caused by the process. So that the error budget is representative of several different cutting conditions, four such conditions are considered in the analysis (shown in table 3-11).

Table 3-11 Cutting Conditions Considered in Error Budget

Material	Depth of Cut (nm)	Thrust Force (N)
Silicon	260	2.2
Silicon	100	0.26
Silicon Carbide	117.5	1.1
Silicon Carbide	60	0.57

The errors are assessed in terms of magnitude (ie maximum displacement in nanometres likely to occur) under each cutting condition. The magnitudes are determined either according to information given by suppliers, or by FEA where appropriateusing the Nastran FEA software package. Parabolic elements were used in the FEA process, and the mesh was progressively refined until the results converged.

The Z axis table, shown in figure 3-27, is a component supplied with known accuracies, and these accuracies are inputted into the error budget. It is noteworthy that the inaccuracies of this component are likely to be non-repeatable errors, so will be among the more important factors in the error budget.

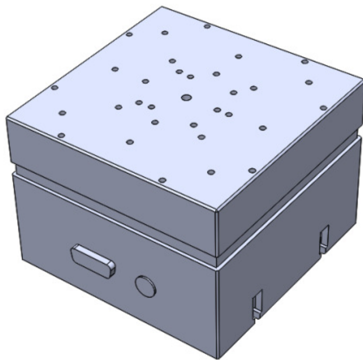

Figure 3-27 Z Axis Table

FEA was carried out on the X axis support, shown in figures 3-28 and 3-38. The boundary conditions were as in the figure below, with the position of the screws which secure the component to the frame made fixed, and the thrust force applied uniformly across the upper surface of the part. 50266 parabolic elements were ultimately used in the analysis, with stainless steel 304 used as the material.

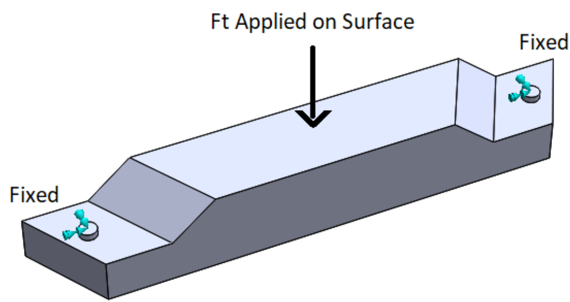

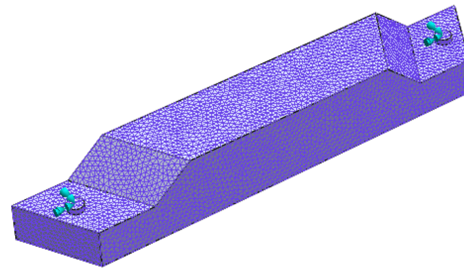

Figure 3-28 X Axis Support Free Body **Figure 3-29 Meshed X Axis Support**

With regards to the analysis of the frame (shown in figure 3-30), the claimed stiffness of the Tetraform C machine is 100 N/µm (Arai, 2004), which equates to a deflection of 10nm for 1N of load. The claimed stiffness of the machine as a whole was used as the stiffness of the frame, to predict the deflection caused by the forces induced in cutting.

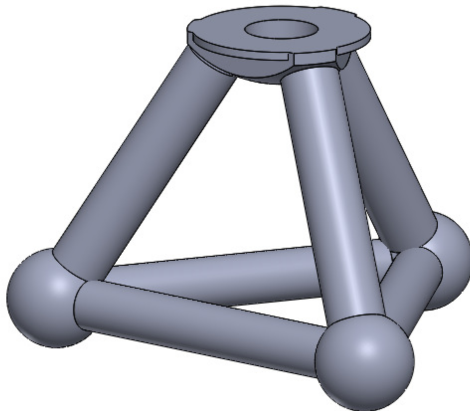

Figure 3-30 Tetraform C Frame

The spindle supports, shown in figures 3-31 and 3-32, were constrained with loads applied as in the free body diagram below, with a third of the thrust force (because there are 3 supports) applied along the lower face where the spindle is attached, and the two faces which are attached to the frame made fixed in the analysis. 127413 parabolic elements were ultimately used for the analysis, with the material being stainless steel 304.

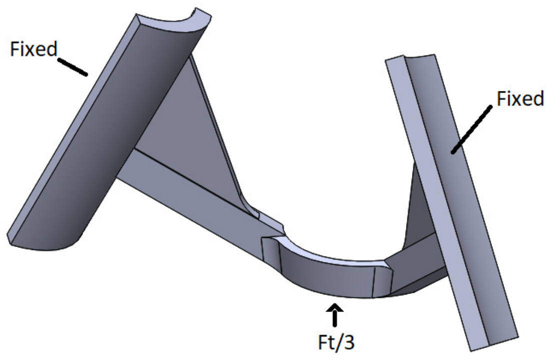

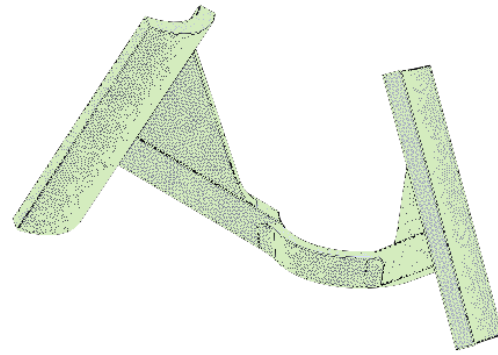

Figure 3-31 Spindle Support Free Body **Figure 3-32 Meshed Spindle Support**

The radial and axial errors in the spindle, shown in figure 3-33, are an inherent property of the spindle as it is provided by the supplier, and therefore cannot be altered for the purposes of the installation- the figure below illustrates the direction of these errors, as well as that of the tilt errors. The errors involved with the tilt motion are also affected by the length of the spindle, because they are calculated based upon the maximum tilt angles multiplied by the distance at which they are acting. The height of the tool fixture is also considered in this calculation.

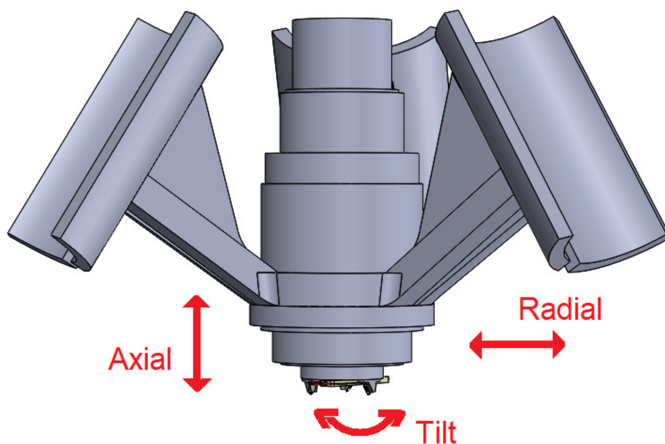

Figure 3-33 Spindle Errors

With regards to the deflection in the tool fixture, shown in figures 3-34 and 3-35, this was again calculated using an FE analysis. As shown in the figure below, the base of the tool was made fixed, and the thrust force was applied as a point load at the tip of the diamond. Meshing of different density was used as shown in the figure below, with 25116 parabolic elements used in the diamond tip, 10844 used in the tool shank, and 25116 used in the tool fixture. Diamond was used as the material for the tool tip, and stainless steel 304 used for the tool shank and fixture. The three components were made to have rigid connections to each other. Results were only taken from the FEA analysis in all cases when they were found to be converged upon by refining of the mesh.

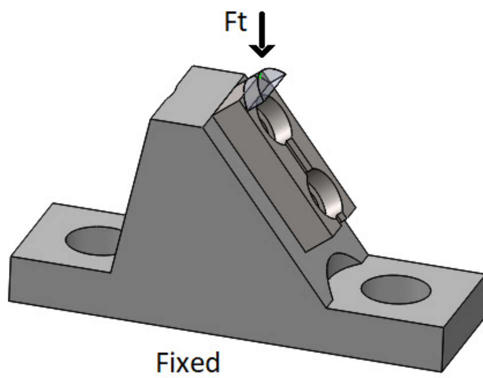

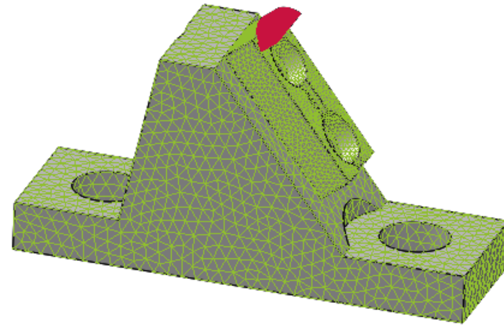

Figure 3-34 Tool Fixture Free Body Diagram **Figure 3-35 Tool Fixture Meshed**

Having carried out the analysis to predict the deflections in the components, an error budget summing the errors caused by the different components is presented, and the results are compared to the accuracies which are required to enable ductile machining of the materials of interest, as calculated in sections 4.1.2 and 4.1.3.

4 ANALYSIS AND DISCUSSION OF THE RESULTS

4.1 Design Process

4.1.1 Determination of Optical Parameters

The procedure outlined in section 3.3.4 was followed to obtain graphs showing absorption and depth of absorption for amorphous silicon, shown in figure 4-1 and 4-2.

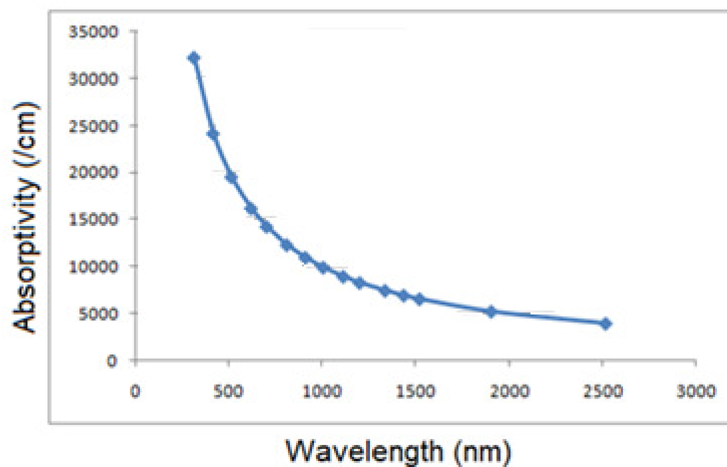

Figure 4-1 Absorptivity of α-Si (Palik, 1998a)

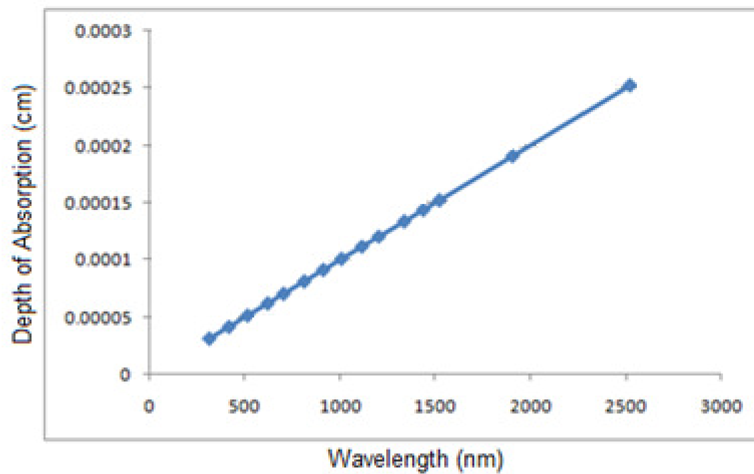

Figure 4-2 Depth of Absorption for α-Si (Palik, 1998a)

It can be seen that at 1000nm, light is absorbed to approximately 1 µm depth in amorphous silicon, which corresponds well to depths of cut of approximately 0.2 µm, as identified by (Ravindra, 2011) when machining with the use of laser. Formula 3-3 is used to determine the losses in intensity at various depths below the surface of amorphous silicon at 1000nm wavelength light, the results are shown in the figure 4-3.

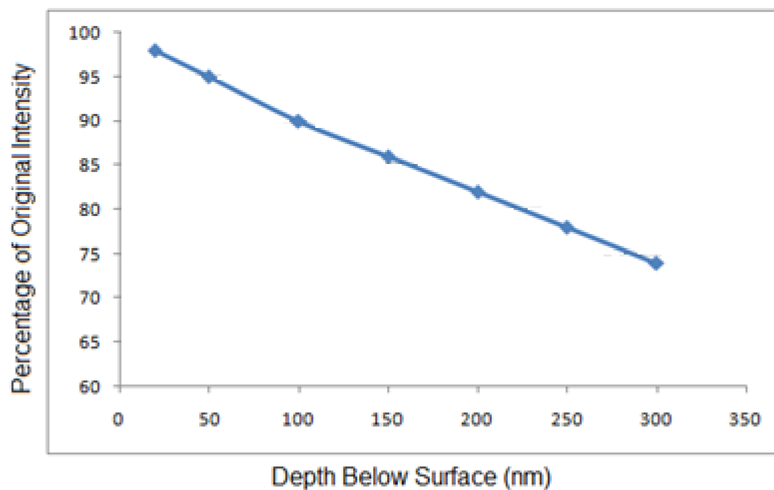

Figure 4-3 Loss of Intensity α-Si

The plot shows a linear decrease in intensity as depth below the surface increases, and that losses in intensity are not significant at lower depths (eg 20nm), but that by larger depths of cut under consideration (eg 260nm), that losses are significant, although not necessarily excessive to the extent that significant heating would be prevented.

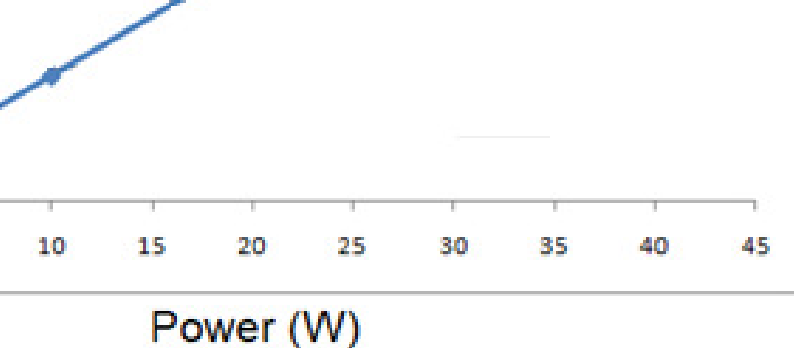

Temperatures of Heated Silicon

at the optimal power level predicted is around 40W. The results indicate that ents should be able to provide at least this amount of power at the diamond y that it is likely, because of the temperature dependent changes in ials, that only a lesser laser power will be required.

ond optical design, as the melting temperature of silicon is 1414°C, it was his temperature no further heating should occur, as melting of the material is at the benefits of µ-LAM are increased while approaching the melting s 4-5 to 4-8 show lines of best fit for Green's (2008) data for the refractive nction coefficient (k) of silicon, and the rate of change of these with the wavelengths of interest (where the indices decrease with increasing

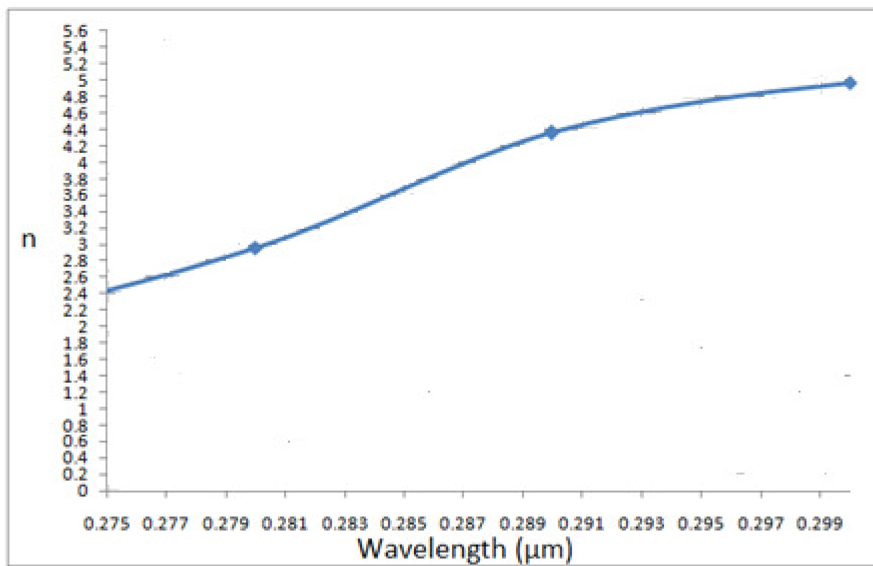

Figure 4-5 n values of pristine silicon

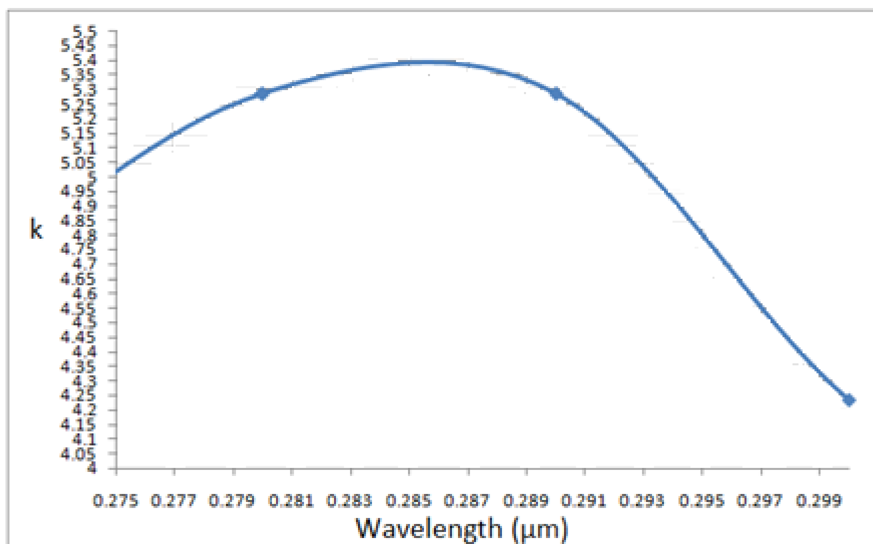

Figure 4-6 k values of pristine silicon

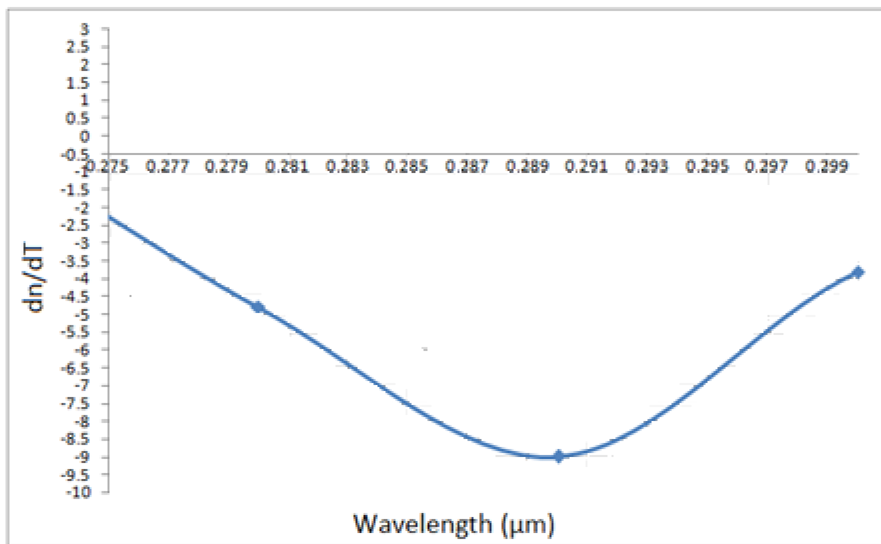

Figure 4-7 dn/dT values of pristine silicon

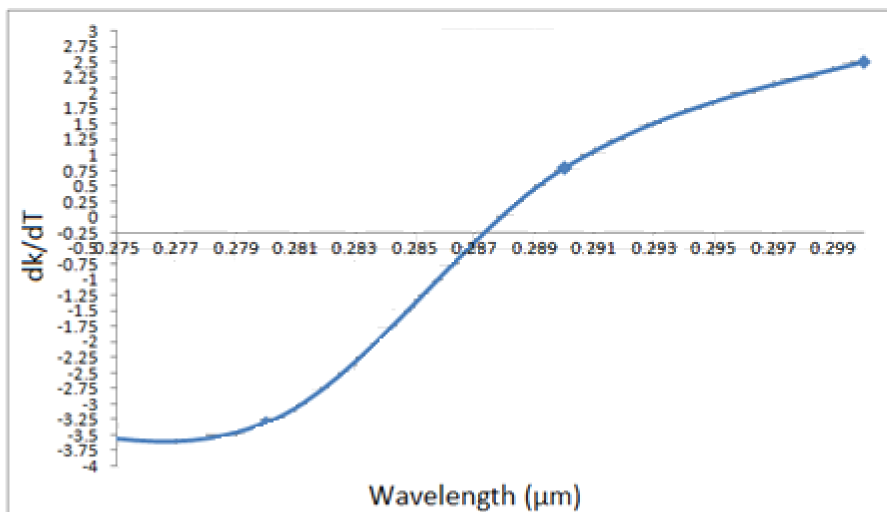

Figure 4-8 dk/dT values of pristine silicon

Formula 3-6 was used to predict the temperature at which the refractive index of silicon reduces to zero for different wavelengths in the range of interest shown above. It can be shown that for a wavelength of 294nm, the refractive index reduces to zero just before the material reaches 1410°C. It is estimated therefore, that by using light of this wavelength at a high enough power, that the temperature of the material will closely approach but not exceed the melting temperature.

It is also necessary to consider the depth of absorption of the material at the given wavelength, in order to ensure that light is being absorbed to a significant depth in the material. Depth of absorption is given by the formula:

$$l = \frac{\lambda}{4\pi nk} \tag{4-1}$$

Where λ is the wavelength of the laser used (m), n is the refractive index of the material at that wavelength, and k is the imaginary component of the complex refractive index at that wavelength

In the case of light at 294nm in silicon, the absorption depth can be calculated to be only about 1.2nm at 300K, but can be predicted to increase to over 200nm by the time the material heats to 1350°C (the material being expected to exceed this temperature). In order to verify that heating is occurring at a sufficient depth, the heat transfer formulae shown below are used:

$$Q = \frac{kA(T_{HOT} - T_{COLD})t}{d} \quad \textbf{(4-2)}$$

$$Q = m \times C_P \times T \quad \textbf{(4-3)}$$

Where Q is heat transfer, k is thermal conductivity, C_p is thermal conductivity, T_{HOT} is the hotter temperature, T_{COLD} is the colder temperature, t is time, and d is distance between the two temperature points, T is temperature. The formula is used with the parameters in table 4-1.

Table 4-1 Parameters Used to Verify Depth of Heating

Parameter	Value
K	120 W/m.K
C_P	750 J/Kg.K
A	2 x 10^{-12} m^2
T_{HOT}	1410 °C
T_{COLD}	20 °C
D	100 nm
T	0.56 µs
T	1400 °C

It was found using the above parameters, that within the dwell time of the laser, it is possible to heat a volume corresponding to a cube with sides over 7 µm long to 1400 °C (which compares well with feed rates being machined).

As discussed previously, the heating of the material actually slows down at this wavelength as its temperature increases. As this is the case, the laser dwell time is considered incrementally, in steps to account for the decreasing heating. The results are shown in figure 4-9.

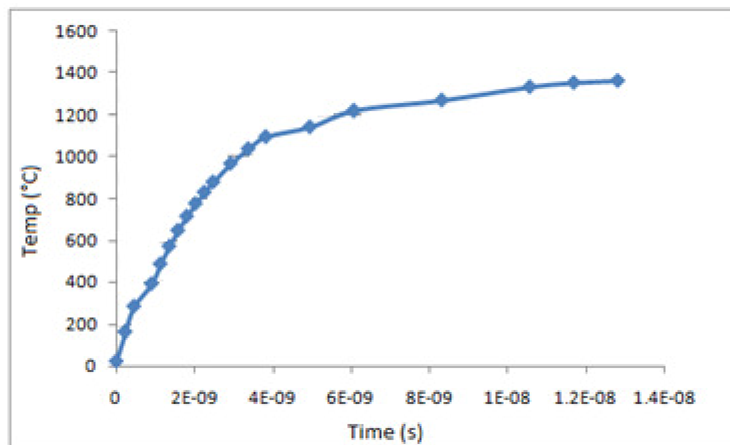

Figure 4-9 Temperature Increase in Pristine Silicon

The graph shows the heating expected caused by a 1W laser at 294nm on silicon. It can be seen that by 14ns, that the maximum temperature of about 1375°C is reached, and that no further heating occurs at this temperature, as the absorptivity has reduced to zero. It is noteworthy also, that the time to reach this temperature is significantly less than the minimum dwell time of the laser upon the material, indicating that the material could be kept at a constant temperature of 1375°C regardless of the cutting speed.

In this section two optical designs are presented for the machine tool, the first using light at 1000nm wavelength and 40W at each diamond, and the second using light at 294nm with a power of up to 1W. It is demonstrated how the second optical design is capable of more closely approaching the melting temperature of the material, and delivering enhanced effects of µ-LAM. It is also shown that this design is capable of heating the substrate within the time that it is exposed to the laser when cutting occurs at maximum speed.

Some limitations to the design presented include that it is carried out with consideration of pristine silicon, whereas in SPDT the phase of silicon present in the cutting region is amorphous silicon carbide, for which absorptivity is affected differently by changing temperature. While data about the way that amorphous silicon (and indeed silicon carbide) changes in absorptivity with increasing temperature is not widely available, Green (2008) presents a methodology of creating such data from results of other experimentation- of which there are several sources for both amorphous silicon and silicon carbide. It is however evident that there is scope for altering the wavelength of laser light used with significant effect, and that it is possible to do so to address the issue of the relationship between laser power and cutting speed which will influence the effectiveness of µ-LAM.

4.1.2 Determination of Cutting Parameters

In this section the preliminary mechanical design of the tool is carried out. Using Bifano's (1991) formula, table 4-2 was created as a preliminary indication of the critical depths of cut for several

materials of interest. Ravindra's (2011) experimentally determined depths of cut for the DBT transition are also shown for comparison:

Table 4-2 Critical Depths of Cut

Material	Young's Modulus (GPa)	Fracture Toughness (MPa $m^{1/2}$)	Hardness (GPa)	Calculated Critical Depth of Cut (nm)	Ravindra's (2011) Obtained Critical Depth of Cut (nm)	Mean Critical Depth of Cut (nm)
3C-SiC	314.55	2.02	26.4	10.5	42.5	26.5
4H-SiC	347.01	1.9	25.5	11.3	20.0	15.65
6H-SiC	347.01	1.9	19.2	26.5	17.5	22
Silicon	135.24	0.9	9.1	21.8	185.0	103.4

An important consideration when determining mechanical cutting parameters is that the feed rate is limited by the critical crack length which will cause sub-surface damage, as shown in figure 2-7.The critical crack lengths for the materials of interest are shown in table 4-3.

Table 4-3 Critical Crack Lengths (Goel, 2014)

Material	Fracture Toughness (MPa $m^{1/2}$)	Hardness (GPa)	Critical Crack Length (µm)
3C-SiC	2.02	26.4	0.7025
4H-SiC	1.9	25.5	0.6667
6H-SiC	1.9	19.2	1.1751
Silicon	0.9	9.1	1.1737

From this information, it is possible to calculate the maximum feed rates which can be applied with tools of different nose radius. This has been done for each of the materials of interest, and is shown graphically in figures 4-10 to 4-13.

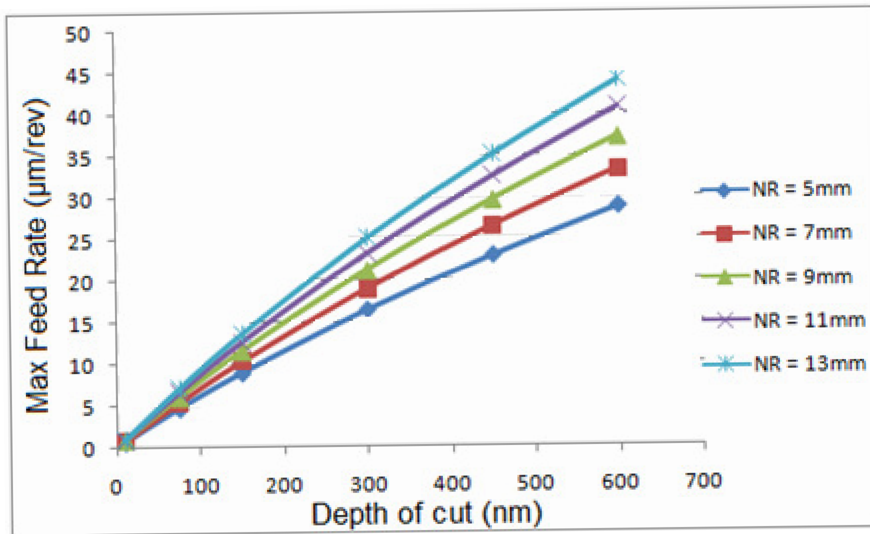

Figure 4-10 Maximum Feed Rate for Different Depths of Cut in 3C-SiC

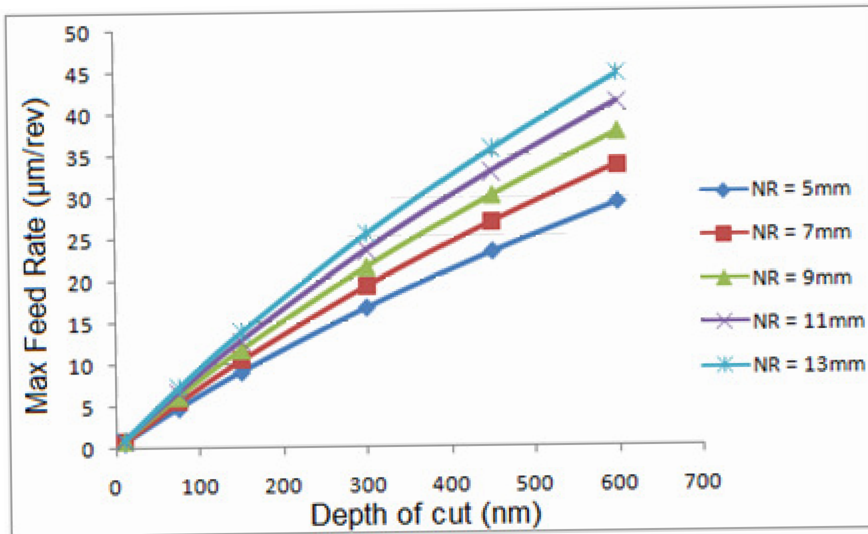

Figure 4-11 Maximum Feed Rate for Different Depths of Cut in 4H-SiC

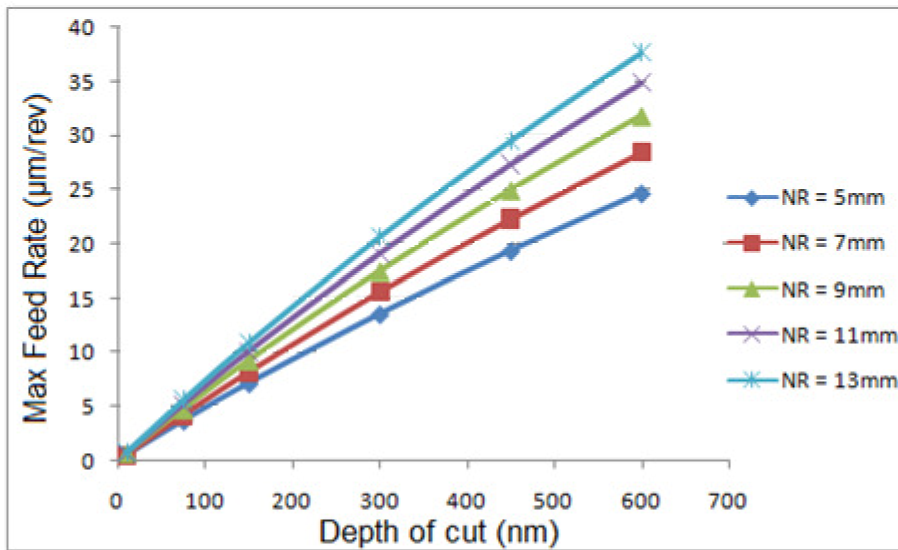

Figure 4-12 Maximum Feed Rate for Different Depths of Cut in 6H-SiC

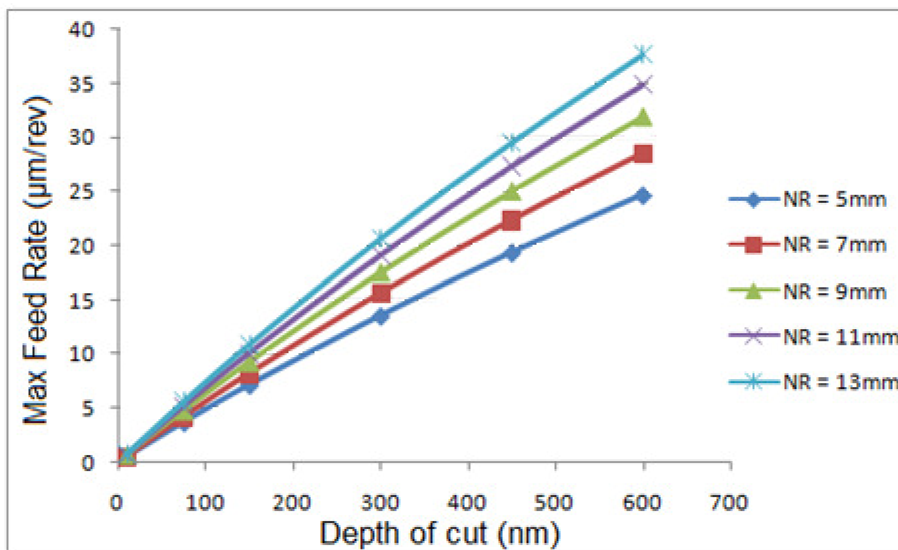

Figure 4-13 Maximum Feed Rate for Different Depths of Cut in Silicon

It can be seen from the above graphs that, at the depths of cut of interest, it is not possible to exceed feed rates of about 2.5 µm/rev. As later in the study it is determined that the minimum feed rate is approximately 25 µm/rev when using laser due to the laser spot size caused by the optical components selected, it is indicated that the maximum feed rate of 2.5 µm/rev is not likely to be sufficient in the case where µ-LAM is used. In the case presently under consideration, however, where laser is not being used, it may be possible to reduce feed rates sufficiently. It is also possible to determine the threshold cutting forces below which cracking for sub-surface damage will not occur, this is shown in table 4-4. Using cutting forces which are below this level will not induce cracking, so allows for greater feed rates to be employed.

Table 4-4 Critical Loads (Goel, 2014)

Material	Fracture Toughness (MPa $m^{1/2}$)	Hardness (GPa)	Critical Load (N)
3C-SiC	2.02	26.4	0.014
4H-SiC	1.9	25.5	0.013
6H-SiC	1.9	19.2	0.029
Silicon	0.9	9.1	0.014

A parameter of interest is the surface roughness which is likely to be achievable for a given nose radius of tool and feed rate. The surface roughness required was defined in section 3.1, and so the graph in figure 4-14 can be used to indicate the feed rate limitations imposed for different nose radius of tool. These results will apply both to heating with and without laser:

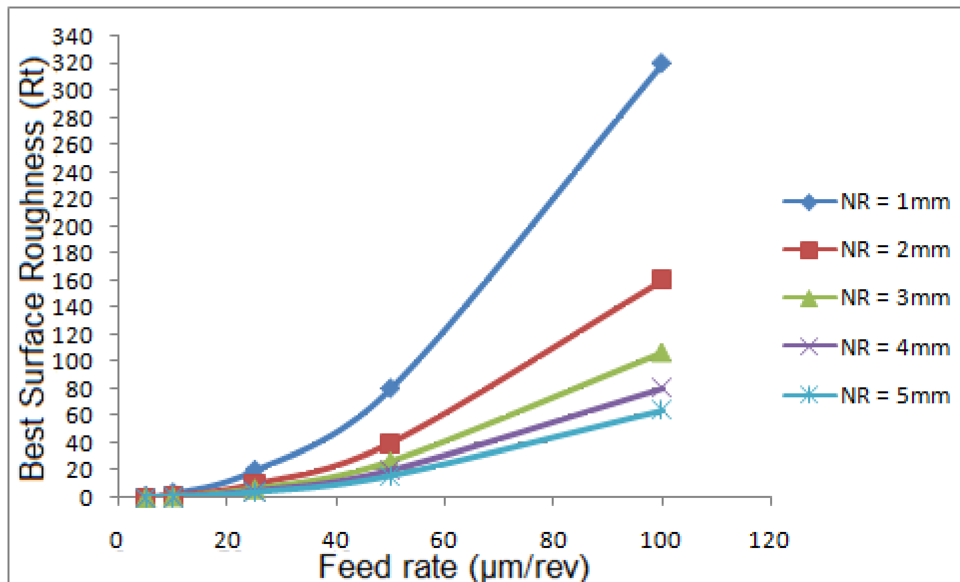

Figure 4-14 Feed Rate correlated to Surface Roughness

It can be seen that even with a 1mm nose radius tool feed rates of up to about 50µm/rev are possible before exceeding a surface roughness of 80nm R_t (as specified in section 3.1). The nose radius, therefore, does not seem to be significantly limited by the surface roughness required.

The procedure outlined in section 3.3.2 has been used to determine the ductile to brittle transitions depths of cut for 4H silicon carbide for various different cutting parameters. High clearance and negative rake angles were seen to improve DBT depths, so these were specified as -45° and 35°. The graph in figure 4-15 shows the predicted DBT depths for different nose radius of tools, for different feed rates:

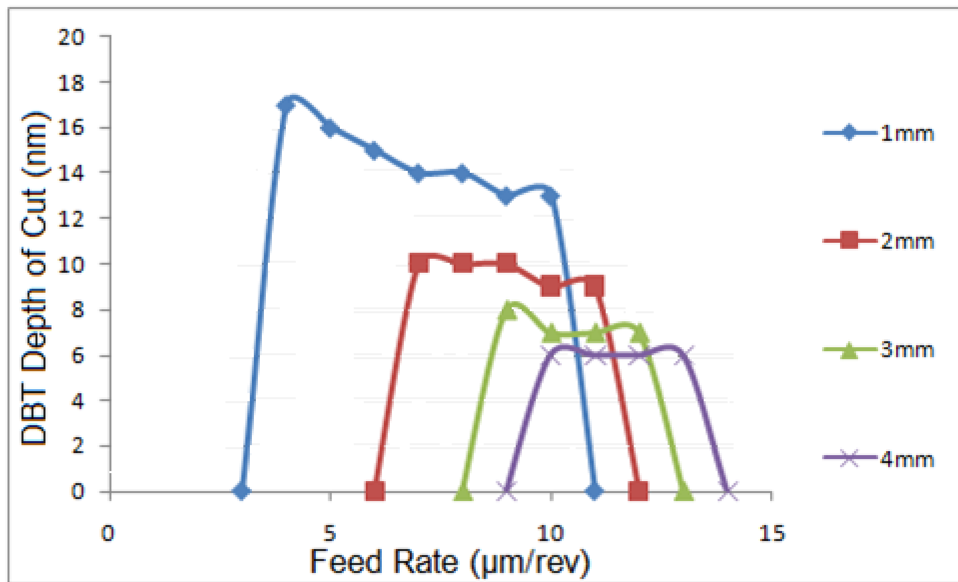

Figure 4-15 Feed Rate correlated to DBT Depth

It can be seen that a maximum DBT depth of cut of 17 nm is predicted using a 1mm nose radius tool at a feed rate of 4 µm/rev, and that in this mode of material removal (limited by the cutting force threshold at which sub-surface damage is induced) increasing the nose radius has the effect of decreasing the DBT depth. It is important to note that there are cut-off feed rates which apply to each nose radius tool, in each case the minimum feed rate is defined as that at which the material removal mode becomes brittle according to Arif's et al's (2013) criteria, and the maximum limit to the feed rate is that at which the feed rate reaches the width of cut, such that effective machining cannot take place at the depth of cut required.

It was observed broadly that decreasing the nose radius, increasing the negative rake angle and increasing the clearance angle have the effect of increasing the DBT depth at a given feed rate. The DBT depth was in all cases considered limited by the threshold force at which sub-surface damage occurs. The analysis suggests that there are several different tool configurations which could be used. It seems, for example, that feed rates can range from 5-15µm/rev, and that depths of cut can range from 5-20nm. In the next section the analysis is repeated including consideration of the heating effect of µ-LAM.

4.1.3 Analysis for Integration of Laser

In this section calculations for cutting effectiveness are presented taking heating by µ-LAM into consideration. Below, table 4-5 shows the predicted critical depths of cut, but using laser, according to Bifano's (1982) formula.

Table 4-5 Critical Depths of Cut

Material	Young's Modulus (GPa)	Fracture Toughness (MPa $m^{1/2}$)	Hardness (GPa)	Calculated Critical Depth of Cut (nm)	Ravindra's (2011) Obtained Critical Depth of Cut (nm)	Mean Critical Depth of Cut (nm)
4H-SiC	347.01	1.33	13	41.9	35	38.45

It can be seen that the calculated critical depth of cut is approximately 270% greater with laser than without, indicating that DBT depths are likely to be greater through the use of laser. Table 4-5 shows the critical crack length with the altered material properties:

Table 4-6 Critical Crack Lengths

Material	Fracture Toughness (MPa $m^{1/2}$)	Hardness (GPa)	Critical Crack Length (µm)
4H-SiC	1.33	13	1.256

It can be seen from table 4-6 that a reduction of nearly 25% is observed in the critical crack length. As such, the question arises of whether the feed rate is limited to the same extent by the induction of sub-surface damage in the case that the critical crack inducing force is exceeded, as is shown in figure 4-16.

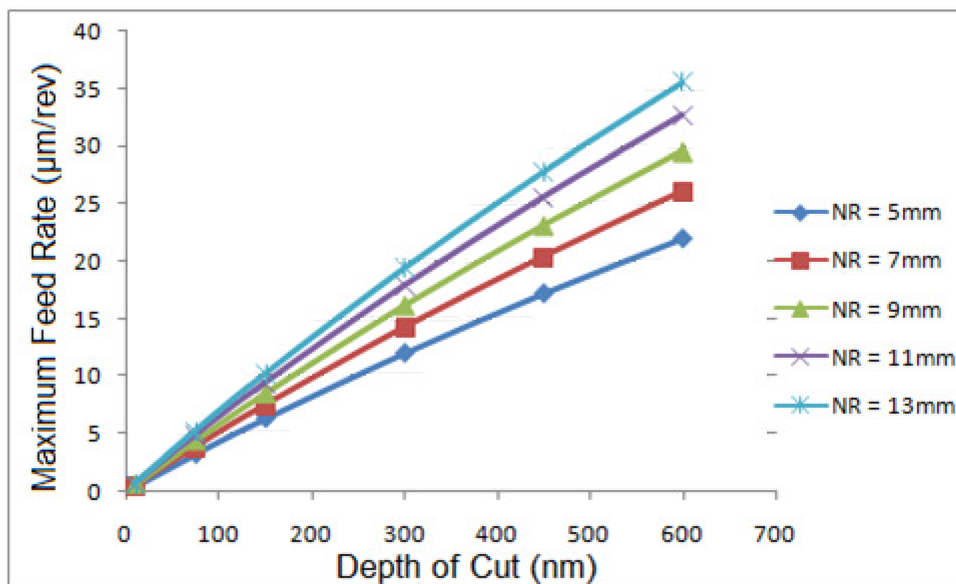

Figure 4-16 Maximum Feed Rate (NR = 3mm, clearance = 10)

It can be seen that while the situation is slightly improved, that at shallow depths of cut below 300nm it is still not possible to reach the required 25 µm/rev of feed which is required by the

optical setup. As such, it will be necessary to maintain the cutting force below the threshold force at which sub-surface damage begins to be induced.

In order to analyse the cutting performance possible with laser, figure 4-17 was created relating DBT depth to feed rate under the cutting conditions with laser, for tools of different nose radius.

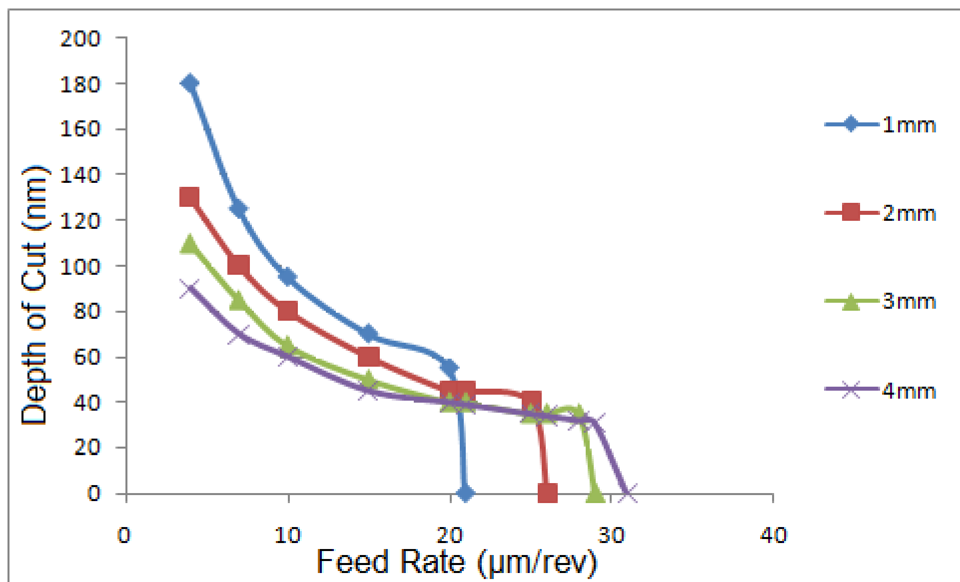

Figure 4-17 DBT Related to Feed Rate

The graph shows the DBT depths for nose radii 1-4mm, which are for the most part limited by the cutting force induced, as this would otherwise cause sub-surface damage. It can be seen from the graph that as feed rates of 25µm/rev or more are required (as in the case of 1000nm laser), that a nose radius of 3mm or greater is needed, as feed rates are limited by the width of cut implied at the depths of cut for which sub-surface damage is not induced. It can be seen that depths of cut of approximately 30-50nm are achievable in this case, using tools of 3-4mm nose radius at feed rates of 25-30 µm/rev. It is noteworthy that at lower feed rates (such as 7µm/rev in the case of the 294 nm laser) the DBT depth increases, and for feed rates in this range, that depth of cut is no longer limited by cutting forces causing sub-surface damage, as the feed rates fall within acceptable ranges for cracking to be allowed. In these cases the DBT depth of cut is limited by Arif's (2008) criteria, and extends to several microns depending upon the tool edge radius and wear land.

It is evident from the preceeding analysis that DBT depths are indeed increased by the use of laser as predicted by the literature review, and that different mechanisms can begin to act to limit DBT depths with the use of laser at lower feed rates. It seems that the use of the lower wavelength identified in the optical design, by enabling lower feed rates to be taken, enables overcoming of the requirement to limit forces to avoid induction of sub-surface damage, thereby

allowing higher DBT depths of cut to be taken which are limited by factors relating to the energy involved in material removal and crack propagation.

4.1.4 Expected Optical Performance

As discussed in section 4.2.3, the effect that temperature increase due to laser has upon chemical wear of the diamond tool is investigated in this section, along with consideration of thermal shock.

With regards to thermal wear of the diamond tool, formula 3-33 describes how the rate of diffusive wear relates to temperature. The methodology is carried out to create the graph in figure 4-18.

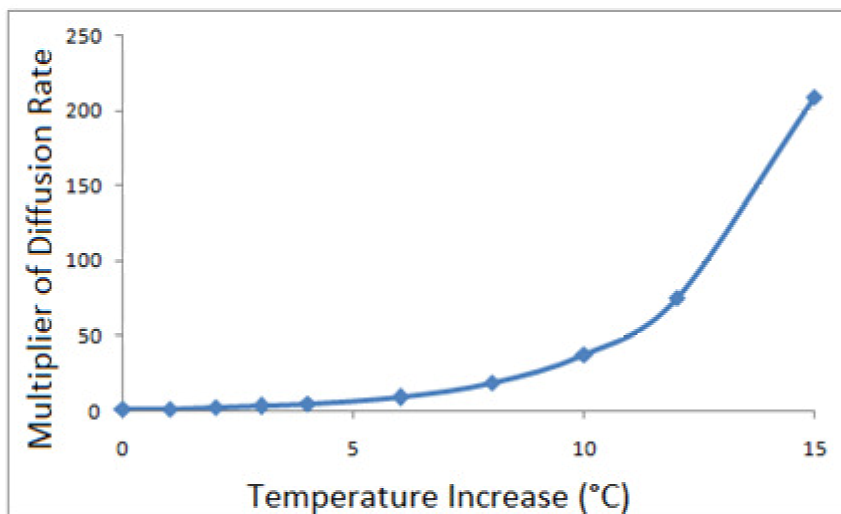

Figure 4-18 Predicted Increase in Diffusion Rate

The chart shows that diffusion rates are predicted to increase exponentially with increasing temperature, and that with an increase of just 15 °C that the diffusion is predicted to increase by a factor of approximately 200. In fact, it is predicted that once the temperature has been raised to the melting point of silicon that the diffusion rate will have increased by 38 orders of magnitude. Yan (2003) describes how significant diffusion was observed to cause significant crater wear in the machining of silicon, indicating that the increase in diffusive wear brought about by laser heating is likely to cause significant chemical wear in the diamond tool. Silicon carbide, however, is not prone to diffusive wear, so wouldn't be affected by this issue.

With respect to graphitisation of the diamond tool, temperature increases from the temperature induced by abrasion (Luo et al, 2012) to the temperature caused by laser heating to the melting temperature of the of the material are predicted to be according to table 4-7.

Table 4-7 Temperature Increases for Diamond Graphitisation

Material	Abrasion Temperature (°)	Melting Temperature (°)	Temperature Increase (°)
3C-SiC	900	2730	1830
6H-SiC	750	2730	1980
Silicon	700	1414	714
4H-SiC	450	2730	2280

Formula 3-31 in section 3.3.1 is therefore used to predict the percentage increase in graphitisation of the diamond tool, shown in table 4-8.

Table 4-8 Predicted Increases in Graphitisation

Material	Factor Increase in Diamond Graphitisation Rate	
	Ea = 730 kJ/mol	Ea = 1060 kJ/mol
3C-SiC	10^{28}	10^{41}
6H-SiC	10^{37}	10^{53}
Silicon	10^{27}	10^{40}
4H-SiC	10^{71}	10^{103}

The table shows that graphitisation is predicted to increase exponentially at the higher temperatures involved. It is not known whether the same mechanism of graphitisation induced by abrasion is indeed likely to occur, but the analysis is predictive of excessive tool wear. It is, however, encouraging that experimental studies (Shayan et al, 2009) do not describe excessive diamond tool wear by graphitisation, indicating that the application of the formula for graphitisation with the parameters identified may not be applicable.

With regard to thermal shock, formula 3-34 is used to determine the maximum changes in temperature with the parameters in table 4-9.

Table 4-9 Parameters used for predicting maximum temperature change

Parameter	Value for Silicon Carbide
Compressive Strength (GPa)	3.9
Poisson's Ratio	0.212
Thermal Expansion Coefficient (µm/°C)	4.0
Young's Modulus (GPa)	347.01

The resulting maximum temperature change is 2214°C for silicon carbide, which is less than the change in temperature required by the process.

4.2 Preliminary Analysis of Tetraform C

4.2.1 Design Assembly of the Tool

The first optical design suggested relies upon the use of the components which are illustrated in the figure 4-19.

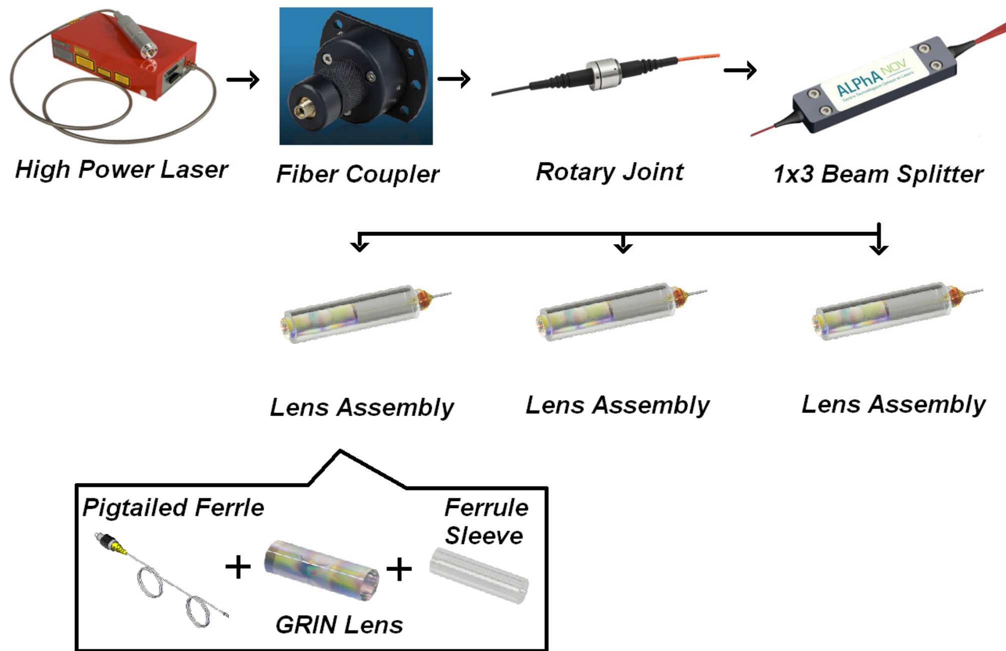

Figure 4-19 Final Optical Setup

The second optical design uses identical optical components, except that the beam splitter is substituted by the one shown in figure 4-20, which is able to accommodate light at the lower wavelength of 294nm (a laser of the appropriate wavelength is used, full specifications for the optical and mechanical components are shown in the appendix). An adaptation which may be required is cutting the GRIN lens to size, which can allow for the lower wavelength of light to be transmitted effectively.

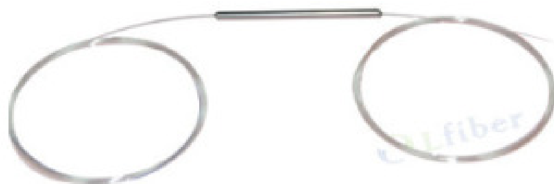

Figure 4-20 7Beam Splitter for 294nm Wavelength Light

Optically, the laser beam starts at the high power laser, from which it is emitted into the fibre coupler. The fibre coupler couples light into a fibre optic cable which carries it to the rotary joint, enabling rotational motion of the beam beyond this point. The light then travels through further fibre optic cables to a beam splitter, which splits the beam into three separate beams. Each beam then travels through further fibre optic cable to a lens assembly, which consists of a pigtailed ferrule which is mated to a GRIN lens within a ferrule sleeve. The GRIN lens works to focus the light onto the tip of the diamond. The way in which the light is positioned so that it accurately focuses on the diamond is discussed in section 4.1.3

The components selected for the 1000nm wavelength are specialist insofar as they are selected based upon their high power ratings, and operate in the wavelength ranges of the light (~1μm), their power ratings are shown in table 4-10.

Table 4-10 Power Ratings of Components in Optical Setup

Component	Power Rating (W)
Fibre Coupler	150
Rotary Joint	200
1x3 Beam Splitter (1000 nm)	200
1 x 3 Beam Splitter (294 nm)	10

It can be seen from the above table that by delivering 150W to the fibre coupler, this can be split equally into three sets of 50W (neglecting losses), which is deliverable to each diamond, comparing well to powers used previously in μ-LAM (eg 25W- Ravindra, 2011). An advantage of the optical setup is that it can be used with lasers of different powers, so long as they are within the required wavelength of the components. For the case of 294nm wavelength light, lesser powers are required as indicated in section 4.1.1. The beam splitter used for the lower wavelength light is capable of up to 10 W in power, meaning that nominally 3W is deliverable to each diamond, exceeding the requirements specified in section 4.1.1.

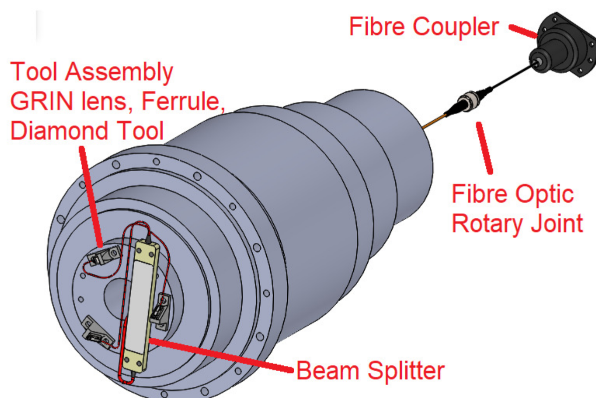

Figure 4-21 Final Optical Assembly

Formula 3-5 was used, knowing that the core diameter of the components selected was 100µm, to determine that the minimum spot size achievable is likely to be 25 µm for the 1000 nm laser, and 7 µm for the 294 nm laser.

Several different concepts were explored in the optical design, which for completeness are outlined here, with rational for their adoption or otherwise. The final assembly is shown in figure 4-21. At first two initial design concepts were identified, which are shown in figures 3-8 and 3-9.

The first design concept (figure 3-8), shows the mechanical tool with an electrical slip ring mounted on it, such that the electrical supply comes in from the side of the tool, and can be fed to individual laser diodes mounted on the rotating tool itself, which ultimately are focused onto each diamond. The first concept has several advantages, especially that it is not necessary to install a cable through the centre of the machine's spindle, meaning that the tool could exist as a stand-alone, off the shelf item that could be fitted to machines relatively easily. There are, however, several drawbacks to this concept- laser diodes, while they provide enough power, often need cooling which could be impractical; and crucially, multi-mode laser diodes have very high M^2 values, which mean that their spot sizes could not be focused to be small enough. For this reason the first concept was abandoned, and the second concept was explored further.

The second design concept shows the mechanical tool with a laser delivered to its diamonds, which enters through the centre of the tool, through the centre of the spindle of the machine- this is the concept that was ultimately adopted in this investigation.

In the initial optical design, a problem which was encountered was that it was difficult to source parts which would allow enough optical power to pass to the rotating part of the tool- because of this, the option of using a laser amplifier was considered. This option was discarded because it would only cause a small amplification in the power of the laser, and the amplifier would require an electrical feed which would also need to rotate- the apparatus is also excessively expensive.

The option of using a fibre optic rotary joint with multiple fibres was considered, as shown in figure 4-22. This would allow for more power to pass through the rotating joint, which could be combined using beam splitters. This option was ultimately discarded because it would be impractical to use the large number of beam splitters that would be required, and there would be excessive losses in the large number of optical components needed.

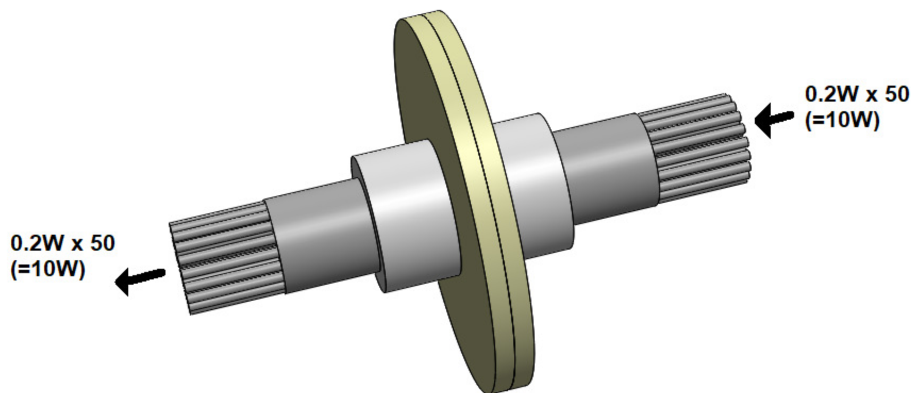

Figure 4-22 Multiple Fibre Rotary Joint

A further option which was considered was combining the light outputs from several different laser diodes using beam splitters/combiners, as shown in figure 4-23. This would allow the light from five 2W laser diodes, for example, to be combined into one 10W output. This option was again discarded for the same reason that multi-mode laser diodes produce light which cannot be focused to a small enough spot size.

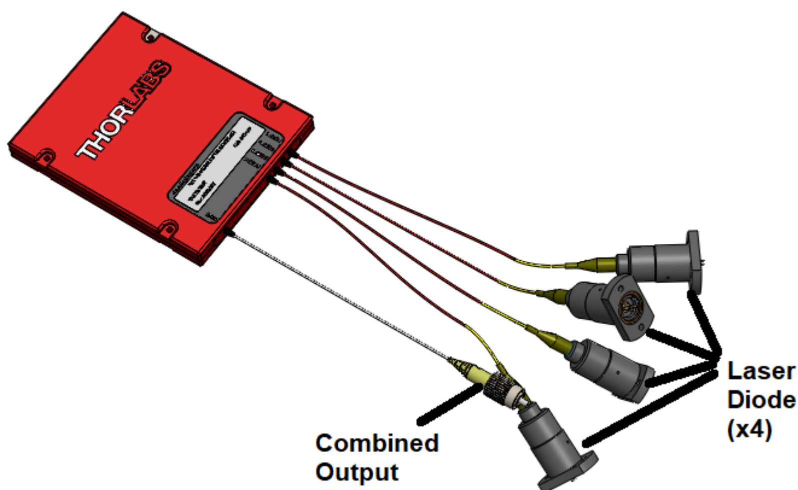

Figure 4-23 Combined Laser Diodes (CAD Parts from Thorlabs.com)

An alternative option that was considered was mounting the laser system itself (non-diode) in the centre of the tool, the output of which could be split to the several different diamonds. This option was discarded as it seemed impractical, as lasers should ideally be kept still, and would be too large to mount in the small spaces available.

A problem that arose in selecting the components was that while components of sufficient power could sometimes be found, these components were not always compatible with each other- they would, for example, have fibre cores of different sizes. An option that was therefore

considered was to use components that had mismatched fibre optic core sizes, as when light flows from a larger fibre to a smaller one, that some of the light is lost, but some of it passes through and can be used, as shown in figure 4-24. This option would have meant that the laser powers required would have far exceeded the output at the diamond tips, but that with a powerful laser some useful heating could be caused at the diamond tips. Fortunately it was possible to source components which both met the power requirements and were fully compatible with each other.

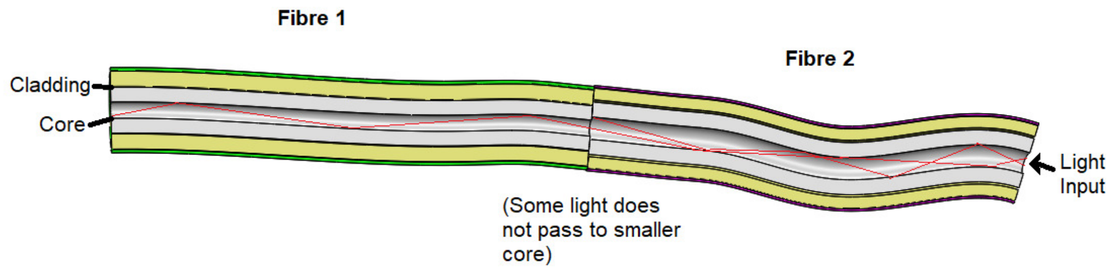

Figure 4-24 Size Mismatched Optical Components

Mechanically, it is suggested that three individual stainless steel tool fixtures be used which are attached to the spindle as shown in figure 4-25. The number of diamonds that could be used, based upon the torque of the machine was excessively large. There is an option to remove some of the tools so that one or two tools only are in use, and to add further tools by using multiple beam splitters. The beam splitter and optical fibres are screwed to the spindle using straps.

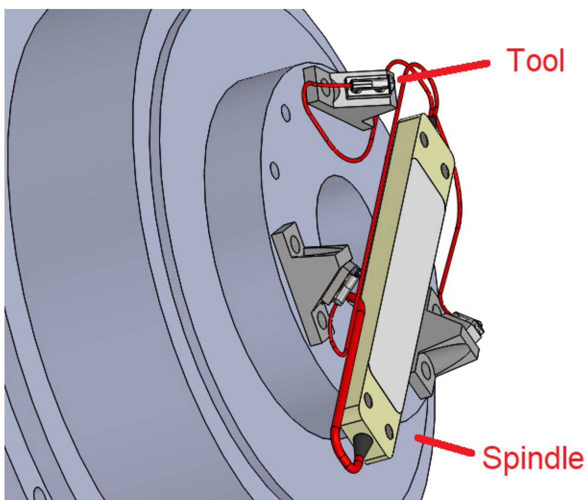

Figure 4-25 Tool Fixtures for Diamond Tools on Spindle

The fixtures are designed in such a way that the diamonds are inclined at 46°to the horizontal. This is done so that, with a -1° rake angle on the diamond, the effective rake angle is -45°. A -1° rake angle was used on the diamond tool because this ensured that the laser beam passed

directly through the diamond. The material selected for this component and for the supports for the spindle is stainless steel 304, this was selected because it offers more stiffness than aluminium, and is corrosion resistant (as opposed to mild steel), and cheaper than stainless steel 316.

The first concept considered for the tool stands was making the fixture hollow as in figure 4-26. This would minimise the moving mass, and thereby reduce instability created by excessive momentum. The concept was not carried forward because a requirement was to maximise the stiffness of the fixture in the Z direction, which would be negatively impacted by using a hollow design.

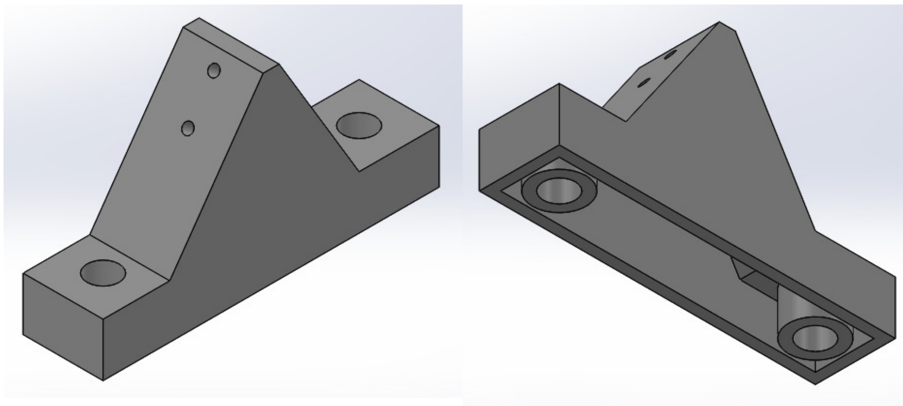

Figure 4-26 Hollow Tool Fixture Concept

The second concept considered, of having multiple angles for the tool on the same fixture, is shown in figure 4-27

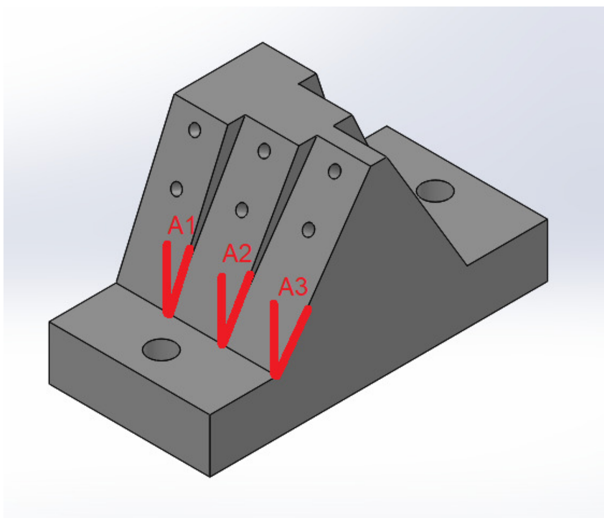

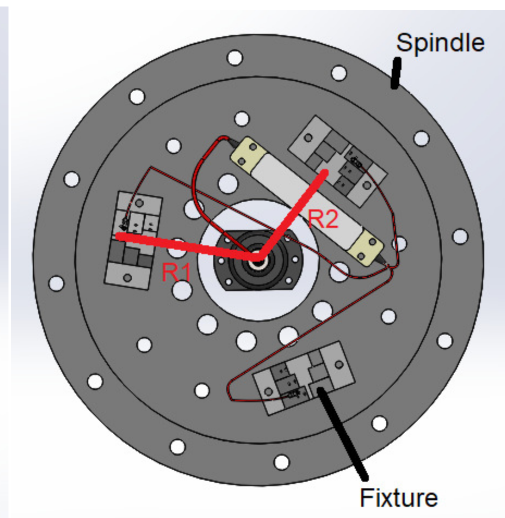

Figure 4-27 Multiple Angle Tool Fixture

Figure 4-28 Differing Swing Radii

The fixture would work by allowing the same diamond tool to be fitted to one of several locations, such that the effective rake angle can be altered by positioning it in a different location. The advantage of this approach is that it allows for flexibility in the rake angle that is used, without having to purchase several different fixtures of different angles. The concept was abandoned because moving the tool from one position to another would effectively alter the swing radius of the tool, as shown in figure 4-28.

The third option considered for the tool fixture was to use a more organic design (Wong and Hernandez, 2012a) relying on Additive Layer Manufacturing (ALM) for the manufacturing method. An example of the type of item which could have been used is shown in figure 4-29. It was determined that the risk of problems that could be caused because of the complexity involved in designing a freeform tool fixture outweighed the advantages gained through the use of this concept, so it was not carried forward.

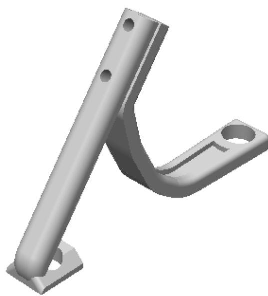

Figure 4-29 ALM Tool Fixture

The diamond tool holder is screwed onto the stand with two screws located through its centre. The diamond tool holder also has a groove which lies central along the tool, which allows the lens configuration to be located centrally. This is done at a height so that the beam focuses nominally at the tip of the diamond (as shown in figure 4-30, as opposed to the misaligned laser shown in figure 4-31).

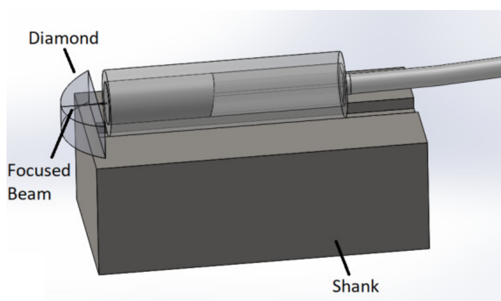

Figure 4-30 Focused Laser Beam

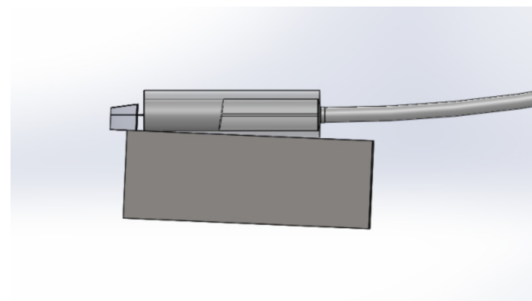

Figure 4-31 Misalignment Laser Beam

The first option considered for coupling the optical system to the mechanical tool was to use standard optical components such as lenses and collimators to focus the light down onto the tip of the diamond. The problem with this approach was that because the tool will be subjected to high accelerations, it is unlikely that it will be robust enough to remain focused accurately on the spot of interest. This was one of the main reasons for opting to use a GRIN lens. The benefit of this is that it is a small and robust item, which does not consist of several parts. Fixing the GRIN lens in place, however, remained a problem- as again the normal fixtures were unlikely to stand up to the forces involved. Because of this, a design has been put forward which is described here. The configuration is as in figures 4-32 and 4-33.

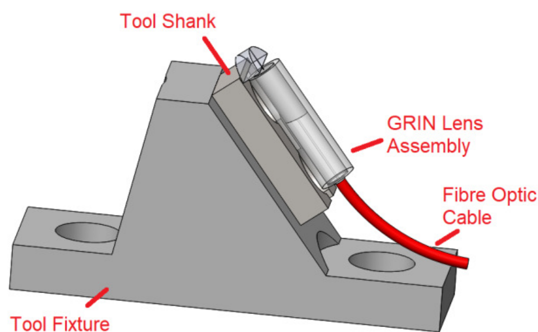

Figure 4-32 Adopted Optical Setup

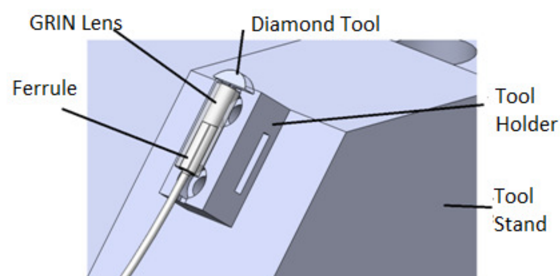

Figure 4-33 Diamond Tool Configuration

It is suggested that the GRIN lens be located on the tool mount in such a position that, according to its nominal dimensions, it focuses light exactly on the tip of the diamond. As Ravindra (2011) described, it is necessary in µ-LAM for the laser to be focused exactly upon the cutting zone so that it preferentially heats the HPPT phase of the material; and it must be adjusted so that this is the case. In the case that the beam is not focused entirely upon the HPPT phase, combustion of the workpiece is possible as evidenced in the following section.

The suggestion put forward is that the GRIN lens be fixed in place with the strap in the groove on the tool holder, but that a layer of padding (a thin sheet of plastic) be placed between the GRIN lens and the tool holder. It is anticipated that by altering the number of sheets of plastic, that it will be possible to adjust the position of the spot. Plastic sheets of only tens of microns can be sourced, which when in compression can allow for fine enough adjustments to be made to position the beam. This design is resistant to forces caused by acceleration of the tool in a way which conventional equipment would not be.

In the case of the GRIN lenses being used, the focal length is 1.92mm, the beam diameter is 100 µm, and the wavelength of light is 1000 nm. Given these parameters the depth of focus can be calculated as 0.90mm. As it is commonly possible to manufacture components to within 0.25mm tolerances, so it is predicted that it will be possible to manufacture the shaft of the tool such that the GRIN lens is positioned so that the beam is focused accurately enough in the

longitudinal direction (as a guideline, a 5% change in beam diameter causes a loss in intensity of only 9.3%).

An important consideration in the optical setup is the way in which the laser beam is aligned with the diamond tip. In order for effective heating to be carried out, it is necessary for the laser beam to be focused exactly at the tip of the diamond, where the HPPT phase of the material being cut is located. Ravindra (2011) achieved this by coating the diamond initially in an opaque coating (as shown in part 2 of figure 4-34), and then performing a very shallow cut in the material, removing the coating at the centre of where the diamond contacts the material (part 3). He then shone the laser through this point, and measured the intensity of the light coming through the diamond with a camera (part 4). By adjusting the position of the laser lens so that the intensity was a maximum, Ravindra was able to effectively align the laser to the tip of the diamond (part 5). It is suggested that the same approach be used for this application.

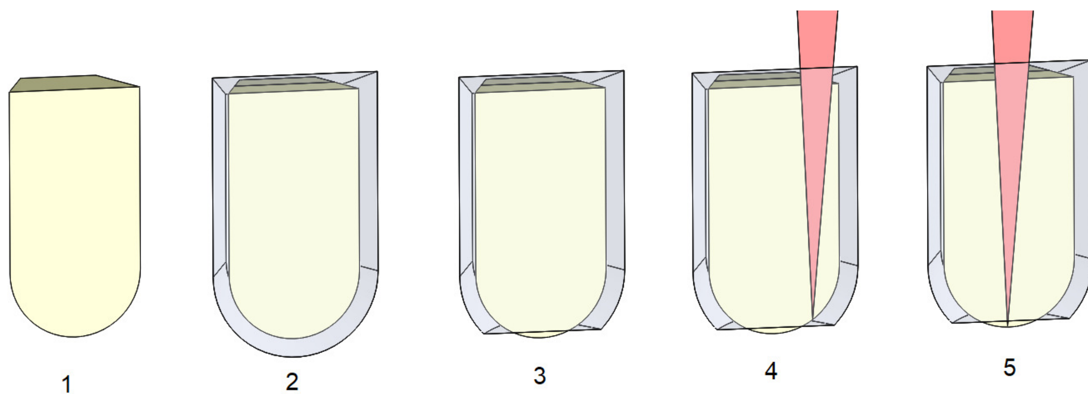

Figure 4-34 Aligning of Laser Beam

With regards to the design for the adaptation of the Tetraform C machine, the first decision was whether the replacement spindle should be mounted on the existing Z axis of the machine, or if the replacement spindle should be mounted rigidly, using a moving Z axis as part of the table for the machine. The deciding factor was that the former accuracy of the Z axis motion was 1 µm Arai (2004). Given that the largest depth of cut for which ductile regime machining was reported by (Ravindra, 2011) was 0.26 µm, it can easily be seen that using the previous Z axis configuration would not be an option for the implementation of the multi-turret µ-LAM tool. The option remained to install a new Z axis to move the spindle, but this was discarded as it was deemed to be too complex to move such a large moving mass accurately.

Having established this, it became apparent that Z axis motion would be necessary in the X table of the machine. Two options became viable, either replacing the entire XY table with a new configuration, that incorporated Z motion; or installing a new component onto the existing table which allowed for Z axis motion. As the minimum number of changes to the machine was preferred, it was decided that an additional module could be installed on the machine allowing

for Z axis motion. It was also decided, because the purposes of the current investigation are primarily to prove the concept of the proposed tool, that it would suffice to only use the X axis, without the use of the Y axis or a rotational axis for moving the workpiece.

In the Tetraform C machine, modified according to the proposals in this report, the machining loop consists of the arrangement of components shown in figures 4-35 and 4-36.

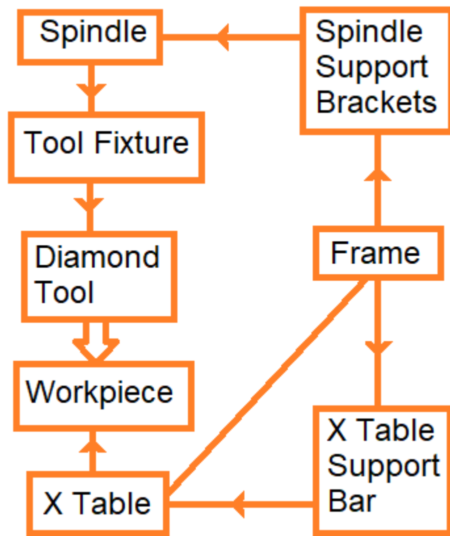

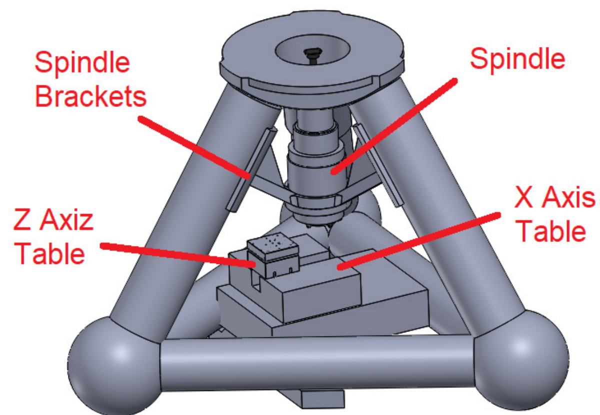

Figure 4-35 Machining Loop **Figure 4-36 Components on Tetraform C**

The procedure outlined in section 3.4.1 was followed to create the graph in figure 4-37 showing cutting speed plotted against material removal rate, at a feed rate of 30µm/rev, for different depths of cut:

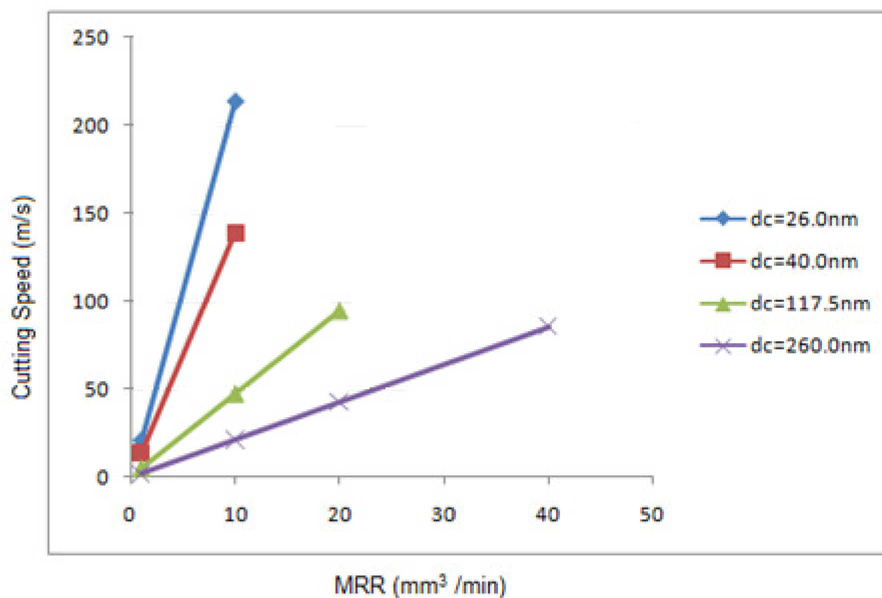

Figure 4-37 MRR Correlated to Cutting Speed (s=30µm/rev)

It can be seen that a linear relationship exists between cutting speed and MRR, with deeper cuts requiring less cutting speed to achieve higher material removal rates.

It is noteworthy that the limitation on spindle speed of 10000rpm imposed by the fibre optic rotary joint selected implies a maximum cutting speed of 45m/s considering the geometry of the spindle under consideration. This limitation is imposed because the availability of fibre optic rotary joints of sufficient power handling capability is not well developed, and after an exhaustive search it was determined that the fibre optic rotary joint selected has the highest rotational speed of those that are capable of withstanding the optical power required. At the limiting speed of 45m/s- MRR rates are 1.4, 2.2, 6.4 and 14.2mm^3/min for depths of cut of 26.0, 40.0, 117.5 and 260.0nm respectively. As these material removal rates are at the lower end of the MRR specification, it is suggested that the maximum cutting speed of 45m/s be possible, to ensure that the performance of the cutting tool is comparable with that of similar processes like SPDT (with MRR of 1-100mm^3/min).

It was necessary to specify two new components that would enable the adaptation of the Tetraform C machine: the spindle/motor and Z axis table. The two parts are shown in table 4-11, along with their relevant performance features (full specifications are in the appendix):

Table 4-11 Performance of Components selected for Adaptation of Tetraform C

Item	Model	Performance	Description
Spindle/Motor	ISO 5.5F	<12.5 nm <12.5 nm 228 N/micrometer 10 000 rpm	Axial error Radial error Axial stiffness Maximum Speed
Z Table	M-501.1DG	Nm 12.5 mm 1 mm/s	Design resolution Travel range Max velocity

The configuration is shown on the Tetraform C machine in figure 4-38.

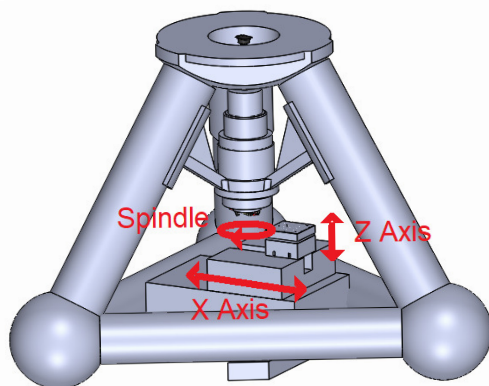

Figure 4-38 Axial Motion of Configuration

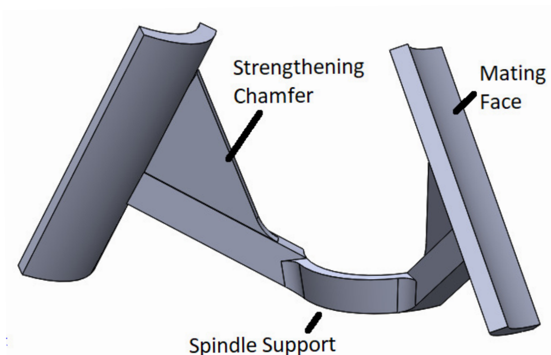

Figure 4-39Spindle Support Brackets

Figure 4-39 shows the spindle support brackets that were designed to fix the selected spindle to the frame of the Tetraform C. Three brackets are used in all, made of stainless steel 304 for rigidity and corrosion resistance. The part was modified based upon FEA results (using a methodology as described in section 3.5) to minimise deflections that occur in the vertical direction.

In this section components which can be used to implement the design of the multi-turret μ-LAM tool upon Cranfield University's Tetraform C machine tool are presented. The components selected allow for machining within the constraints set in the specification in section 3.1, although the spindle speed achievable (while abiding by constraints imposed by the fibre optic rotary joint selected) is lower than would be desirable. It can be seen that components are available which allow for the implementation of the optimal designs which were arrived at in section 4.1, and that the implementation of the proposed tool therefore appears to be feasible. The task remains to assess the suggested implementation of the tool to determine whether accuracies required for ductile mode machining of the materials of interest is feasible with the configuration presented- this is undertaken in section 4.3.

4.2.2 Modal Analysis

In the modal analysis, the modes which were identified which are displayed in figure 4-40 (the arrows indicate the frequencies at which distinct modes appear to be excited).

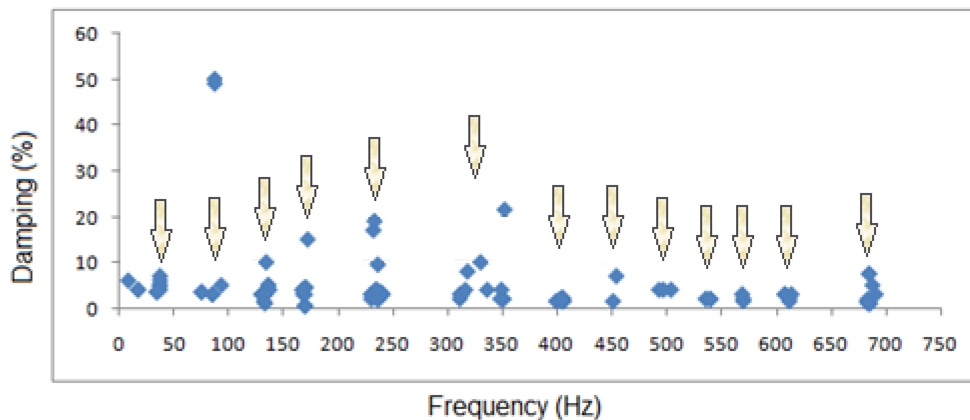

Figure 4-40 Modes Identified in Experimentation

The modes excited in each member (as shown in figure 4-40) were as in table 4-12.

Table 4-12 Modes Detected in Tetraform C

Member	Frequencies of Modes (Hz)
Front Horizontal Beam	123, 132, 132, 133, 136, 166, 170, 170, 230, 240, 350, 351, 612,
Left Horizontal Beam	85, 87, 130, 130, 130, 131, 169, 311, 405, 536, 540
Right Horizontal Beam	237, 172, 240, 239, 168, 169, 169, 352, 397, 608, 684, 318, 614, 691, 404, 404
Left Upright Beam	238, 238, 238, 133, 238, 93, 134, 348, 493, 313, 572, 504, 451, 497, 570, 406
Right Upright Beam	309, 350, 240, 351, 239, 355, 239, 131, 134, 89, 236, 316, 571, 235, 404, 239, 350, 400, 570, 239
Rear Upright Beam	685, 232, 235, 235, 37, 336, 569, 236, 454, 685, 235, 454, 485, 235
Left Ball	405, 405, 233, 404, 234, 17, 37, 133, 8, 132, 37, 684, 612, 684, 404, 404, 405
Right Ball	403, 349, 330, 37, 167, 131, 167, 17, 37, 37, 686, 316, 683, 405, 608, 688, 403
Rear Ball	34, 34

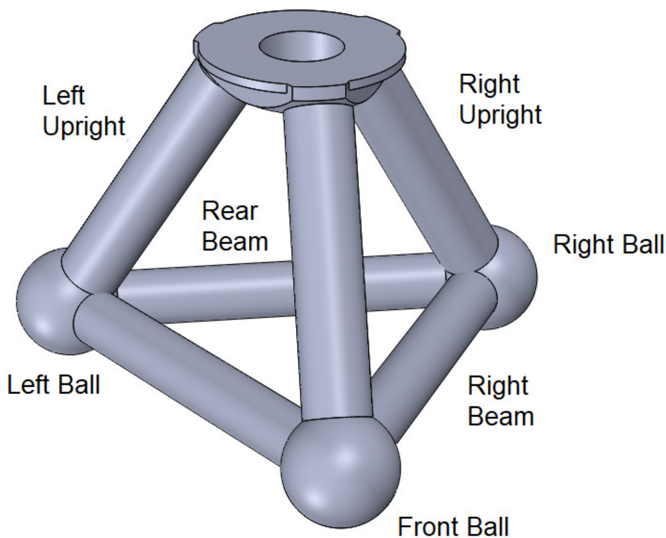

Figure 4-41 Components of Tetraform C Tested

After carrying out the procedure for narrowing down on the modes of most interest (described in section 3.4.2), the table 4-13 shows the rigid body modes which were identified by the process:

Table 4-13 Modes Identified by Analysis

Mean Frequency (Hz)	Mean Damping (%)	Number of Detections	Number of members detected on
132	3	18	7
169	3	8	4
235	3	11	5
313	3	4	4
350	3	4	3
405	2	12	6
570	2	3	2
611	2.5	5	4
686	2	7	3

The table shows that a large number of modes were identified, from the first natural frequency at 36Hz. to 686 Hz. Arai (2004) highlighted two frequencies of vibration which were said to be dominant in the Tetraform C, 152.8Hz and 287.2Hz- which the current investigation did not identify. Arai carried out his testing of the machine when the rotary table was installed, among other components, so it is possible that these changes in mass affected the results obtained. A criticism of the current study was that impacts were only delivered at 3 points on the machine- it is possible that had other points been used, that different modes may have been identified.

In any case, the frequencies which are likely to be caused on the machine are outlined in table 4-14, followed by the justification for their consideration. These frequencies are then compared to those of the identified modes (and those of Arai, 2004).

Table 4-14 Sources of Vibration

Source	Frequency (Hz)
Spindle	>2000
Cutting Tool	>500

Table 4-14 shows some of the frequencies which are likely to be encountered in the operation of the tool on the Tetraform C. As the cutting speed required is likely to be up to 45m/s, the calculations are based upon the corresponding RPM of the spindle (~10000Hz), with the rotational symmetries of the rotating parts. As there are 3 cutting tools, these are likely to have rotational symmetry of 3, resulting in an effective frequency of up to 500Hz. The spindle has rotational symmetry of 12 in terms of fixings, resulting in frequencies of up to 2000Hz. It is

noteworthy that the lowest natural frequency detected on the Tetraform C machine was 132Hz, suggesting that from the results obtained, that there are several modes which could be excited by the rotation of the spindle. Based upon the results obtained, it is suggested that the spindle not be operated at speeds of: 8100, 7000, 6260, 4700, 3380 and 2640 RPM.

4.2.3 Validation of Laser Heating

It was found that by using 40W at 100mm/s, heating exceeded 1000°C- under these conditions the substrate combusted. The results found seem to indicate that silicon does in fact absorb enough energy at high laser travel speeds for significant heating to occur, and potentially for µ-LAM to be effective. It should be noted, also, that the silicon used in this trial was in the pristine phase, whereas the silicon undergoing laser heating in µ-LAM is of the HPPT phase, which absorbs more light.

A criticism of the validity of the results is that when viewed, little heating seemed to occur when the laser started, it was only after several seconds that the silicon seemed to absorb enough energy and began to combust. This may indicate that the shape used in the experiments (a square) allowed excessive energy to enter the substrate in a compact surface area, whereas in actual machining the laser would not pass over paths in such close proximity to each other. The fact that the silicon absorbed enough energy to reach the desired temperature is, however, indicative that substantial heating does indeed occur at high speeds of travel.

4.3 Error and Uncertainty Predicted for Design

In this section inaccuracies are calculated for each component in the machining loop as described in section 3.5, followed by a table summing up the errors-allowing for the accuracies of the proposed configuration to be compared to the accuracies required to achieve the depths of cut required according to sections 4.1.2 and 4.1.3.

The accuracies of the Z axis table according to the manufacturer are shown in table 4-15.

Table 4-15 Accuracies of Z Axis Table

Parameter	Value
Design Resolution	5nm
Pitch	+/- 15 µrad
Yaw	+/- 15 µrad

With regards to the Z axis accuracies of the component, it can be seen that a 5nm error is inherent in the design of the component. While the pitch and yaw contribute to lateral inaccuracies, their effect upon the Z axis accuracy can be shown to be negligible.

Another part of the machining loop which is considered important is the fixing of the table to the machine. The table is supported from underneath by a beam which crosses the length of the machine (as shown in figure 4-42) and it is connected by a fixing to one of the members of the frame on the other side. FE analysis was also carried out on these components to determine the deflection likely to arise in this part of the machine. Because it was not practical to determine the deflection likely to occur in the table itself, the deflection in the beam was calculated.

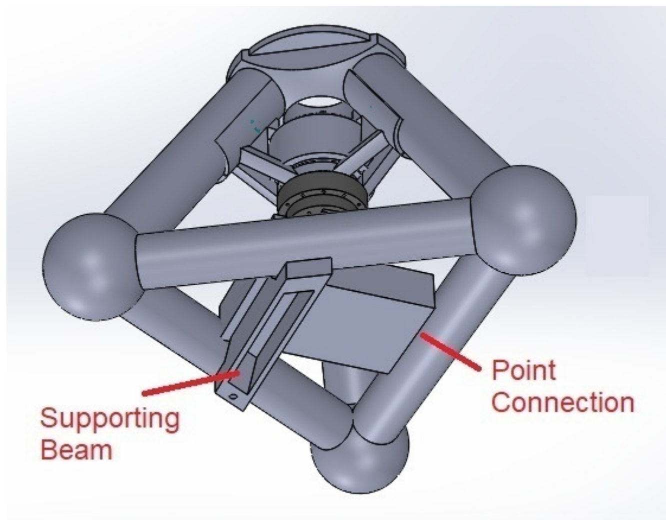

Figure 4-42 View from Underneath Tetraform C

With regards to the deflections of the frame, Arai (2004) describes how the stated stiffness of the frame is 100 N/µm. Accordingly, table 4-16 shows the deflections caused for the different loading conditions:

Table 4-16 Deflections in Tetraform C Frame

Si, Dc = 260 nm, F_t = 2.2N	**Si, Dc = 100 nm, F_t = 0.26N**	**SiC, Dc = 117.5nm, F_t = 1.1N**	**SiC, Dc = 60nm, F_t = 0.57N**
22	2.6	11	5.7

The combined inaccuracies predicted by the analysis are shown in table 4-17.

Table 4-17 Combined Accuracies in the Z Direction

Component	**Predicted Z axis Accuracy (nm)**			
	Si, Dc = 260 nm, F_t = 2.2N	**Si, Dc = 100 nm, F_t = 0.26N**	**SiC, Dc = 117.5nm, F_t = 1.1N**	**SiC, Dc = 60nm, F_t = 0.57N**
Spindle Errror Motion	<12.5	<12.5	<12.5	<12.5

Spindle Stiffness Error	9.6	1.1	4.8	2.5
Z Axis Table	5	5	5	5
Tool Fixture	17	4	8	4
Spindle Brackets	6	0.7	3	2
X Axis Supporting Beam	8	1	4	2
Tetraform C Frame	22	2.6	11	5.7
Total	<80.1	<26.9	<48.3	<33.7

The table confirms that the accuracy predicted for the components is highly dependent upon the thrust force applied, which results from the depth of cut being utilised. It is noteworthy that not all sources of inaccuracy have been identified, but it is encouraging that by considering the most obvious sources of error, that for all depths of cut, the inaccuracies predicted are less than the depths of cut, constituting 30%, 27%, 41% and 56% of the depth of cut. The results are encouraging as the configuration seems likely to be capable of cutting silicon, and some polymorphs of silicon carbide in the ductile regime. It is also significant that the summation of the errors shown represents the worst case error, for example when all of these error sources act in the same direction. It is likely that in practice the errors would sometimes act in opposing directions, thereby cancelling each other out. Additionally, a great proportion of the errors are caused by strain in the components, which may be a repeatable error which can be adjusted for in setting the cutting parameters. In any case, it remains encouraging that the design need not be discarded as impractical when considering the more obvious sources of error.

5 RECOMMENDATIONS AND FUTURE WORK

Several findings of interest have been obtained in the course of the investigation, these are discussed here along with their implications and recommendations and future work which can be carried out.

Overall it seems that implementing the concept proposed is feasible, and that it is likely to offer improved cutting performance. It was possible to source optical components which allow for the implementation of the tool at two different wavelengths, and the mechanical components were designed and sourced which would enable the tool to be implemented upon a machine tool- thereby providing evidence that the concept is practical to implement.

The design was evaluated analytically for improvements in cutting performance and resistance to tool wear, and the results indicated an increase in cutting depths that could be achieved (and therefore material removal), and also in the resistance to tool wear.

The novel methodology for selecting the wavelength of laser is expected to be capable of enabling improved performance in µ-LAM. While lasers with wavelengths of 1000nm have traditionally been used, it is expected that by selecting the wavelength such that a constant temperature is maintained in the workpiece, and that if this temperature more closely approaches the melting temperature of the material, that the benefits of µ-LAM can be greatly enhanced. A limitation of the technique presented is that it used absorptivity values of pristine silicon, whereas the absorptivity values for amorphous silicon may be more appropriate. While this data, and absorptivity values for phases of silicon carbide in the HPPT zone, are not widely available, Green (2008) presents a methodology whereby the necessary data can be evaluated based upon findings of other studies. There seems to be ample scope for further studies concerning the effect of laser wavelength upon the performance of µ-LAM to be carried out, and more specifically for studies implementing the technique put forward in this investigation of more closely approaching the melting temperature of the material by controlling the wavelength of laser light used with respect to rates of decreasing absorptivity with increasing temperature.

A noteworthy aspect of the selection of wavelength is that, when 1000nm was used as the laser wavelength, cutting was severely inhibited in terms of the feed rate possible, with a minimum of about 25 µm being possible. In the case where the lower wavelength was considered it was possible to reduce the spot size used, and thereby reduce feed rate.

Problems which may be caused involving increased chemical wear of the diamond tool at elevated temperatures were identified, but it is noteworthy that these problems have not prevented effective experimentation using µ-LAM in other studies.

Overall, the proposed concept for the multi-turret hot machining tool seems to be feasible and capable of delivering improved cutting performance of difficult-to-machine materials, including the much sought after polytypes of silicon carbide. Several aspects of the investigation that is carried out are novel, these are discussed in this section, and are shown graphically in figure 5-1.

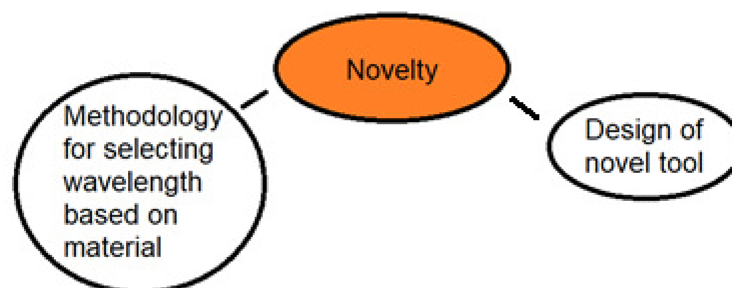

Figure 5-1 Novel Aspects of Study

The main contribution of the work is the validation that the multi-turret µ-LAM tool seems to be practical to implement; the second contribution is the proposal of a novel methodology for the selection of laser wavelength in µ-LAM. An aspect of the current investigation which is novel is developing µ-LAM so that it can be used on a fly-cutting tool. µ-LAM has been used on SPDT diamonds which are stationary, allowing for the optical setup to be simplified because there is no motion involved. A challenge faced is being able to deliver high enough laser power to the diamonds with the optical components available, while allowing the motion required. Investigating the feasibility of this technique has the effect of identifying designs which can be used, and determining whether components currently available are capable of meeting this challenge.

µ-LAM has previously been used with laser light of 1µm wavelength, but there has not been a detailed investigation determining the optimum wavelength of laser light to be used. In the current study, an in-depth investigation of the heating effects of different wavelengths of laser light is carried out to justify the selection of laser wavelength. Components are selected using the conventional 1 µm wavelength laser light, but an alternative wavelength is also selected using an evidence based approach which is expected to deliver superior performance. Components are also selected for this wavelength of laser, thereby enabling the tool to use this novel optical design. Addressing this issue contributes towards the problem in µ-LAM of selecting the power of laser that should be used. While the relationship that should be kept between power and cutting speed has been discussed previously (Ravindra, 2011), this issue has still not been resolved. As cutting speed often varies during cutting operations, the cutting enhancement provided by µ-LAM may not currently be used effectively across the whole cutting operation. The concept presented for selection of the laser wavelength is novel, and may also enable an increase in the benefits which can be gained through µ-LAM such as depths of cut achievable and resistance to tool wear.

It is encouraging that the concept central to this work seems to be feasible to implement, and the future work most desirable based upon this study is the implementation of the concept to verify its effectiveness. The alternative approach found for selecting laser wavelengths seems also to offer significant advances in µ-LAM, and further analytical investigation of this concept, as well as its implementation is desirable to evaluate the effectiveness of this concept.

REFERENCES

Agilent Technologies, 2016. The Fundamentals of Modal Testing.

Anderson, M., Patwa, R., Shin, Y.C., 2006. Laser-assisted machining of Inconel 718 with an economic analysis. Int. J. Mach. Tools Manuf. 46, 1879–1891. https://doi.org/10.1016/j.ijmachtools.2005.11.005

Arai, S., 2004. Surface integrity control of piezoelectric materials in ultra precision grinding on the basis of machine design assessment. Cranfield University.

Arif, M., Xinquan, Z., Rahman, M., Kumar, S., 2013. A predictive model of the critical undeformed chip thickness for ductile–brittle transition in nano-machining of brittle materials. Int. J. Mach. Tools Manuf. 64, 114–122.

Bifano, T.G., Dow, T.A., Scattergood, R.O., 1991. Ductile-Regime Grinding: A New Technology for Machining Brittle Materials. J. Eng. Ind. 113, 184. https://doi.org/10.1115/1.2899676

Blake, P.N., Scattergood, R.O., 1990. Ductile-Regime Machining of Germanium and Silicon. J. Am. Ceram. Soc. 73, 949–957. https://doi.org/10.1111/j.1151-2916.1990.tb05142.x

Brehl, D., Dow, T., 2008. Review of vibration-assisted machining. Precis. Eng. 32, 153–172.

Bridgman, P.W., Šimon, I., 1953. Effects of Very High Pressures on Glass. J. Appl. Phys. 24, 405–413. https://doi.org/10.1063/1.1721294

Brinksmeier, E., Grimme, D., Preuss, W., 2002. Generation of freeform surfaces by diamond machining, in: Proc. 17th Ann. Meeting ASPE.

Brinksmeier, E., Preuss, W., 2012. Micro-machining. Philos. Trans. R. Soc. Math. Phys. Eng. Sci. 370, 3973–3992. https://doi.org/10.1098/rsta.2011.0056

Chavoshi, S.Z., Goel, S., Luo, X., 2016. Influence of temperature on the anisotropic cutting behaviour of single crystal silicon: A molecular dynamics simulation investigation. J. Manuf. Process. 23, 201–210.

Chen, D., Zhang, X.F. and Ritchie, R.O., 2000. Mechanisms of High-Temperature Fatigue and Fracture in Silicon Carbide Ceramics. *Fatigue and Fracture Behavior of High Temperature Materials*, pp.1-8.

Cheng, M., 2007. Optimization of surface generation in ultra-precision multi-axis raster milling (Thesis). The Hong Kong Polytechnic University.

Chunlei, H., Zong, W., Sun, T., 2016. Origins for the size effect of surface roughness in diamond turning. Int. J. Mach. Tools Manuf. 106.

Comley, P., Morantz, P., Shore, P., Tonnellier, X., 2011. Grinding metre scale mirror segments for the E-ELT ground based telescope. CIRP Ann.-Manuf. Technol. 60, 379–382.

Dandekar, C.R., Shin, Y.C., Barnes, J., 2010. Machinability improvement of titanium alloy (Ti–6Al–4V) via LAM and hybrid machining. Int. J. Mach. Tools Manuf. 50, 174–182. https://doi.org/10.1016/j.ijmachtools.2009.10.013

Design, N.R.C.C. on T.F. for D.M. in E., 2001. Theoretical foundations for decision making in engineering design. National Academy Press.

Durazo-Cardenas, I., Shore, P., Luo, X., Jacklin, T., Impey, S., Cox, A., 2007. 3D characterisation of tool wear whilst diamond turning silicon. Wear 262, 340–349.

Goel, S., Luo, X., Comley, P., Reuben, R.L., Cox, A., 2013. Brittle–ductile transition during diamond turning of single crystal silicon carbide. Int. J. Mach. Tools Manuf. 65, 15–21. https://doi.org/10.1016/j.ijmachtools.2012.09.001

Goel, S., Luo, X., Reuben, R.L., Rashid, W.B., 2011. Atomistic aspects of ductile responses of cubic silicon carbide during nanometric cutting. Nanoscale Res. Lett. 6, 589.

Green, M.A., 2008. Self-consistent optical parameters of intrinsic silicon at 300K including temperature coefficients. Sol. Energy Mater. Sol. Cells 92, 1305–1310. https://doi.org/10.1016/j.solmat.2008.06.009

Hasselman, D.P.H., 1985. Thermal stress resistance of engineering ceramics. Mater. Sci. Eng. 71, 251–264. https://doi.org/10.1016/0025-5416(85)90235-6

Jacob, J., Patten, J.A., Couey, B.B.J.A., Marsh, E.R., 2005. Determination of the ductile to brittle transition and critical depth of cut in 6H-silicon carbide through fly cutting, in: Proceedings of the ASPE Annual Meeting.

Janvrin, B., 1996. Nd:YAG laser-assisted turning of difficult-to-machine silicon nitride. Retrosp. Theses Diss.

Jeon, Y., Lee, C.M., 2012. Current research trend on laser assisted machining. Int. J. Precis. Eng. Manuf. 13, 311–317. https://doi.org/10.1007/s12541-012-0040-4

King, R.F., Tabor, D., 1954. The Strength Properties and Frictional Behaviour of Brittle Solids. Proc. R. Soc. Math. Phys. Eng. Sci. 223, 225–238. https://doi.org/10.1098/rspa.1954.0111

Kumar, M., Melkote, S., Lahoti, G., 2011. Laser-assisted microgrinding of ceramics. CIRP Ann.-Manuf. Technol. 60, 367–370.

Lawn, B., Wilshaw, R., 1975. Indentation fracture: principles and applications. J. Mater. Sci. 10, 1049–1081. https://doi.org/10.1007/BF00823224

Lee, C.-M., Kim, D.-H., Baek, J.-T., Kim, E.-J., 2016. Laser assisted milling device: A review. Int. J. Precis. Eng. Manuf.-Green Technol. 3, 199–208. https://doi.org/10.1007/s40684-016-0027-1

Li, S. and Li, L., 2011. Radiative transfer modeling for quantifying lunar surface minerals, particle size, and submicroscopic metallic Fe. Journal of Geophysical Research: Planets, 116(E9)

Liang, Y., Chen, W., An, C., Luo, X., Chen, G., Zhang, Q., 2014. Investigation of the tool-tip vibration and its influence upon surface generation in flycutting. Proc. Inst. Mech. Eng. Part C J. Mech. Eng. Sci. 228, 2162–2167.

McKeown, P.A., 1987. The Role of Precision Engineering in Manufacturing of the Future. CIRP Ann. - Manuf. Technol. 36, 495–501. https://doi.org/10.1016/S0007-8506(07)60751-3

Mohammadi, H., Poyraz, H.B., Ravindra, D., Patten, J., 2014. Micro-Laser Assisted Single Point Diamond Turning on unpolished single crystal silicon, in: 29th Annual Meeting of the American Society for Precision Engineering, ASPE 2014. American Society for Precision Engineering, ASPE.

Mohammadi, H., Ravindra, D., Kode, S.K., Patten, J.A., 2015. Experimental work on micro laser-assisted diamond turning of silicon (111). J. Manuf. Process. 19, 125–128. https://doi.org/10.1016/j.jmapro.2015.06.007

Morantz, P., 2017. µ4 – compact 6 axes ultra precision diamond machining centre.

Moriwaki, T., Shamoto, E., 1995. Ultrasonic elliptical vibration cutting. CIRP Ann.-Manuf. Technol. 44, 31–34.

Moriwaki, T., Shamoto, E., 1991. Ultraprecision diamond turning of stainless steel by applying ultrasonic vibration. CIRP Ann.-Manuf. Technol. 40, 559–562.

Moriwaki, T., Shamoto, E., Inoue, K., 1992. Ultraprecision ductile cutting of glass by applying ultrasonic vibration. CIRP Ann.-Manuf. Technol. 41, 141–144.

Muhammad, R., Maurotto, A., Roy, A., Silberschmidt, V.V., 2012. Hot ultrasonically assisted turning of β-Ti alloy. Procedia CIRP 1, 336–341.

Murakami, K., Eryu, O., Takita, K., Masuda, K., 1987. Explosive crystallization starting from an amorphous-silicon surface region during long pulsed-laser irradiation. Phys. Rev. Lett. 59, 2203.

Nakasuji, T., Kodera, S., Hara, S., Matsunaga, H., Ikawa, N., Shimada, S., 1990. Diamond turning of brittle materials for optical components. CIRP Ann.-Manuf. Technol. 39, 89–92.

Ngoi, B., Sreejith, P., 2000. Ductile regime finish machining-a review. Int. J. Adv. Manuf. Technol. 16, 547–550.

Niihara, K., 1979. Slip systems and plastic deformation of silicon carbide single crystals at high temperatures. J. Common Met. 65, 155–166. https://doi.org/10.1016/0022-5088(79)90161-9

Ohmori, H., Nakagawa, T., 1990. Mirror surface grinding of silicon wafers with electrolytic in-process dressing. CIRP Ann.-Manuf. Technol. 39, 329–332.

Özel, T., Pfefferkorn, F., 2007a. Pulsed laser assisted micromilling for die/mold manufacturing, in: ASME International Conference on Manufacturing Science and Engineering. pp. 337–342.

Palik, E.D., 1998a. Handbook of optical constants of solids. Academic press.

Pfefferkorn, F.E., Lei, S., Jeon, Y., Haddad, G., 2009. A metric for defining the energy efficiency of thermally assisted machining. Int. J. Mach. Tools Manuf. 49, 357–365. https://doi.org/10.1016/j.ijmachtools.2008.12.009

Ravindra, D., 2011. Ductile Mode Material Removal of Ceramics and Semiconductors. Dissertations.

Ravindra, D., Patten, J., 2008. Improving the surface roughness of a CVD coated silicon carbide disk by performing ductile regime single point diamond turning, in: Proceedings of the 2008 International Manufacturing Science and Engineering Conference.

Shamoto, E., Moriwaki, T., 1999. Ultaprecision diamond cutting of hardened steel by applying elliptical vibration cutting. CIRP Ann.-Manuf. Technol. 48, 441–444.

Shayan, A.R., Poyraz, H.B., Ravindra, D., Ghantasala, M., Patten, J.A., 2009. Force Analysis, Mechanical Energy and Laser Heating Evaluation of Scratch Tests on Silicon Carbide (4H-SiC) in Micro-Laser Assisted Machining (µ-LAM) Process, in: ASME 2009 International Manufacturing Science and Engineering Conference. American Society of Mechanical Engineers, pp. 827–832.

Shibata, T., Fujii, S., Makino, E., Ikeda, M., 1996. Ductile-regime turning mechanism of single-crystal silicon. Precis. Eng. 18, 129–137.

Shim, S., Jang, J.I. and Pharr, G.M., 2008. Extraction of flow properties of single-crystal silicon carbide by nanoindentation and finite-element simulation. *Acta Materialia*, *56*(15), pp.3824-3832.

Shore, P., 1995. Machining of optical surfaces in brittle materials using an ultra-precision machine tool. Cranfield University.

Shore, P., Cunningham, C., DeBra, D., Evans, C., Hough, J., Gilmozzi, R., Kunzmann, H., Morantz, P., Tonnellier, X., 2010. Precision engineering

for astronomy and gravity science. CIRP Ann. - Manuf. Technol. 59, 694–716. https://doi.org/10.1016/j.cirp.2010.05.003

Silicon Carbide Electronics and Sensors, n.d.

Skelton, R.C., 1968. Turning with an oscillating tool. Int. J. Mach. Tool Des. Res. 8, 239–259.

Syn, C., Taylor, J., 1989. Ductile brittle transition of cutting mode in diamond turning of single crystal silicon and glass, in: ASPE/IPES Conference, Monterey.

Thompson, C., 1987. Grain growth in polycrystalline silicon films. MRS Online Proc. Libr. Arch. 106.

Tonnellier, X., 2009. Precision grinding for rapid manufacturing of large optics.

Uriarte, L., Herrero, A., Zatarain, M., Santiso, G., de Lacalle, L.L., Lamikiz, A., Albizuri, J., 2007a. Error budget and stiffness chain assessment in a micromilling machine equipped with tools less than 0.3 mm in diameter. Precis. Eng. 31, 1–12.

Uriarte, L., Herrero, A., Zatarain, M., Santiso, G., de Lacalle, L.L., Lamikiz, A., Albizuri, J., 2007b. Error budget and stiffness chain assessment in a micromilling machine equipped with tools less than 0.3 mm in diameter. Precis. Eng. 31, 1–12.

Virkar, S.R., Patten, J.A., 2009. Numerical simulations and analysis of the thermal effects on silicon carbide during ductile mode micro-laser assisted machining, in: Proceedings of the ASME International Manufacturing Science and Engineering Conference, MSEC2009. pp. 409–416.

Virkar, S.R. and Patten, J.A., 2013. Combined Effects of Stress and Temperature During Ductile Mode Microlaser Assisted Machining Process. *Journal of Manufacturing Science and Engineering*, *135*(4), p.041003.

Whitehouse, D.J., 1994. Handbook of surface metrology. CRC Press.

Wong, K.V., Hernandez, A., 2012a. A review of additive manufacturing. ISRN Mech. Eng. 2012.

Wong, K.V., Hernandez, A., 2012b. A review of additive manufacturing. ISRN Mech. Eng. 2012.

Yan, J., Kobayashi, F., 2013. Laser recovery of machining damage under curved silicon surface. CIRP Ann.-Manuf. Technol. 62, 199–202.

Yan, J., Syoji, K., Tamaki, J., 2003. Some observations on the wear of diamond tools in ultra-precision cutting of single-crystal silicon. Wear 255, 1380–1387.

Zhang, S.J., To, S., Zhang, G.Q., 2017. Diamond tool wear in ultra-precision machining. Int. J. Adv. Manuf. Technol. 88, 613–641. https://doi.org/10.1007/s00170-016-8751-9

Zhang, S.J., To, S., Zhu, Z.W., Zhang, G.Q., 2016. A review of fly cutting applied to surface generation in ultra-precision machining. Int. J. Mach. Tools Manuf. 103, 13–27. https://doi.org/10.1016/j.ijmachtools.2016.01.001

APPENDIX

Table A-13 Fiber Coupler Specification

Parameter	Value
Manufacturer	Laser Components
Wavelength	400 – 1300 nm*
Max Power	<150W
Fiber Core Size	100-2000 µm

*Only 5% reflection at 295nm wavelength

Table A-14 Rotary Joint Specification

Parameter	Value
Manufacturer	Thorlabs
Wavelength	400 – 2200 nm*
Max Power	>200W
Fiber Core Size	200µm
Maximum Rotation	10000 rpm

*Only 90% transmission at 295nm wavelength

Table A-15 1000nm Beam Splitter

Parameter	Value
Manufacturer	AplphaNov
Wavelength	600 – 1600 nm

Number of Outputs	3
Max Input Power	100 W
Input Fiber Core Size	200 µm
Output Fiber Core Size	105 µm

Table A-16 295nm Beam Splitter

Parameter	Value
Manufacturer	Lfiber
Wavelength	190 – 2500 nm
Number of Outputs	3
Max Input Power	1 W
Input Fiber Core Size	200 µm
Output Fiber Core Size	105 µm

E
D
C
B
A

10
5.16
22.19

13.92
10
7.50
A
128°
16
3.50
32.50

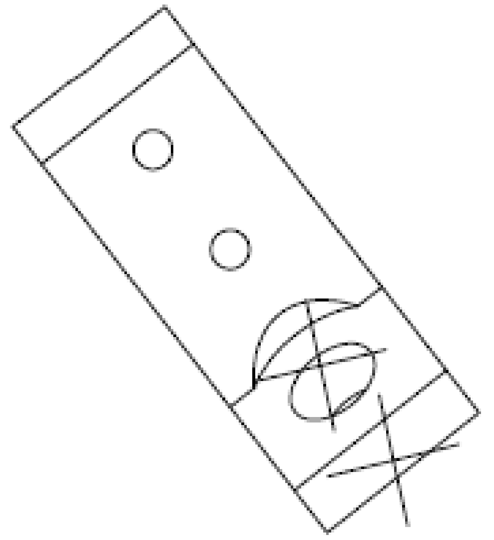

VIEW A
SCALE 3.5 : 1

UNLESS OTHERWISE SPECIFIED:
DIMENSIONS ARE IN MILLIMETERS
SURFACE FINISH:
TOLERANCES:
LINEAR:
ANGULAR:

FINISH:

DEBURR AND BREAK SHARP EDGES

	NAME	SIGNATURE	DATE
DRAWN			
CHK'D			
APPV'D			
MFG			
Q.A			

MATERIAL:

WEIGHT:

5 4 3

SOLIDWORKS Educational Product. For Instructional Use Only.

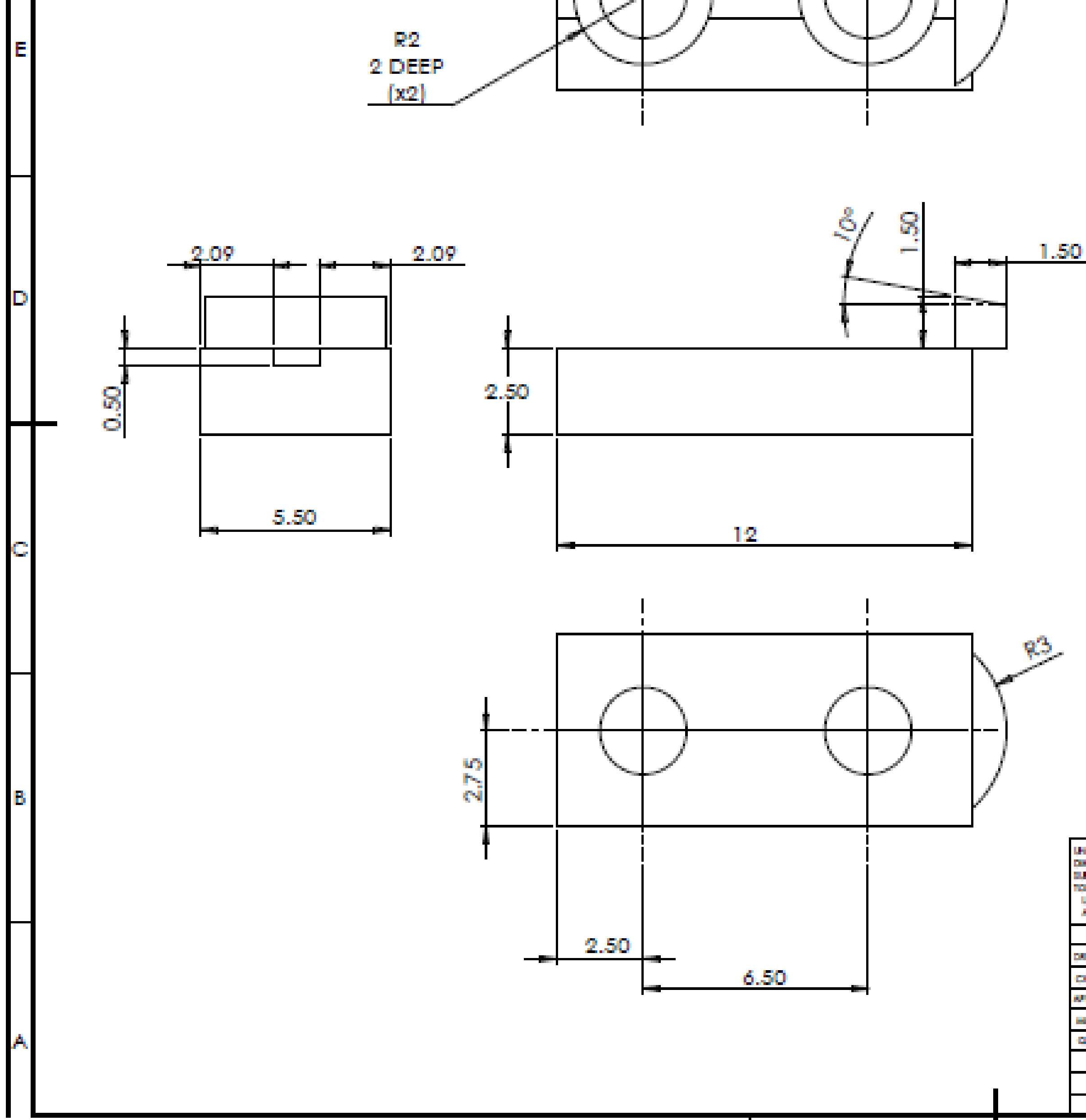

SOLIDWORKS Educational Product. For Instructional Use Only.

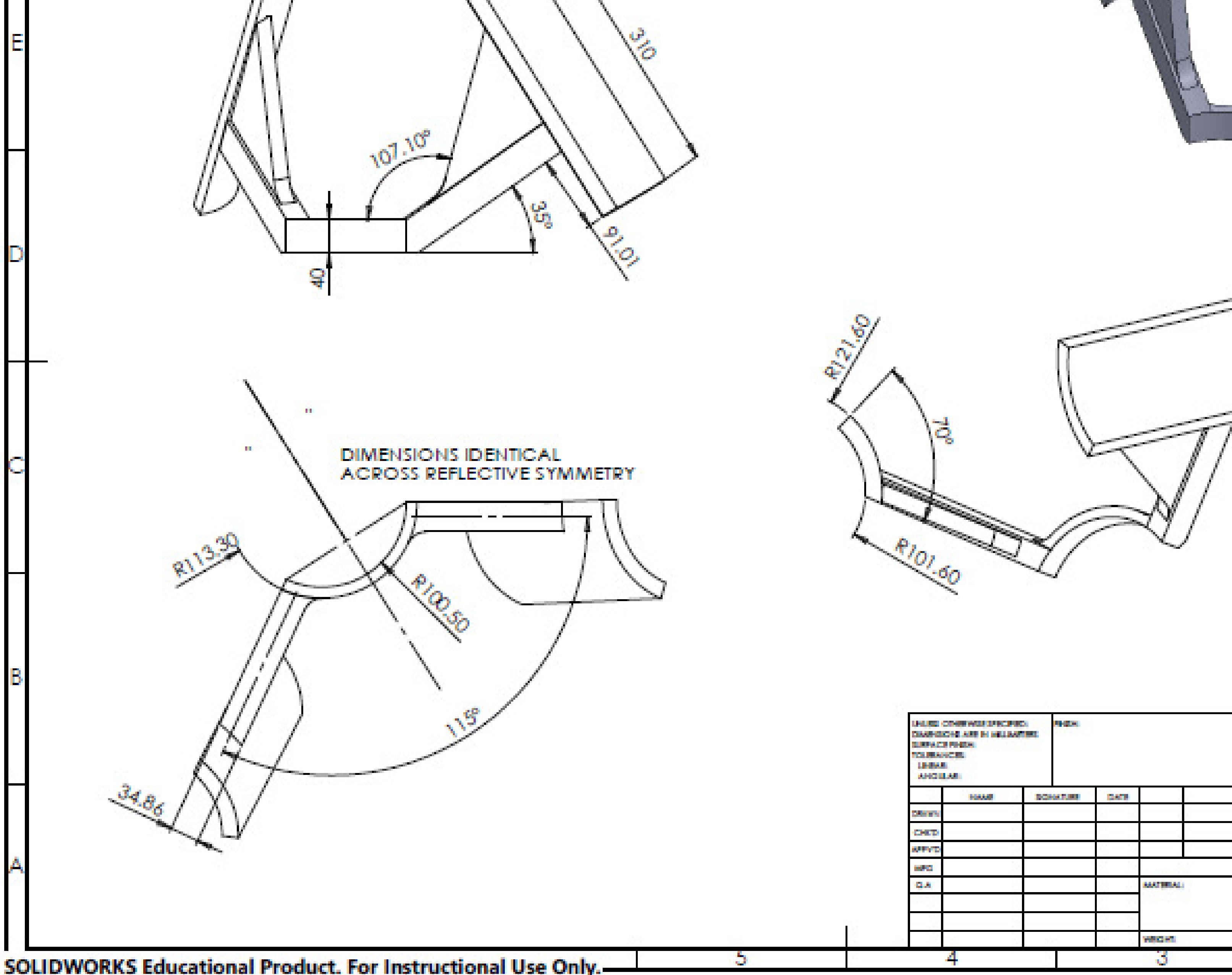
310
107.10°
35°
91.01
40
R121.60
70°
R101.60
DIMENSIONS IDENTICAL
ACROSS REFLECTIVE SYMMETRY
R113.30
R100.50
115°
34.86
E
D
C
B
A
5
4
3
SOLIDWORKS Educational Product. For Instructional Use Only.